2014

Template-mediated, Hierarchical Engineering of Ordered Mesoporous Films and Powders

Zheng Tian
Lehigh University

Template-mediated, Hierarchical Engineering of Ordered Mesoporous Films and Powders

By

Zheng Tian

Presented to the Graduate and Research Committee
of Lehigh University
in Candidacy for the Degree of
Doctor of Philosophy
in
Chemical Engineering

Lehigh University
September 2014

Certificate of Approval

Approved and recommended for acceptance as a dissertation in partial fulfillment of the requirements of the degree of Doctor of Philosophy.

_____
Date

_____
Mark A. Snyder, Ph.D.
Dissertation Advisor

_____
Accepted Date

Committee Members:

_____
Mark A. Snyder, Ph.D.
Committee Chair

_____
Hugo S. Caram, Ph.D.
Committee Member

_____
James F. Gilchrist, Ph.D.
Committee Member

_____
Kai Landskron, Ph.D.
Committee Member

Acknowledgements

I owe my special thanks to Professor Mark A. Snyder for his priceless inspiration, teaching, guidance, encouragement and support throughout my research work at Lehigh University. Without him, this thesis will never become possible. His guidance and advice not only limited to my research, but also my career and other extracurricular activities in my life here at Lehigh. Prof. Snyder's lab has been a constant source of companionship and support throughout the years in helping me to hit the ground running in my research. I would like thank my committee members, Professor Hugo S. Caram, Professor James F. Gilchrist and Professor Kai Landskron, for their insight and guidance in my research. Also, I want to send my special appreciation to Professor Andrew Klein for his advice and help.

I also want to take this opportunity to thank all my colleagues at Lehigh and friends - Qianying Guo, Shih-Chieh Kung, Daniel Gregory, Pisist Kumnorkaew (Pao), Ying Bai, Midhun Joy, and Weiqing Zheng (ChE, University of Delaware) who were being supportive and helpful throughout the course of my thesis work. I specially thank Pao and Ying for their help in film preparations by convective deposition and spin-coating techniques, Midhun Joy for teaching me the assembly and characterization of solar cells, and Weiqing for carburization treatment. I would also like to thank Dr. Zhiyang Yu for helping me use electron microscope for advanced characterization of my samples. Additionally, I highly appreciate the great help from Cong Liu in Dept. of Chemistry at Lehigh for electrochemical performance characterization especially related to the work presented in Chapter 4 of this thesis.

My research work would not have been possible without the help of many individuals in Dept. Chemical Engineering, specially Paul N. Bader and John Caffrey for helping me in electronics and instrument fabrication. I would also like to thank Barbara Kesslar, Ruth Kneller, Tracy Lopez and Janine Jekels for their supportive help whenever needed.

Finally, I am grateful to my wife Ping, parents, and parent-in-laws for their everlasting support and love throughout my life.

Table of Contents

List of Tables

List of Figures

Abstract

Hierarchical control over pore size, pore topology, and meso/mictrostructure as well as material morphology (e.g., powders, monoliths, thin films) is crucial for meeting diverse materials needs among applications spanning next generation catalysts, sensors, batteries, sorbents, etc. The overarching goal of this thesis is to establish fundamental mechanistic insight enabling new strategies for realizing such hierarchical textural control for carbon materials that is not currently achievable with sacrificial pore formation by 'one-pot' surfactant-based 'soft'-templating or multi-step inorganic 'hard-templating. While 'hard'-templating is often tacitly discounted based upon its perceived complexity, it offers potential for overcoming key 'soft'-templating challenges, including bolstering pore stability, accommodating a more versatile palette of replica precursors, realizing ordered/spanning porosity in the case of porous thin films, simplifying formation of bi-continuous pore topologies, and inducing microstructure control within porous replica materials.

In this thesis, we establish strategies for hard-templating of hierarchically porous and structured carbon powders and tunable thin films by both multi-step hard-templating and a new 'one-pot' template-replica precursor co-assembly process. We first develop a nominal hard-templating technique to successfully prepare three-dimensionally ordered mesoporous (3DOm) and 3DOm-supported microporous carbon thin films by exploiting our ability to synthesize and assemble size-tunable silica nanoparticles into scalable, colloidal crystalline thin film templates of tunable mono- to multi-layer thickness. This robust thin film template accommodates liquid and/or vapor-phase infiltration, polymerization, and pyrolysis of various carbon sources without pore contraction and/or collapse upon template sacrifice. The result is robust, flexible 3DOm or 3DOm-supported ultra-thin microporous films that can be transferred by stamp techniques to various substrates for low-cost counter-electrodes in dye-sensitized solar cells, as we demonstrate, or as potential high-flux membranes for molecular separations.

Inspired by ‘one-pot’ ‘soft’-templating approaches, wherein the pore forming agent and replica precursor are co-assembled, we establish how ‘hard’-templating can be carried out in an analogous fashion. Namely, we show how pre-formed silica nanoparticles can be co-assembled from aqueous solutions with a carbon source (glucose), leading to elucidation of a pseudo-phase behavior in which we identify an operating window for synthesis of hierarchically bi-continuous carbon films. Systematic study of the association of carbon precursors with the silica particles in combination with transient coating experiments reveals mechanistic insight into how silica-adsorbed carbon precursor modulates particle assembly and ultimately controls template particle *d*-spacing. We uncover a critical *d*-spacing defining the boundary between ordered and disordered mesoporosity within the resulting films.

We ultimately extend this thin-film mechanistic insight to realize ‘one’-pot, bi-continuous 3DOm carbon powders. Through a combination of X-ray photoelectron spectroscopy (XPS), Raman spectroscopy, and high-resolution transmission electron microscopy (HR-TEM), we elucidate novel synthesis-structure relations for template-mediated microstructuring of the 3DOm replica carbons. Attractive properties of the resulting bi-continuous porous carbons for applications, for example, as novel electrodes, include high surface areas, large mesopore volumes, and tunable graphitic content (i.e. >50%) and character. We specifically demonstrate their performance, in thin film form, as counter-electrodes in dye-sensitized solar cells. We also demonstrate how they can be exploited in powder form as high-performance supercapacitor electrodes exhibiting attractive retention and absolute capacitance.

We conclude the thesis by demonstrating the versatility of both the thin-film and powder templating processes developed herein, for realizing ordered binary colloidal crystal templates and their bi-modal porous carbon replica films, expanding compositional diversity of the ‘one-pot’ thin film process beyond carbons to include an example of 3DOm ZrO_2 films, and employing the hard-templating process as a strategy for realizing 3DOm carbon-supported nanocarbides.

Chapter 1: Introduction

1.1 Background and Motivation

Design and synthesis of porous architectures spanning sub-micrometer to nanometer scales has long been an important science subject,[1] motivated to some extent by the ubiquitous examples of 'active' or 'functional' porosity existing in nature (e.g., paths for water dispersion in trees, pulmonary and circulation systems, cell membranes, diatom exoskeletons). Such structures provide both passive and active platforms for high-resolution manipulation of molecular species, charge, fluids, etc. *As such, the ability to rationally and synthetically tune pore size, topology, and function in addition to material morphology (e.g., powders, monoliths, thin films) is a critical step in synthetic materials development for realizing next generation catalysts, sensors, batteries, sorbents, etc. with implications in Grand Challenges spanning energy, the environment and health.*

According to the International Union of Pure and Applied Chemistry (IUPAC), pore structures can be classified based on their pore diameter, D, as microporous (D < 2 nm), mesoporous (2 < D < 50 nm), or macroporous (D > 50 nm). Microporous materials, in the form, for example, of zeolites (e.g., ZSM-5) or activated carbons, have been widely studied and used in industrial chemical and petrochemical processes as shape-selective catalysts and/or high-capacity sorbents,[2, 3] among other applications, there taking advantage of the ultra-high surface area and pores of molecular dimensions. At the opposite end of the pore-size spectrum, macroporous materials including foams, gels, and correspondingly sized, but ordered, porous structures have been studied and applied[4] as photonic crystals[5] to tissue scaffolds.

With progress made in modern nanoscience, mesoporous materials have garnered significant recent interest within the fields of engineering, materials science, chemistry, physics and biology owing, in part, to the simple fact that they link micropore and macropore length scales of interest.

They, therefore, represent a critical scale in the development of hierarchically structured materials[6, 7], a class of materials that is garnering growing interest both academically and industrially due to their potential for realizing multi-scale control and manipulation of matter. In addition, the 2-50 nm length scale endows mesoporous materials with an attractive balance between moderately high surface areas and accessible pore volumes, the former important for tuning active surface function and the latter critical for facilitating rapid molecular transport, two key properties in applications spanning adsorption[8, 9], separation[10], catalysis[11, 12], sensing[13] and energy storage and conversion,[14, 15, 16] among others.

The ability to realize truly hierarchical control over pore size for a compositionally diverse class of materials and for a range of material morphologies including porous powders and thin films has been a challenge intrinsic to porous materials work. As depicted in Figure 1.1, hierarchical pore size control spanning sub-nanometers to tens of nanometers is crucial for addressing applications ranging, respectively, from selective small molecule separations, sensing, and reaction (e.g., tunable surface function or catalytic moieties, size/shape-selectivity microporosity) through meso- and even macro-scale elimination of transport resistances (e.g., bulky molecules, electrolyte infiltration).

Figure 1.1: Range of pore sizes required for versatile application

Ultimately, realization of versatile strategies to introduce and tune material properties at all scales—molecular to macroscopic—would help endow materials with multiple functionalities suitable for addressing complex and multifaceted applications. For example, monoliths/bulk powders that combine micropore-derived large surface areas and size-/shape-selectivity with 3D-interconnected mesopores have clearly demonstrated advantages, for example, in efficient

catalysis. When adopting such materials in other applications, for example as thin film electrodes for energy storage devices, hierarchical structures, with high surface area, better permeability and reduce path length[16], that enable efficient contacting of electrolytes can enable delivery of greater amounts of energy than can be achieved with a single porosity scale. In both applications the additional realization of a high degree of 3D ordering of the pore topology can help facilitate molecular transport, help circumvent transient pore blockages, and enhance energy storage over disordered counterpart materials.

This motivates the **goal of this dissertation**, to establish strategies for realizing a new level of hierarchical control, not achievable with the current paradigm for pore formation, over three-dimensionally ordered mesoporous (3DOm) and 3DOm/microporous carbon powders and thin films suitable for applications as efficient electrode materials and supercapacitors, that should be extendable to other compositional classes of materials and functions (e.g., stable catalysts).

1.2 Mesoporous materials: Past, present, and future

The first widely-cited work on mesoporous materials dates back to the 1980s, when pillared clays containing mesopores were first studied in detail. However, in such materials the disordered rectangular pores could not be fully opened, making access of the inter-layer galleries by reactant molecules difficult if not impossible, and thereby leading to unwanted coke formation during catalytic application of those materials.[3] Additionally, control over the pore size distribution in such materials could be achieved only over a limited range, and the pores assumed a disordered topology.

A marked upsurge in the active study of ordered mesoporous materials began in 1992 with the development by the Mobil Oil Company of the class of periodic mesoporous silica materials known as the M41S phase.[17, 18] These materials were obtained by surfactant assisted synthesis, so-called liquid crystal templating, under conditions employed to crystallize microporous solids like zeolites.[19] The process was comparable to lesser-cited work by Ciola and co-workers patented

two decades earlier for synthesizing ultra-low-density structures[20]. The M41S materials provided an attractive combination of pore order, akin to zeolites, with pore sizes exceeding the molecular dimensions of zeolitic pores (i.e., 15 angstroms)[21]. In 1993, Kuroda reported the optimization of synthesis conditions to achieve an ordered mesoporous silicate[22]. Since then there have been broad worldwide research efforts, leading to the independent area of research on ordered mesoporous materials broadly spanning the development of novel synthesis strategies, methods for characterizing the resulting structures, and specific applications. This is illustrated by the rise in the number of Mesoporous'-related publications since 1990 in the *ISI Web of Science* as shown in Figure 1.2. Before 1992, there were less than 50 publications per year, while the year 1992 marked the increase in the number of publications.

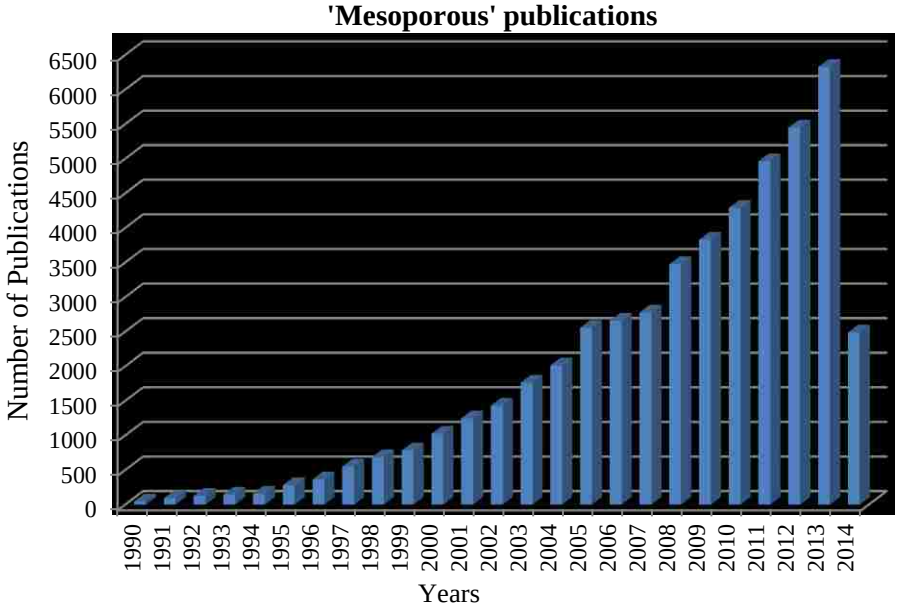

Figure 1.2: Statistics of publications after 1990 with key word "mesoporous" based upon ISI Web of Science search (as of June 2014).

1.2.1 Current paradigm for bulk mesopore templating

The construction of mesoporous materials with highly ordered porosity has generated much interest in the porous materials area. Generally, two kinds of sacrificial templates are adopted to produce such ordered mesoporous materials: 1) supermolecular aggregates such as surfactant

micelle arrays, or 2) rigid preformed porous solids such as ordered mesoporous silica, carbon and colloidal crystals. The corresponding synthesis pathways are usually described in the literature as *soft*- and *hard*-templating techniques, respectively.

1.2.1.1 Soft-templating of ordered mesoporous materials

Soft-templating is often cited as a useful and convenient pathway for the preparation of ordered mesopores materials[23]. Ordered mesostructured templates are typically achieved by the cooperative assembly of surfactant molecules and guest species driven by the reduction in interfacial energy[24]. The surfactants, building blocks of the soft-templating strategy, are amphiphilic molecules that contain both hydrophilic and hydrophobic domains. Three major classes of surfactant molecules can be adopted for the soft-templating strategy: cationic, anionic and non-ionic. Ionic surfactants typically produce either micropores or small mesopores (2~4nm); however non-ionic surfactants generate mesopores that range in diameter from a few nm to more than 10nm,[25] and are widely used for assembly of ordered mesoporous materials. The structure of non-ionic surfactants varies widely from Brij compounds, containing a linear alkyl chain connected to a hydrophilic polyethylene oxide (-CH_2-CH_2-O-, PEO) chain, to a variety of block copolymeric surfactants[26]. Tri-block polyethylene oxide (PEO)—polypropylene oxide (PPO)—PEO (PEO_x-PPO_y-PEO_x) surfactants, famously known as Pluronics®, are also used. Brij surfactants produce small mesopores, while higher molecular weight Pluronics® can template mesopores around 4~20nm in diameter[27]. Self-assembly processes of these non-ionic surfactants are primarily mediated by van der Waals interactions and hydrogen bonding[28].

Two representative examples of soft-templating techniques include ordered mesoporous silica (OMS) and carbon (OMC) materials. For example, continuous mesostructured silica films and powders have been successfully achieved by so-called evaporation-induced self-assembly (EISA),[29, 30] a process involving: i) preparation of a homogeneous solution containing the templating surfactants and guest precursors (e.g. tetraethyl orthosilicate, TEOS), ii) casting of the

solution, iii) self-assembly of the templating surfactant into lyotropic phases in the presence of the inorganic oligomeric precursors as triggered by the progressive evaporation of the volatile solvent[31], iv) treatment to stabilize the resulting organic-inorganic template-precursor composite mesostructure, and v) template elimination to open the ordered mesoporous materials[32].

Similarly as illustrated in Figure 1.3, to prepare ordered mesoporous carbon by soft-templating, in the initial homogeneous solution[32] resol oligomers, having a 3D network structure and plenty of hydroxyl groups, can interact with PEO blocks of triblock-*co*-polymer templates via hydrogen bonds. Evaporation of ethanol enriches the concentration of copolymers and drives the organization of resol-copolymer composites into an ordered liquid-crystalline mesophase[33]. The assembly of resols and copolymer templates occurs readily to form ordered mesostructures without macrophase separation. In 2004, Dai's group[34] first synthesized well-ordered mesostructured carbons as films by using resorcinol selectively partitioned in polystyrene-b-poly(4-vinylpyridine) (PS-P4VP) and subsequently cross-linked by formaldehyde vapor. By adjusting surfactant/resol ratio or choosing different block copolymers, porous carbon with various mesostructures can be obtained[35], as well as control over mesopore sizes realized[36, 37].

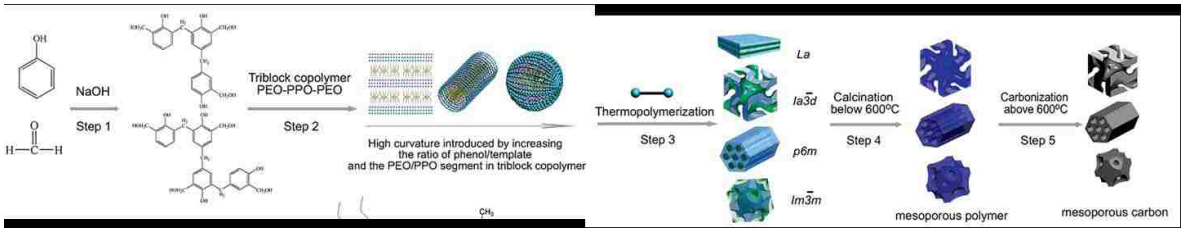

Figure 1.3: Illustration of the preparation of ordered mesoporous carbon frameworks by the soft-templating technique. Reprinted from Meng et al., 2006[35].

This soft-templating technique has more recently been extended to the synthesis of mesoporous metals[38] and metal oxides[39]. For example, amphiphilic block-*co*-polymers as template and metal halides as inorganic precursors were used to realize several mesoporous metal oxides, including TiO_2, ZrO_2, Al_2O_3, WO_3 [30] and some other mixed oxides[31, 40]. The most

important point for successful soft-templating of mesoporous metal oxides is control over the rate of alcoholysis of inorganic salts[31].

The organic liquid-crystalline templates and final ordered mesostructures of soft-templated materials are influenced by numerous factors, such as molecular structure of the surfactant and its concentration, chemical nature of the inorganic precursors, treatment conditions, and even some ancillary conditions such as water concentration, humidity and temperature[31]. While this multi-parameter sensitivity provides numerous handles for tuning the soft-templating of mesoporous powders and thin films, it also convolutes the phase space. In addition, despite significant progress, there are some critical issues that continue to challenge soft-templating of porous inorganic materials. For example, deleterious shrinkage or even collapse of mesopores has been shown to occur during thermal treatment aimed at structural evolution and/or template removal[35, 41]. Specifically, during high-temperature removal of organic template molecules and carbonization stages, significant shrinkage of mesopores[42, 43] from 18%~60% occurs as well as partial collapse of the structure[44]. Furthermore, soft-templating tends to lead to wormy pore topologies, owing to the flexibility of the liquid crystalline templates, and giving rise to tortuous and sometimes uni-dimensional pores[35, 45].

Additionally, in this sol-gel process employed for soft-templated synthesis of mesoporous metal oxides, restrained hydrolysis and condensation of the inorganic precursor species appears to be crucial for forming mesophases of most non-siliceous oxides because of their strong tendency to precipitate and crystallize into bulk (untemplated) oxide phases. As such, strategies must be adopted to control the rate of reactions, including the pH optimization, water content in the precursor, and the humidity[46]. Similar to collapse of carbonaceous materials upon high-temperature treatment, high-temperature processing of many metal oxides can also cause crystallites to sinter, grow and ultimately destroy pores given the limited resistance and temperature-susceptibility of the organic templates.[41]

1.2.1.2 Hard-templating of ordered mesoporous materials

As another synthetic pathway to fabricate ordered mesoporous materials of various composition and pore topologies, the so-called hard-templating method, also known as the nanocasting technique, has been developed over the past decades.[47] Ryoo first reported the preparation of ordered mesoporous carbons (OMCs) by adopting a the soft-templated ordered mesoporous aluminosilicate MCM-48 as a hard template. In that work, a carbon precursor was infiltrated into the pores of the MCM-48 template wherein it was polymerized and carbonized prior to the selective removal (i.e., by etching) of the template[48]. 3D ordered mesosized platinum networks as well as crystallized, high-surface area metal oxides (e.g., Cr_2O_3, Mn_2O_3, Fe_2O_3 and CeO_2)[49] have also been achieved by a similar templating approach.[50]

The typical process employed for such hard-templating or nanocasting techniques is illustrated in Figure 1.4, and involves: i) the synthesis of a sacrificial mesoporous template, ii) fluid precursor (typically liquid or gas phase) infiltration into the mesochannels or mesoporosities of the template structure, iii) conversion of the molecular precursor into the replica product under the confinement imposed by the mesochannels, and iv) removal of the mesoporous template.

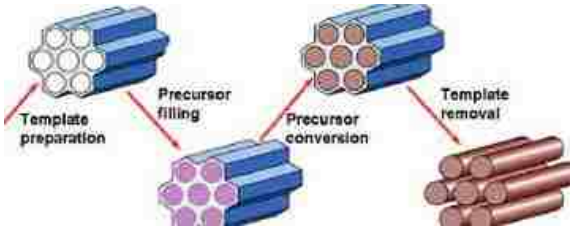

Figure 1.4: Illustration of the general approach for realizing ordered mesoporous frameworks by the hard-templating technique. Reprinted Wan et al., 2008[33].

The specific pre-formed template can assume numerous forms, commonly spanning ordered mesoporous silicas (OMSs), ordered mesoporous carbons (OMCs), and colloidal crystalline powders, with the cost and complexity of the mult-step nanotemplating process schematized in Figure 1.4 contingent, in part, upon the corresponding complexity of the synthesis of the template itself. In addition, the length scales of the replica structure are dependent upon those of the

template. Namely, assuming perfect replication, the size of the pores and the resolution with which they can be tuned within the replica materials are governed by the corresponding resolution and range over which the walls of the template material can be modulated. Likewise, the thickness of the walls of the replica structure is governed by the tunability of the pore size of the template material. Some challenges with the hard-templating approach, resulting from the need to "back-fill" a pre-formed template relate to overcoming sometimes complex interactions between the pore walls and precursors, including hydrogen bonding and van der Waals forces[51], and random blockage of template channels, leading to a poor or incomplete infiltration.[31]

1.2.2 Versatile pore engineering: Seamlessly linking powder and thin film processing

Among porous materials, porous inorganic films have attracted attention for commercial applications spanning industrial chemicals (e.g., gas, isomer separations, catalysis, adsorption), electronic and energy generation/storage (e.g., capacitor electrodes, electrolyte membranes in fuel cell and lithium-ion battery[52, 53]), health and foods (e.g., blood dialysis, drug delivery devices), and the environment (e.g., desalination, adsorption) [54] owing, in part, to their thermal, chemical, and mechanical stability. In the context especially of inorganic films (e.g., carbon molecular sieving, metal oxide, zeolitic films), however, versatile strategies for precisely controlling thickness as well as film-spanning porosity and the concomitant pore size—be it microporous, mesoporous, or hierarchical—to meet the often multifaceted needs of the wide range of aforementioned applications, has been a persistent challenge.

The large thickness (i.e., order of microns to tens of microns) and limited control over morphology and pore topology within conventional inorganic films can lead, for example, to stress-induced crack formation, pore blockage in the case of 1D pores,[55] and sluggish transport as underscored by the inverse proportionality of flux to the actual or effective (i.e., accounting for pore tortuosity) film thickness captured most simply by Fick's first law of diffusion, $\mathrm{J} = -\mathrm{D}\frac{\partial \varphi}{\partial \mathrm{x}}$,

where J is the diffusion flux, D is the diffusion coefficient, φ is the local concentration of solute, and x is the dimension in the direction of flux. *As such, there is a general demand for development of porous thin film technologies in which fine control over materials properties (e.g., pore size, connectivity, film thickness, robustness and composition) can be achieved to meet requirements of specific applications for e.g., molecular and charge transport, catalytic activity, adsorption selectivity, etc.*

1.3 Approach and Outline

In this thesis, we focus on the development of pore-forming strategies capable of translating conventional templating of bulk porous powders to methods suitable for realizing scalable porous inorganic thin films bearing three-dimensionally ordered mesoporosity (3DOm) as well as hierarchical 3DOm-supported microporous morphologies (Chapters 2 and 3). New mechanistic insight into simplified, yet versatile hard-templating of porous materials, obtained from carefully designed thin film studies, is then translated back to synthetic porous powders, wherein template-mediated microstructure control is elucidated (Chapter 4).

In the context of thin, porous inorganic films, both hard- and soft-templating methods have tacit advantages and disadvantages highlighted across the body of porous thin film work in the open literature, which we summarize in Table 1.1. From the standpoint of soft-templating of thin films, a primary benefit is the 'one-pot' nature of the synthesis, namely the co-assembly of the pore-forming agent (e.g., lyotropic liquid crystal) and replica material, which effectively reduces the concomitant processing. However, drawbacks of this process, paralleling the same for soft-templating of bulk porous materials described above, include limits on carbon precursor due to the reliance on hydrogen-bond-induced organization of organic-organic mesostructures with the resol hydroxyl functionality,[56, 57, 58, 59] complex thermodynamics of assembly, and inaccessibility of the upper mesopore size range (i.e., 25-50 nm)[60, 61]. Challenges with pore shrinkage are especially acute in soft-templated thin films, with uniaxial shrinkage directed normal to the

film/substrate deriving from anisotropies induced by the film. This uniaxial pore shrinkage is responsible for the transition from a body-centered cubic mesostructure to an orthorhombic mesostructure.[41] This phenomena is compounded by the association of the pore forming phase (e.g., micelles) with the substrate upon which the film is cast, leading to pore orientation parallel rather than perpendicular to the substrate without additional treatment like solvent annealing, imposition of external fields, or interface control.[62, 63, 64, 65] This pore orientation can preclude facile access to the pore space[31].

Table 1.1: Comparison between soft- and hard-templating methods of ordered porous carbons

	Soft Templating	**Hard Templating**
Procedure[66]	"One-pot" synthesis	Multi-step
Post-treatment	Sophisticated procedure to fix defects[34]	None
Template source	Limited to amphiphilic surfactant and block-co-polymer, some are not commercially available	Monosized silica particles, mesoporous silica, zeolites, MOF, ...[67]
Carbon source	Limited to resol monomers[66]	*Various*: FA, resol, sucrose, biomass,...
Reaction conditions	Highly sensitive to pH, temperature, reactant ratio, ...[68]	Template/assembly decoupled
Pore size distribution	Determined by surfactant and reactants ratio	Controlled by template wall thickness[69]
Pore size range	1.5nm~25nm[33]	From ~nm to even ~μm
Pore structure topology	Uneasy to manipulate, a combination of vertical, horizontal and wormy[45]	Determined by templates, such as 3D interconnected or 1D channel
Pore structure stability	At least 10% size shrinkage and partial collapse during thermal removal of template molecules[44]	Template-bolstered mechanical stability
Film/membrane size[34]	Scalable	Perceived challenges in scale-up
Cost	Expensive template and source molecules	Dependent on the pre-synthesized template molecules

1.3.1 Approach

The alternative hard templating process offers potential for overcoming some of the soft-template-specific drawbacks if key challenges with hard templating can be overcome. Here, we aim to accomplish this by exploiting convective assembly to realize tunable colloidal crystal thin films as a versatile and scalable strategy for sacrificial templating of thickness- and morphology (i.e., 3DOm, 3DOm-supported microporous)-tunable porous carbon films based upon a wide range of carbon sources. As illustrated in Figure 1.5, our nominal approach is to i) assemble template films of robust, monosized nanometer-scale silica particles, ii) introduce carbon precursors into the void spaces within the template film, iii) carry out processing steps to solidify the introduced precursors, and iv) selectively sacrifice the template.[6] This nominal process, therefore, is akin to the conventional hard-templating strategy schematized in Figure 1.4, but here we leverage our ability to convectively assemble large-area colloidal crystalline films from nanoparticle sols as self-templated and continuous films with large pore volume for accommodating carbonaceous precursor.

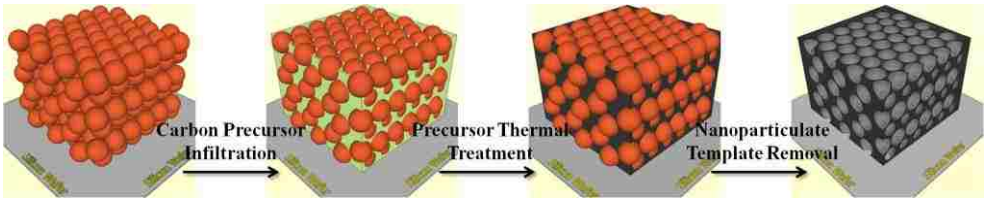

Figure 1.5: Illustration scheme for preparation of ordered mesoporous carbon films by hard-templating technique.

1.3.2 Outline

Chapter 2

In Chapter 2, we develop a nominal hard-templating technique to successfully prepare 3DOm and 3DOm-supported microporous carbon thin films by exploiting our ability to synthesize and assemble size-tunable silica nanoparticles into scalable, colloidal crystalline thin films of tunable

mono- to multi-layer thickness. We establish a precursor infiltration approaches for successfully introducing a wide range of carbon precursors (e.g., furfural/oxalic acid, phenol-formaldehyde, resorcinol-formaldehyde, sucrose) into the interstitial pore space of the silica colloidal crystal films, with control over infiltration conditions enabling tunable formation of i) ultra-thin microporous carbon layers self-supported on 3DOm films or ii) open 3DOm films. The stability of the silica templates under polymerization and carbonization conditions helps bolster mesopore robustness, eliminating uniaxial pore shrinkage. The inherent flexibility of these ultra-thin films enables polymer-assisted transfer of the films among substrates. In addition, direct formation of films upon even rough surfaces is demonstrated, allowing exploitation of the large-pore volume and high surface areas of the 3DOm films as potential low-cost alternatives to costly Pt-based electrodes in dye-sensitized solar cell technologies.

Chapter 3

Following the demonstration in Chapter 1 of how convectively deposited colloidal crystal thin films can serve as a versatile and scalable template for replica porous carbon films, we focus our attention in this chapter in addressing the remaining significant drawback cited frequently for hard-templating strategies; namely, the multi-step nature of this approach. Specifically, motivated by 'one-pot' soft-templating approaches wherein the pore forming agent and replica precursor are co-assembled, we study how hard-templating can be carried out in an analogous fashion. Namely, we explore the co-assembly of molecular carbon precursors (e.g., glucose) with the silica nanoparticles from aqueous solutions. The result is the elucidation of a pseudo-phase behavior identifying an operating window defined by incipient silica volume fraction and concentration of the carbon precursor wherein hierarchically bi-continuous carbon films are synthesized. Systematic study of the association of carbon precursor with the silica particles in combination with transient coating experiments reveals mechanistic insight into how silica-

adsorbed carbon precursor modulates particle assembly and ultimately controls particle *d*-spacing. We uncover a critical *d*-spacing defining the boundary between ordered and disordered films.

Chapter 4

In this chapter, we extend the mechanistic insight into one-pot hard-templating of carbon thin films obtained in Chapter 3 to the formation of one-pot hard-templated bi-continuous powders. Namely, we show that similar d-spacing-derived order-disorder transitions exist for the correspondingly assembled powders, with the parametric envelope expanded to include lower carbon precursor concentrations than in the thin film case for successfully obtaining 3DOm carbon powders. In addition, we move beyond mesostructuring of the carbon and employ a combination of X-ray photoelectron spectroscopy (XPS), Raman spectroscopy, and high-resolution transmission electron microscopy (HR-TEM) to understand novel synthesis-structure relations wherein template-mediated microstructuring of the 3DOm replica carbons occurs. Specifically, we uncover how carbon precursor concentration can tune the fraction of sp^2-hybridized carbon allotropes within the final 3DOm carbon precursor, accompanied by remarkable pore volumes and attractive surface areas. We demonstrate, using cyclic voltammetry, how these properties can be exploited, albeit without being able to specifically decouple their effects, for high-performance supercapacitance rivaling other nanotemplated porous carbons and even porous graphene.

Chapter 5

Chapter 5 returns to carbon film replication concepts introduced in Chapter 2, but focuses on expanding the structural diversity of the template as well as carbon replica films. Specifically, proof-of-concept of convective deposition of binary nanoparticle films is demonstrated, with realization of NaCl-isostructural films wherein the smallest nanoparticles occupy the octahedral positions between cubically arranged larger silica particles. The role of solvent evaporation and

possible matching of flux of the large and small particles to the drying front is discussed as a possible mechanism for successful co-assembly of novel binary nanoparticle films. Carbon replication of these films is demonstrated to result in bimodal porous carbon films.

Chapter 6

We conclude the thesis with a summary of new insight established herein for realizing carbon thin films and powders by novel hard-templating strategies. We also discuss concepts and even proof-of-concept data for future work. This includes further extension of strategies established in this thesis for realizing novel catalytic materials, namely 3DOm-carbon supported MoC structures. In addition, we show preliminary evidence that the 'one-pot' co-deposition strategies highlighted in Chapter 4 can be extended to systems other than carbon. Specifically, we demonstrate how 3DOm zirconia films can also be realized as an example indicating the possible diversity of the materials palette that may be accessible with the approaches developed in this thesis for hard-templating of porous materials.

1.4 Reference

1. Wu, D. C.; Xu, F.; Sun, B.; Fu, R. W.; He, H. K.; Matyjaszewski, K. Design and Preparation of Porous Polymers. *Chemical Reviews* **2012,** *112* (7), 3959-4015.

2. Davis, M. E. Ordered porous materials for emerging applications. *Nature* **2002,** *417* (6891), 813-821.

3. Corma, A. From microporous to mesoporous molecular sieve materials and their use in catalysis. *Chemical Reviews* **1997,** *97* (6), 2373-2419.

4. Braun, P. V. Materials Chemistry in 3D Templates for Functional Photonics. *Chemistry of Materials* **2014,** *26* (1), 277-286.

5. Subramanian, G.; Manoharan, V. N.; Thorne, J. D.; Pine, D. J. Ordered macroporous materials by colloidal assembly: A possible route to photonic bandgap materials. *Advanced Materials* **1999,** *11* (15), 1261-+.

6. Petkovich, N. D.; Stein, A. Controlling macro- and mesostructures with hierarchical porosity through combined hard and soft templating. *Chemical Society Reviews* **2013,** *42* (9), 3721-3739.

7. Parlett, C. M. A.; Wilson, K.; Lee, A. F. Hierarchical porous materials: catalytic applications. *Chemical Society Reviews* **2013,** *42* (9), 3876-3893.

8. Wu, Z. X.; Zhao, D. Y. Ordered mesoporous materials as adsorbents. *Chemical Communications* **2011,** *47* (12), 3332-3338.

9. Hartmann, M. Ordered mesoporous materials for bioadsorption and biocatalysis. *Chemistry of Materials* **2005,** *17* (18), 4577-4593.

10. Karger, J.; Valiullin, R. Mass transfer in mesoporous materials: the benefit of microscopic diffusion measurement. *Chemical Society Reviews* **2013,** *42* (9), 4172-4197.

11. Taguchi, A.; Schuth, F. Ordered mesoporous materials in catalysis. *Microporous and Mesoporous Materials* **2005,** *77* (1), 1-45.

12. Ivanova, II; Knyazeva, E. E. Micro-mesoporous materials obtained by zeolite recrystallization: synthesis, characterization and catalytic applications. *Chemical Society Reviews* **2013,** *42* (9), 3671-3688.

13. Wagner, T.; Haffer, S.; Weinberger, C.; Klaus, D.; Tiemann, M. Mesoporous materials as gas sensors. *Chemical Society Reviews* **2013,** *42* (9), 4036-4053.

14. Zhai, Y. P.; Dou, Y. Q.; Zhao, D. Y.; Fulvio, P. F.; Mayes, R. T.; Dai, S. Carbon Materials for Chemical Capacitive Energy Storage. *Advanced Materials* **2011,** *23* (42), 4828-4850.

15. Zhang, H. G.; Yu, X. D.; Braun, P. V. Three-dimensional bicontinuous ultrafast-charge and -discharge bulk battery electrodes. *Nature Nanotechnology* **2011,** *6* (5), 277-281.

16. Nishihara, H.; Kyotani, T. Templated Nanocarbons for Energy Storage. *Advanced Materials* **2012,** *24* (33), 4473-4498.

17. Beck, J. S.; Vartuli, J. C.; Roth, W. J.; Leonowicz, M. E.; Kresge, C. T.; Schmitt, K. D.; Chu, C. T. W.; Olson, D. H.; Sheppard, E. W.; McCullen, S. B.; Higgins, J. B.; Schlenker, J. L. A NEW FAMILY OF MESOPOROUS MOLECULAR-SIEVES PREPARED WITH LIQUID-CRYSTAL TEMPLATES. *Journal of the American Chemical Society* **1992,** *114* (27), 10834-10843.

18. Kresge, C. T.; Leonowicz, M. E.; Roth, W. J.; Vartuli, J. C.; Beck, J. S. ORDERED MESOPOROUS MOLECULAR-SIEVES SYNTHESIZED BY A LIQUID-CRYSTAL TEMPLATE MECHANISM. *Nature* **1992,** *359* (6397), 710-712.

19. Kresge, C. T.; Roth, W. J. The discovery of mesoporous molecular sieves from the twenty year perspective. *Chemical Society Reviews* **2013,** *42* (9), 3663-3670.

20. Chiola Vincent, R. J. E., Vanderpool Clarence D. Process for producing low-bulk density silica. US Patent US 3556725 A, 1971.

21. Hoffmann, F.; Cornelius, M.; Morell, J.; Froba, M. Silica-based mesoporous organic-inorganic hybrid materials. *Angew. Chem.-Int. Edit.* **2006,** *45* (20), 3216-3251.

22. Inagaki, S.; Fukushima, Y.; Kuroda, K. SYNTHESIS OF HIGHLY ORDERED MESOPOROUS MATERIALS FROM A LAYERED POLYSILICATE. *Journal of the Chemical Society-Chemical Communications* **1993,** (8), 680-682.

23. Nicole, L.; Boissiere, C.; Grosso, D.; Quach, A.; Sanchez, C. Mesostructured hybrid organic-inorganic thin films. *Journal of Materials Chemistry* **2005,** *15* (35-36), 3598-3627.

24. Shi, Y. F.; Wan, Y.; Zhao, D. Y. Ordered mesoporous non-oxide materials. *Chemical Society Reviews* **2011,** *40* (7), 3854-3878.

25. Soler-illia, G. J. D.; Sanchez, C.; Lebeau, B.; Patarin, J. Chemical strategies to design textured materials: From microporous and mesoporous oxides to nanonetworks and hierarchical structures. *Chemical Reviews* **2002,** *102* (11), 4093-4138.

26. Innocenzi, P.; Malfatti, L.; Soler-Illia, G. Hierarchical Mesoporous Films: From Self-Assembly to Porosity with Different Length Scales. *Chemistry of Materials* **2011,** *23* (10), 2501-2509.

27. Soler-Illia, G.; Azzaroni, O. Multifunctional hybrids by combining ordered mesoporous materials and macromolecular building blocks. *Chemical Society Reviews* **2011,** *40* (2), 1107-1150.

28. Fan, J.; Boettcher, S. W.; Tsung, C. K.; Shi, Q.; Schierhorn, M.; Stucky, G. D. Field-directed and confined molecular assembly of mesostructured materials: Basic principles and new opportunities. *Chemistry of Materials* **2008,** *20* (3), 909-921.

29. Zhao, D.; Yang, P.; Melosh, N.; Feng, J.; Chmelka, B. F.; Stucky, G. D. Continuous mesoporous silica films with highly ordered large pore structures. *Advanced Materials* **1998,** *10* (16), 1380-+.

30. Yang, P. D.; Deng, T.; Zhao, D. Y.; Feng, P. Y.; Pine, D.; Chmelka, B. F.; Whitesides, G. M.; Stucky, G. D. Hierarchically ordered oxides. *Science* **1998,** *282* (5397), 2244-2246.

31. Li, W.; Yue, Q.; Deng, Y. H.; Zhao, D. Y. Ordered Mesoporous Materials Based on Interfacial Assembly and Engineering. *Advanced Materials* **2013,** *25* (37), 5129-5152.

32. Meng, Y.; Gu, D.; Zhang, F. Q.; Shi, Y. F.; Yang, H. F.; Li, Z.; Yu, C. Z.; Tu, B.; Zhao, D. Y. Ordered mesoporous polymers and homologous carbon frameworks: Amphiphilic surfactant templating and direct transformation. *Angew. Chem.-Int. Edit.* **2005,** *44* (43), 7053-7059.

33. Wan, Y.; Shi, Y. F.; Zhao, D. Y. Supramolecular aggregates as templates: Ordered mesoporous polymers and carbons. *Chemistry of Materials* **2008,** *20* (3), 932-945.

34. Liang, C. D.; Hong, K. L.; Guiochon, G. A.; Mays, J. W.; Dai, S. Synthesis of a large-scale highly ordered porous carbon film by self-assembly of block copolymers. *Angew. Chem.-Int. Edit.* **2004,** *43* (43), 5785-5789.

35. Meng, Y.; Gu, D.; Zhang, F. Q.; Shi, Y. F.; Cheng, L.; Feng, D.; Wu, Z. X.; Chen, Z. X.; Wan, Y.; Stein, A.; Zhao, D. Y. A family of highly ordered mesoporous polymer resin and carbon structures from organic-organic self-assembly. *Chemistry of Materials* **2006,** *18* (18), 4447-4464.

36. Deng, Y. H.; Yu, T.; Wan, Y.; Shi, Y. F.; Meng, Y.; Gu, D.; Zhang, L. J.; Huang, Y.; Liu, C.; Wu, X. J.; Zhao, D. Y. Ordered mesoporous silicas and carbons with large accessible pores templated from amphiphilic diblock copolymer poly(ethylene oxide)-b-polystyrene. *Journal of the American Chemical Society* **2007,** *129* (6), 1690-1697.

37. Deng, Y. H.; Liu, J.; Liu, C.; Gu, D.; Sun, Z. K.; Wei, J.; Zhang, J. Y.; Zhang, L. J.; Tu, B.; Zhao, D. Y. Ultra-Large-Pore Mesoporous Carbons Templated from Poly(ethylene oxide)-b-Polystyrene Diblock Copolymer by Adding Polystyrene Homopolymer as a Pore Expander. *Chemistry of Materials* **2008,** *20* (23), 7281-7286.

38. Yamauchi, Y.; Kuroda, K. Rational design of mesoporous metals and related nanomaterials by a soft-template approach. *Chemistry-an Asian Journal* **2008,** *3* (4), 664-676.

39. Yang, P. D.; Zhao, D. Y.; Margolese, D. I.; Chmelka, B. F.; Stucky, G. D. Generalized syntheses of large-pore mesoporous metal oxides with semicrystalline frameworks. *Nature* **1998,** *396* (6707), 152-155.

40. Tian, B. Z.; Liu, X. Y.; Tu, B.; Yu, C. Z.; Fan, J.; Wang, L. M.; Xie, S. H.; Stucky, G. D.; Zhao, D. Y. Self-adjusted synthesis of ordered stable mesoporous minerals by acid-base pairs. *Nature Materials* **2003,** *2* (3), 159-163.

41. Falcaro, P.; Costacurta, S.; Mattei, G.; Amenitsch, H.; Marcelli, A.; Guidi, M. C.; Piccinini, M.; Nucara, A.; Malfatti, L.; Kidchob, T.; Innocenzi, P. Highly ordered "defect-free" self-assembled hybrid films with a tetragonal mesostructure. *Journal of the American Chemical Society* **2005,** *127* (11), 3838-3846.

42. Tian, B. Z.; Liu, X. Y.; Solovyov, L. A.; Liu, Z.; Yang, H. F.; Zhang, Z. D.; Xie, S. H.; Zhang, F. Q.; Tu, B.; Yu, C. Z.; Terasaki, O.; Zhao, D. Y. Facile synthesis and characterization of novel mesoporous and mesorelief oxides with gyroidal structures. *Journal of the American Chemical Society* **2004,** *126* (3), 865-875.

43. Zhang, F. Q.; Meng, Y.; Gu, D.; Yan, Y.; Chen, Z. X.; Tu, B.; Zhao, D. Y. An aqueous cooperative assembly route to synthesize ordered mesoporous carbons with controlled structures and morphology. *Chemistry of Materials* **2006,** *18* (22), 5279-5288.

44. Li, H. Q.; Liu, R. L.; Zhao, D. Y.; Xia, Y. Y. Electrochemical properties of an ordered mesoporous carbon prepared by direct tri-constituent co-assembly. *Carbon* **2007,** *45* (13), 2628-2635.

45. Liang, C. D.; Dai, S. Synthesis of mesoporous carbon materials via enhanced hydrogen-bonding interaction. *Journal of the American Chemical Society* **2006,** *128* (16), 5316-5317.

46. Crepaldi, E. L.; Soler-Illia, G.; Grosso, D.; Cagnol, F.; Ribot, F.; Sanchez, C. Controlled formation of highly organized mesoporous titania thin films: From mesostructured hybrids to mesoporous nanoanatase TiO2. *Journal of the American Chemical Society* **2003,** *125* (32), 9770-9786.

47. Lebeau, B.; Galarneau, A.; Linden, M. Introduction for 20 years of research on ordered mesoporous materials. *Chemical Society Reviews* **2013,** *42* (9), 3661-3662.

48. Ryoo, R.; Joo, S. H.; Jun, S. Synthesis of highly ordered carbon molecular sieves via template-mediated structural transformation. *Journal of Physical Chemistry B* **1999,** *103* (37), 7743-7746.

49. Tian, B. Z.; Liu, X. Y.; Yang, H. F.; Xie, S. H.; Yu, C. Z.; Tu, B.; Zhao, D. Y. General synthesis of ordered crystallized metal oxide nanoarrays replicated by microwave-digested mesoporous silica. *Advanced Materials* **2003,** *15* (16), 1370-+.

50. Shin, H. J.; Ryoo, R.; Liu, Z.; Terasaki, O. Template synthesis of asymmetrically mesostructured platinum networks. *Journal of the American Chemical Society* **2001,** *123* (6), 1246-1247.

51. Yang, H. F.; Zhao, D. Y. Synthesis of replica mesostructures by the nanocasting strategy. *Journal of Materials Chemistry* **2005,** *15* (12), 1217-1231.

52. Dimitrakopoulos, C. D.; Malenfant, P. R. L. Organic thin film transistors for large area electronics. *Advanced Materials* **2002,** *14* (2), 99-+.

53. Li, Q. F.; He, R. H.; Jensen, J. O.; Bjerrum, N. J. Approaches and recent development of polymer electrolyte membranes for fuel cells operating above 100 degrees C. *Chemistry of Materials* **2003,** *15* (26), 4896-4915.

54. Guliants, V. V.; Carreon, M. A.; Lin, Y. S. Ordered mesoporous and macroporous inorganic films and membranes. *Journal of Membrane Science* **2004,** *235* (1-2), 53-72.

55. Rolison, D. R.; Long, R. W.; Lytle, J. C.; Fischer, A. E.; Rhodes, C. P.; McEvoy, T. M.; Bourga, M. E.; Lubers, A. M. Multifunctional 3D nanoarchitectures for energy storage and conversion. *Chemical Society Reviews* **2009,** *38* (1), 226-252.

56. Tanev, P. T.; Pinnavaia, T. J. A NEUTRAL TEMPLATING ROUTE TO MESOPOROUS MOLECULAR-SIEVES. *Science* **1995,** *267* (5199), 865-867.

57. Zhao, D. Y.; Feng, J. L.; Huo, Q. S.; Melosh, N.; Fredrickson, G. H.; Chmelka, B. F.; Stucky, G. D. Triblock copolymer syntheses of mesoporous silica with periodic 50 to 300 angstrom pores. *Science* **1998,** *279* (5350), 548-552.

58. Wang, X. Q.; Liang, C. D.; Dai, S. Facile synthesis of ordered mesoporous carbons with high thermal stability by self-assembly of resorcinol-formaldehyde and block copolymers under highly acidic conditions. *Langmuir* **2008,** *24* (14), 7500-7505.

59. Mayes, R. T.; Tsouris, C.; Kiggans, J. O.; Mahurin, S. M.; DePaoli, D. W.; Dai, S. Hierarchical ordered mesoporous carbon from phloroglucinol-glyoxal and its application in capacitive deionization of brackish water. *Journal of Materials Chemistry* **2010,** *20* (39), 8674-8678.

60. Sun, X. M.; Zhang, Z. T.; Guan, G. Z.; Qiu, L. B.; Peng, H. S. The synthesis of porous materials with macroscopically oriented mesopores interconnected by branched mesopores. *Journal of Materials Chemistry A* **2013,** *1* (15), 4693-4698.

61. Igor Zlotnikov, P. W., Horst Blumtritt, Andreas Graff, Yannicke Dauphin, Emil Zolotoyabko, Peter Fratzl. A Perfectly Periodic Three-Dimensional Protein/Silica Mesoporous Structure Produced by an Organism. *Advanced Materials* **2014,** *26* (11), 1682-1687.

62. Huang, E.; Rockford, L.; Russell, T. P.; Hawker, C. J. Nanodomain control in copolymer thin films. *Nature* **1998,** *395* (6704), 757-758.

63. Villar, M. A.; Rueda, D. R.; Ania, F.; Thomas, E. L. Study of oriented block copolymers films obtained by roll-casting. *Polymer* **2002,** *43* (19), 5139-5145.

64. Kim, S. H.; Misner, M. J.; Xu, T.; Kimura, M.; Russell, T. P. Highly oriented and ordered arrays from block copolymers via solvent evaporation. *Advanced Materials* **2004,** *16* (3), 226-+.

65. Hara, M.; Nagano, S.; Seki, T. pi-pi Interaction-Induced Vertical Alignment of Silica Mesochannels Templated by a Discotic Lyotropic Liquid Crystal. *Journal of the American Chemical Society* **2010,** *132* (39), 13654-13656.

66. Liang, C. D.; Li, Z. J.; Dai, S. Mesoporous carbon materials: Synthesis and modification. *Angew. Chem.-Int. Edit.* **2008,** *47* (20), 3696-3717.

67. Xia, Y. D.; Yang, Z. X.; Mokaya, R. Templated nanoscale porous carbons. *Nanoscale* **2010,** *2* (5), 639-659.

68. Zhang, F. Q.; Meng, Y.; Gu, D.; Yan, Y.; Yu, C. Z.; Tu, B.; Zhao, D. Y. A facile aqueous route to synthesize highly ordered mesoporous polymers and carbon frameworks with Ia(3)over-bard bicontinuous cubic structure. *Journal of the American Chemical Society* **2005,** *127* (39), 13508-13509.

69. Lee, J.; Kim, J.; Hyeon, T. Recent progress in the synthesis of porous carbon materials. *Advanced Materials* **2006,** *18* (16), 2073-2094.

Chapter 2: Templated synthesis of large-pore, three-dimensionally ordered mesoporous carbon thin films

2.1 Introduction

Among classes of mesoporous materials bearing high surface area, three-dimensionally ordered pore topology, and large pore volumes, ordered mesoporous carbons (OMCs) have attracted specific interest due to their low cost, thermal and physicochemical stability and electrical conductivity, properties that make them attractive for applications as diverse as electrodes in energy conversion and storage devices, supercapacitors, catalysts, and adsorbents.[1, 2, 3, 4] A range of methods have been realized for scalable synthesis of mesoporous carbon powders since early demonstration of nanocasting strategies on ordered mesoporous silicas by Ryoo *et al*.[5] and Hyeon *et al*,[6] and direct synthesis strategies via so-called soft-templating pioneered by Dai and co-workers.[7, 8] Translation of these powder approaches to realization of ultra-thin (i.e., nanometer to sub-micron) porous carbon films with desired properties has garnered significant research focus,[8, 9, 10, 11, 12, 13, 14] owing to the promise that thin films hold for applications spanning electronics, sensing, and membranes, among others.[15] Challenges faced when transitioning from powders to thin films include realizing facile tunability of film thickness and morphology, controlling pore size and its structural robustness, and achieving accessible and orientated film-spanning 3D-interconnected and ordered pore topologies.

So-called ‘soft-templating’ or ‘direct’ strategies that exploit the self-assembly phase behavior of copolymer surfactants as templates and polymerizable carbon precursors by evaporation induced self-assembly (EISA) can be used to realize ordered mesoporous carbon films.[8, 9, 12, 13, 16, 17, 18] The assembly process occurs by hydrogen-bonding interactions that drive the organic-organic assembly of surfactants and carbon precursors, with subsequent decomposition of template molecules and thermally induced carbonization of the remaining mesoporous polymeric

materials leading to mesoporous carbon films. While such processes enjoy scalability, owing to their reliance on 'one-pot' solution phase thermodynamics, they do face several critical drawbacks. Namely, soft-templating processes face the cost of sacrificing surfactant templates or specific polymer blocks, uniaxial pore shrinkage due to anisotropic thin-film stresses,[13, 19] limitations on the types of carbon sources amenable to assembly[2] and thus stifled tunability of intrinsic properties of the derived carbons, and difficulties in realizing facile control over the orientation and thereby accessibility of pores due to interface-driven preferential segregation and orientation of the pore forming phase (e.g., micelles) parallel rather than perpendicular to the substrate upon which they are cast.[9, 16, 20] Overcoming the latter typically requires solvent annealing steps,[17] imposition of external fields,[18] or interface control.[16]

Alternative hard-templating methods commonly involve impregnation of silica templates with carbon precursors, which are polymerized and carbonized prior to selective etching of the silica framework.[1, 21] This approach typically adopts pre-synthesized surfactant-templated (e.g., SBA, MCM, KIT, MSU-H, HMS)[3, 4, 5, 6, 22] or colloidal[23, 24, 25, 26, 27] porous silicas as templates, but has been challenged by the need to fashion thin-film templates from materials more commonly processed in powder form. Specific difficulties derive, in part, from multi-step synthesis possibly requiring the surfactant-templated pre-fabrication of ordered mesoporous silica films followed by costly surfactant sacrifice, inaccessible porosity therein,[28] a problem akin to challenges faced in soft-templating of carbon films,[13] general lack of suitably scalable template films, and disorder and sometimes discontinuity in some meso-structured template films.[10] In addition, with early hard templating efforts primarily employing chemical (CVD) or physical vapor deposition (PVD),[11, 23] replication has been limited primarily to conformal coatings of the pore wall of the template under vacuum conditions or the need for repetitive carbonization steps for full replication of those template features. Film continuity and substrate adhesion are also believed to plague earlier hard-templating efforts.

Here, we address the drawbacks associated with hard templating of porous thin films through establishment of a tunable and robust strategy for realizing large-pore, 3DOm carbon thin films that is also capable of overcoming some of the intrinsic challenges associated with soft-templating approaches (e.g., pore orientation/accessibility, uniaxial pore shrinkage, carbon precursor versatility). Enabling this work is the ability to realize surfactant-free assembly of continuous three-dimensionally ordered mesoporous (3DOm), thickness-tunable colloidal crystal films as templates. Previous reports have established how particles ranging in size from micron and sub-micron to as small as ca. 10 nm can be assembled into area-scalable colloidal crystalline thin films by evaporation-induced convective deposition either by dip-coating[29, 30] or blade-based processes.[31, 32, 33] In both processes, a solid substrate is brought in contact with a particle solution, yielding a meniscus and triple phase boundary where particulate coatings are formed. Solvent evaporation drives particle convection through the sol to the contact line where capillary forces within the thin solvent layer pin particles in an ordered colloidal crystalline array on a substrate advancing at a prescribed rate. Handles for tuning the thickness of convectively deposited colloidal crystal films include parametric control over solids content, deposition rate, and evaporation rate, the latter modulated, for example, by humidity control.

In lieu of EISA techniques wherein mesoporous silica films result from surfactant-templated self-assembly and polymerization of silicate precursors followed by sacrifice of the pore forming micellar phase,[28, 34] convectively assembled nanoparticle-based colloidal crystal films are endowed with 3D-interconnected mesopore volume that is effectively self-templated since it derives simply from the interstices formed from template-free particle assembly. Herein, we exploit the large interstitial pore volume of tunable nanoparticle crystalline films for templating 3DOm carbon films. The tunability of the template films translates to facile control over the feature pore size, film thickness, morphology, and texture.

We first demonstrate the tunable synthesis of such crystalline nanoparticle silica films. Subsequent methods for uniform carbon replication of these tunable films and their polymer-

assisted transfer among various substrates will be described, with a discussion of key factors found to help bridge the materials gap between powder and thin film replication on ideal to non-ideal substrates (i.e., ones bearing surface roughness far exceeding the size of the primary template particles). Finally, we use dye-sensitized solar cells (DSSCs) as a test-bed to begin to elucidate the structure-function relations for the films developed herein when applied as low-cost alternatives to conventional platinum-based counter-electrodes.

2.2 Materials and Methods

2.2.1 Materials

The following reagents were used without further purification: tetraethyl orthosilicate (TEOS, Acros Organics, 98%), sulfuric acid (H_2SO_4, 98%, Sigma Aldrich), L-lysine (Sigma Aldrich, 98%), furfuryl alcohol (FA, Acros Organics, 98%), oxalic acid (OA, Acros Organics, 98%), potassium hydroxide (KOH, BDH), and sucrose (Sigma Life Science, 99.5%) were obtained from Sigma-Aldrich. Phenol (99%), resorcinol (99%), and hydrofluoric acid (HF, 49%) were obtained from Alfa Aesar; hydrogen peroxide (30% wt.) and formaldehyde (37% wt. in water) were obtained from Fisher Scientific; sodium carbonate (99.5%) was obtained from VWR; poly(methyl methacrylate) (PMMA, MW of 75,000) was obtained from Polysciences Inc.; polydimethylsiloxane (PDMS) reagents (Sylgard® 184 silicone elastomer base and curing agent) were obtained from Dow Corning. Silicon wafers were purchased from Silicon Quest Int. and FTO-glass (TEC-8) was obtained from Pilkington North American. Solaronix Ti-Nanoxide, Platisol T/SP, Solaronix Iodolyte AN-50 electrolyte, and Solaronix Ruthenizer 535-bisTBA (Solaronix N719, prepare 0.3 mM solution in tert-butanol (Sigma Aldrich, 99.7%), acetonitrile (Acros Organics, 99.9%) with volume ratio of 1:1), and carboxymethyl cellulose (Sigma Aldrich) were used as received without further purification. Millipore water with resistivity 18 M□ was used for all reactions.

2.2.2 Silica nanoparticle sol synthesis

Typically, L-lysine was dissolved in water under vigorous stirring for 0.5 hr within an oil bath at 90°C. TEOS was subsequently hydrolyzed in the aqueous L-Lysine solution at 90°C under vigorous stirring for at least 12 hrs. Silica nanoparticles of ca. 20 nm in diameter were synthesized directly, with a final molar composition, x SiO_2/ y Lysine/ z water/ $4x$ ethanol, of x=60, y=1.23, z=4750. Sols of larger ca. 30 nm (x=210, y=1.23, z=4750), 40 nm (x=500, y=1.23, z=9500) and 50 nm (x=950, y=1.23, z=9500) diameter particles were prepared through a seeded growth process, in which 3-4 aliquots of TEOS were added to sols of the prepared ca. 20 nm particles until the prescribed molar composition was reached, with intermediate hydrolysis at 90°C for at least 12 hrs following each aliquot addition. Dialysis of the resulting silica suspension was carried out against water for 3 days with mild stirring using Spectra/Por® dialysis bags (Spectrum Labs, 3500 molecular weight cutoff). Water was exchanged every 8 hrs during dialysis until pH~5.5 was reached.

2.2.3 Silica colloidal crystal thin film templates

A lab-scale convective coating device, described in detail in Ref. [33], was used to prepare silica nanoparticle template films. 50μL of the nanoparticle sol was held in the space between the substrate and a glass blade (i.e., glass microscope slide with the bottom edge made hydrophobic by attaching parafilm), the latter fixed in close (~0.5 mm) proximity and at an angle of 45° to the underlying substrate. A linear motor is employed to drive the underlying substrate at a prescribed speed relative to the fixed blade while capillary forces hold the nanoparticle sol between the blade and substrate. All convective coatings were carried out at room temperature, ambient humidity of ca. 55%, and prescribed substrate draw speeds of 5 μm/s, 10μm/s or 20μm/s.

Silicon wafer substrate In the case of coatings prepared on silicon wafers, substrates were first cleaned of all organic contaminants using Piranha solution (3:1 volumetric mixture of sulfuric acid and hydrogen peroxide), followed by rinsing with water and drying with a jet of dry

nitrogen. Calcination of the silica nanoparticle films prepared on Si wafers was carried out for 3 hrs (5^{o}C/min ramp, 3 hr soak) at 1000^{o}C.

FTO glass substrate In the case of coatings made on FTO-glass, the substrate was first immersed in a 0.1M hydrochloric acid solution in ethanol for 30 min and then rinsed with ethanol and dried with a jet of dried nitrogen. Calcination of the silica nanoparticle films prepared on FTO glass substrates was carried out for 3 hrs (5^{o}C/min ramp, 3 hr soak) at 600^{o}C.

2.2.4 Carbon films by template replication

Carbon replication of colloidal crystal thin film templates was carried out with carbon sources of the following mass compositions: 1) furfuryl alcohol/oxalic acid (100/1 FA/OA), 2) phenol-formaldehyde (0.58/0.12/1.0 phenol/KOH (20%wt)/formaldehyde), 3) resorcinol-formaldehyde (0.68/0.013/0.64/1.0 resorcinol/sodium carbonate/water/formaldehyde), and 4) sucrose (0.25/0.002/1.0 sucrose/sulfuric acid/water).

Precursor vapor infiltration (PVI) In the case of PVI, employed for replication with FA/OA, the silica template film was suspended horizontally 0.5 inch above a pool of FA/OA solution in a sealed plastic beaker. The sealed container was heated at 90°C for 12 hrs, driving deposition of polymerizing monomer vapor into the porous thin film structure. Controlled duration of the PVI process or tuning of the volume of the FA/OA source solution was used to tune replica film thickness.

Precursor immersion/spin-off (PIS) In the case of PIS, applicable for all carbon precursors studied here, the supported silica colloidal crystal film was immersed in the prescribed monomer solution for 30 minutes with excess monomer solution removed by sample spinning on a Laurell® Tech. Corp. WS-650MZ-23NPP/LITE spin-coater.

Polymerization, carbonization, and template etching Polymerization of the template-infiltrated carbon precursors was carried out at conditions specific to the carbon source: 90°C for 12 hrs in the case of FA/OA, 100°C for 24 hrs in the cases of phenol-formaldehyde and sucrose,

and 85°C for 3 days in the case of resorcinol-formaldehyde. Resulting silica-polymer composites supported on silicon wafers were carbonized in a tube furnace under flowing nitrogen (1.5 L/min), first at 200°C (5°C/min ramp, 3 hr soak) and then at 900°C (5°C/min ramp, 3 hr soak). After cooling to room temperature, the silica was selectively etched from the carbon-silica composite film by dropping dilute HF (5% wt.) onto the film surface in a sufficient quantity (ca. 2 mL) to coat the ca. 1 in. x 1.5 in. film. HF was rinsed from the surface of the carbon replica film after 2 hours, using copious amounts of water and ethanol. In the case of silica-polymer composites supported on FTO-glass substrates, more mild carbonization was carried out in a tube furnace under flowing nitrogen (1.5 L/min) at 200°C (5°C/min ramp, 3 hr soak) and a maximum temperature of only 600°C (5°C ramp, 3 hr soak). Subsequent selective etching of the silica template was achieved in a similar fashion as described for films supported on silicon wafers, with KOH (30% wt.) employed instead as the etching agent. The samples were carefully washed after 2 hours using copious amounts of water and ethanol. Persistence of the FTO crystalline structure and corresponding conductivity during the KOH etching process was confirmed by SEM and ohmmeter measurements, respectively.

2.2.5 3DOm carbon reference powders

Bulk colloidal crystal silica templates were synthesized as reference materials by evaporative drying of dialyzed Lys-Sil nanoparticle sols at 70°C. The resulting silica powders were calcined at 600°C for 3 hrs. Carbon replication of the powders was completed by incipient wetness techniques described in Ref. [35]. Specifically, FA/OA solution was introduced into the void space between particles (e.g., 1 g silica colloidal crystalline powder, 0.195 mL FA/OA solution) and allowed to age overnight to ensure complete infiltration, with subsequent polymerization and carbonization identical to the thin film processing. Silica template removal was carried out by HF (5% wt) or KOH (30% wt) etching with stirring at room temperature or etching with 6M KOH solution and activation at 180°C for 3 days in Teflon-lined stainless steel autoclaves.

2.2.6 Carbon film transfer among substrates

PDMS and PMMA (20% wt. in acetone) were used as transfer medium to move films among substrates. In the case of PDMS, Sylgard® 184 base and curing agent, were mixed in a 10:1 weight ratio and bubbles were removed under vacuum for 30 min. PDMS or PMMA were deposited on top of the carbon films by spin coating for 30 sec at 1000 RPM. Solidification of the polymer coatings was carried out at 80°C for 2 hours in the case of PDMS, and through 2 hr evaporation of acetone in the case of PMMA. Subsequent immersion of the carbon-polymer composite film in 30% wt. KOH solution for at least 4 hours resulted in delamination from the silicon wafer. The resulting film, supported on PDMS or PMMA, was carefully rinsed with copious amounts of water or ethanol, transferred to other substrates (e.g., plastic/metal sheets, glass slide, porous support, paper), and finally dried in air. Transfer was accomplished by simply pressing the polymer-backed carbon film onto the target substrate, with removal of the polymer transfer medium by simple peeling in the case of PDMS or acetone-induced dissolution in the case of PMMA.

2.2.7 Characterization

Scanning electron microscopy (SEM) was carried out on samples coated with Iridium using a Hitachi 4300 FE-SEM with accelerating voltage of 5-10 kV. Transmission electron microscopy (TEM) images were obtained on a JEOL 2000FX with accelerating voltage of 200 kV. Nitrogen adsorption isotherms were measured on porous carbon powders to determine representative textural properties of the porous films. Isotherms were measured at 77 K on a Micromeritics ASAP 2020 instrument. Prior to adsorption measurements, all samples were degassed under vacuum (5μm Hg) at 350°C for more than 12 hrs. The Brunauer-Emmett-Teller (BET) method is applied to estimate the total specific surface area. The total pore volume (V_t) was estimated from the adsorbed amount at a relative pressure P/P_0 of 0.995. Micro- and mesopore analysis was based on t-plot methods, and Barrett-Joyner-Halenda (BJH) analysis applied to the adsorption and

desorption branches was used for estimation of the size distribution of pore bodies and pore windows, respectively.

2.2.8 Dye-sensitized solar cell (DSSC) fabrication, packaging, and testing

DSSC photoanodes were prepared by depositing a ca. 15 □m thick coating of Solaronix Ti-Nanoxide D paste on the FTO-surface using a doctor blade technique. After drying, the photoanode was treated at 500°C for 2 hrs. The cooled photoanode was subsequently immersed for 12 hrs in a 0.3 mM Solaronix N-719 dye solution prepared in a 50/50 volumetric mixture of acetonitrile and tertbutyl alcohol. As a lab performance standard, a conventional platinum cathode was prepared on FTO glass by convective blade-coating of Platisol T/SP, followed by thermal treatment at 400°C for 30 min. Alternative cathodes included carbon films described herein either transferred to or directly deposited on FTO glass substrates. Reference counter-electrodes coated with 3DOm carbon powder were typically prepared by convective deposition of 100 □L of sonicated (30 min) dispersions of 0.2 g of 3DOm carbon powder in 20 mL of DI-water containing 0.02 g carboxymethyl cellulose (Sigma Aldrich) onto FTO glass substrates.

Working DSSCs were assembled with a 50 μm thick hot-melt gasket made of Surlyn film between the anode and cathode. Commercial grade Iodolyte AN 50 electrolyte was injected into the 50μm thick reservoir between the heat-sealed anode and cathode using injection ports bored through the FTO glass. Ports were subsequently sealed with a Surylyn film and cover glass. The photocurrent density and voltage of the DSSCs were measured over a 1cm^2 area using a Solar Simulator with AM 1.5G filter (Abet Technology) at 100 mW/cm^2 25^{o}C and Solar Module Analyzer (PROVA 200, TES Electrical Electronic Corp). Overall cell efficiency, η, is calculated as $\eta = J_{SC} \cdot V_{OC} \cdot FF/P$, where J_{SC} is the short-circuit current, V_{OC} is the open-circuit voltage, and P is the power density of the incoming light. FF is the so-called fill factor, defined as $FF = J_m V_m / J_{SC} V_{OC}$, where V_m and J_m are the voltage and current density corresponding to the maximum power density.

2.3 Results and Discussion

2.3.1 Tunable porous thin film templates

We first establish convective deposition parameters that enable realization of uniform ordered colloidal crystal thin films of tunable thickness and feature size (i.e., particle size). As described previously,[33] the process of convective deposition involves sweeping a meniscus of a nanoparticle sol across a substrate at a controlled rate, with particle convection to and capillary pinning at the contact line formed between the sol and substrate. This scalable process enables single-pass coatings of mono- to multi-layer nanoparticle crystalline films. Figure 2.1 shows representative cross-sectional and plan view SEM images of colloidal crystalline films composed of 50 nm silica nanoparticles achieved by their convective deposition on silicon wafers. The resulting films are comprised of close-packed nanoparticulate structures in single crystal-like domains separated by cracks and/or grain boundaries (arrows, Figure 2.1d). The latter arise as a result of capillary forces during film drying.[29]

With solution and environmental parameters (e.g., humidity and thereby evaporation rate) held constant, the thickness of the multi-layer colloidal crystal films can be adjusted by controlling the rate at which the substrate is advanced during the coating process. As shown in Figures 2.1a and 2.1b for representative nanoparticle sols composed of 50 nm particles and prescribed coating conditions (3.44% vol., 50 nm silica, 24°C, ca. 55% humidity), tuning the coating rate from 5μm/s to 20 μm/s leads to colloidal crystal films of ca. 400 nm (8 layers) to ca. 140 nm (3 layers), respectively. We find that uniformity of the thickness of the deposited film requires removal (i.e., by dialysis) of excess ethanol from the as prepared Lys-Sil nanoparticle sols prior to convective coating. This removal of ethanol results in purely aqueous nanoparticle sols, ensuring a constant rate of solvent evaporation at the drying front provided that constant humidity conditions are maintained during the coating process.

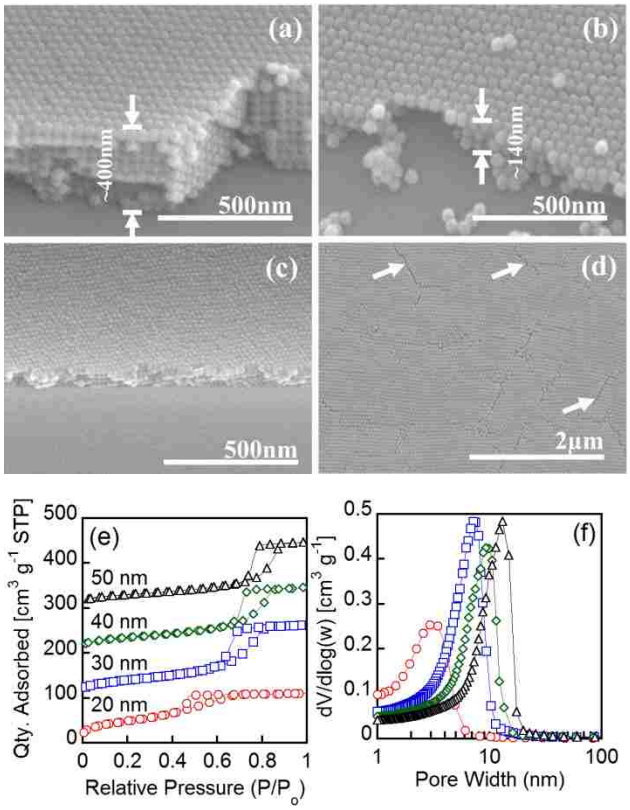

Figure 2.1: Cross-sectional SEM images of crystalline Lys-Sil nanoparticle films comprised of (a,b,d) ca. 50 nm to (c) ca. 20 nm silica nanoparticles. Film thickness is tunable by coating rates as shown for (a) 5µm/s to (b,c) 20µm/s, with (d) intrinsic defects (e.g., cracks, grain boundaries denoted by arrows on SEM) observed on the top surface of the films. Nitrogen adsorption collected on colloidal crystal powders composed of particles of prescribed diameter are shown in (e), with corresponding pore size distribution (f) calculated from BJH analysis of the adsorption branches.

The ultimate resolution by which the thickness of the colloidal crystal film can be tuned is a function of the coupled control over mono- to multi-layer coatings and the size of the assembled particles. As shown in Figure 2.1c, convective deposition can accommodate assembly of Lys-Sil nanoparticles of sizes spanning ca. 20 nm to 50 nm,[35, 36, 37] with previous reports establishing that Lys-Sil particles as small as ca. 10 nm in diameter can also be assembled with near-monolayer to multilayer thickness.[29] Tuning the size of nanoparticles comprising the template directly impacts the pore size of the resulting replica materials, a dimension intrinsically coupled to the thickness of the pore walls within the replica structures.

Quantitative insight into the tunable size of the colloidal crystal interstices is achieved by nitrogen physisorption. Figure 2.1e shows nitrogen adsorption isotherms collected on bulk colloidal crystal powders prepared with particles of the same size and under identical conditions (i.e., convective drying) as those used for thin film formation. The hysteresis loops of the resulting isotherms are indicative of the mesoporosity defined by the colloidal crystal interstices. The corresponding size of these interstices, extracted by BJH analysis of the adsorption branch (Figure 2.1f), systematically increases with increasing particle size, consistent with the concomitant shift to higher relative pressures of the hysteresis loops. This analysis suggests that replica wall thickness should be tunable from ca. 3 nm to more than 10 nm with concomitant tunability of the pore body size.

2.3.2 3D ordered mesoporous (3DOm) and mesopore-supported carbon replica films

The facile ability to assemble colloidal crystal films of tunable thickness and primary particle size with long-range, three-dimensional order marks a key advance enabling establishment of important synthetic approaches for bridging the materials gap between powder replication processes[35, 37] and the apparently elusive[10, 11] sacrificial hard-templating of meso- and hierarchically structured carbon films. Namely, it provides a surfactant-free and facile means for realizing nanometer-scale thin films with ordered, size-tunable, and highly accessible porosity facilitating high-fidelity replication.

Here, we describe two strategies for complete carbon replication of the colloidal crystal thin films, differing primarily in the methods employed for introducing the carbon precursor into the interstitial spaces of the template. The methods include a precursor vapor infiltration (PVI) approach, which we demonstrate for controlled infiltration of a common furfuryl alcohol/oxalic acid (FA/OA) precursor solution, and a precursor infiltration and spin-off (PIS) approach, amenable to a wide range of carbon precursors. These methods enable realization of open mesoporous and mesopore-supported thin carbon films derived from a wide range of carbon

precursors and bearing tunable porous morphologies. The 3D-ordered mesopore (3DOm) topology within the replica films is templated by the sacrificial nanoparticles comprising the colloidal crystal thin film template, with pore windows formed by the exclusion of carbon replication media at the point of contact between adjacent template particles.

As schematized in Figure 2.2b, the PVI approach involves vaporization of an FA/OA solution in the presence of the silica colloidal crystal film, resulting in simultaneous precursor deposition and partial polymerization within the interstices, grain boundaries, and cracks alike of the film. Subsequent in situ processing (e.g., polymerization, carbonization) and selective template sacrifice results in various film morphologies including open, three-dimensionally ordered mesopore (3DOm) topologies (Figure 2.2c) and 3DOm-supported thin carbon films (Figure 2.2d-f) dependent upon the degree to which the silica templates are filled or over-filled, respectively, with FA/OA precursor solution during PVI processing. Namely, incomplete filling of the template film results in an open 3DOm film morphology upon template etching (Figure 2.2c and SI Figure S2.1), whereas systematic overfilling of the colloidal crystal template leads to ultra-thin over-layers supported atop a 3DOm carbon film (Figures 2.2d-2.2f). In the case of the latter, the thickness of both layers of the film can be independently tuned; the 3DOm layer by controlling the thickness of the precursor silica template film (e.g., Figures 2.1, 2.2d and 2.2e), and the carbon over-layer by modulating the duration of PVI processing or simply by adjusting the volume of the precursor solution (Figure 2.2f and Figure S2.2). Therefore, the PVI process, and the PIS process that we describe later, provide a facile means for easily selecting between, and tuning the thickness of, 3DOm and over-layer film morphologies without the need for complex and costly processes of polishing, controlled etching or specially designed flow/infiltration cells as reported for macroscopic film fabrication.[38, 39]

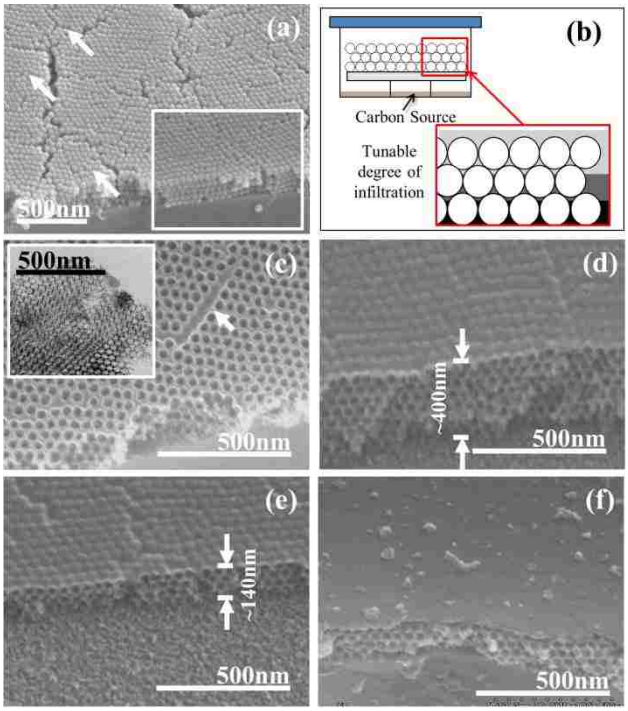

Figure 2.2: SEM images of (a) the 50nm silica film template after calcination to 1000°C (inset, pre-calcination morphology), and the carbon replication of similar colloidal crystal films by the PVI method, schematized in (b), and following selective silica sacrifice. PVI conditions dictate the degree of filling of the template, yielding (c) open, 3DOm carbon films, (d,e) carbon-topped 3DOm films, the thickness of which is tunable by the thickness of the colloidal crystal film template, with (f) the over-layer thickness tunable by duration of PVI treatment or volume of precursor solution. Arrows in (a) and (c) indicate grain boundaries/cracks that open in the template during calcination and carbon healing of defect structures during replication, respectively.

Evidence of long-range mesopore order and defect healing is illustrated by the lower magnification SEM images of both the open 3DOm and 3DOm-supported over-layer film morphologies in SI Figures 2.1 and 2.2, respectively. The complete filling of template interstices and larger defects (e.g., grain boundaries, cracks) alike (e.g., arrow, Figure 2.2c), coupled with the tunability of the open and ordered porous replica film thickness, suggests that replica films are formed by a deposition front that advances normal to the underlying substrate. This requires uniform, three-dimensional propagation of the precursor deposition front among the interconnected interstitial features of the template. Vapor condensation likely occurs at the template-substrate interface as well as on the large surface area of the colloidal crystal film itself.

Yet, the final replica films display carbon walls that appear to result only from complete filling of the octahedral and tetrahedral interstices of the colloidal template as opposed to conformal coating of the template surfaces as has been observed in studies employing gas-phase chemical deposition.[11, 23] This may result from condensation and gravity-driven drainage of carbon precursor as a source for the deposition front that advances normal to the substrate.

The practical implication of the complete filling of interstices, defects, and grain boundaries of the template film is that the only accessible and film-spanning pore topology within the replica structure is comprised exclusively of spatially ordered, three-dimensionally interconnected spherical pore bodies once occupied by the size-tunable silica template particles. This could have implications for these films as highly selective membranes for macromolecular sieving. The specific size of the pore bodies can be controlled with nanometer resolution by exploiting the tunable size of the template silica particles. This can be seen in the cross-sectional SEM images in SI Figure 2.3 wherein 3DOm replicas of colloidal crystalline films comprised of silica nanoparticles spanning ca. 20 nm to 50 nm are shown.

Corresponding nitrogen physisorption analysis carried out on 3DOm carbon powders derived from four representative template particle sizes are shown in Figure 2.3a, with BJH pore size distributions of pore bodies and pore windows calculated from the adsorption (Figure 2.3b) and desorption (Figure 2.3c) branches, respectively. Adsorption isotherms display a sharp capillary condensation step indicating the presence of mesopores of a highly uniform size. The systematic shift of the hysteresis loop to higher relative pressure with increasing template particle size is indicative of the tunable mesopore body size, confirmed through the pore size distribution (Figure 2.3b) extracted from BJH analysis of the adsorption branch. Intrinsic tunability of the size of the pore window connecting adjacent pore bodies[40] is indicated by the BJH pore size distributions in Figure 2.3c, extracted from the desorption branches of the isotherms. Comparison of textural properties of the 3DOm carbon replicas based upon etching agents (KOH, HF) and conditions (room temperature, 180^{o}C) applied within this paper is provided through comparative nitrogen

adsorption and textural analysis in SI Figure 2.4 and SI Table 2.1, with recognition of the intrinsic limitations of the BJH model when applied to cage-like structures as opposed to cylindrical mesopores for which it was designed. In the case of materials etched with HF at room temperature, wherein microporosity within the carbon replica walls is not activated[41], the specific surface area of the carbon replicas is, in most cases, within almost 20% of the surface area associated with the silica templates, indicating that high-fidelity 3D carbon replication has been achieved.

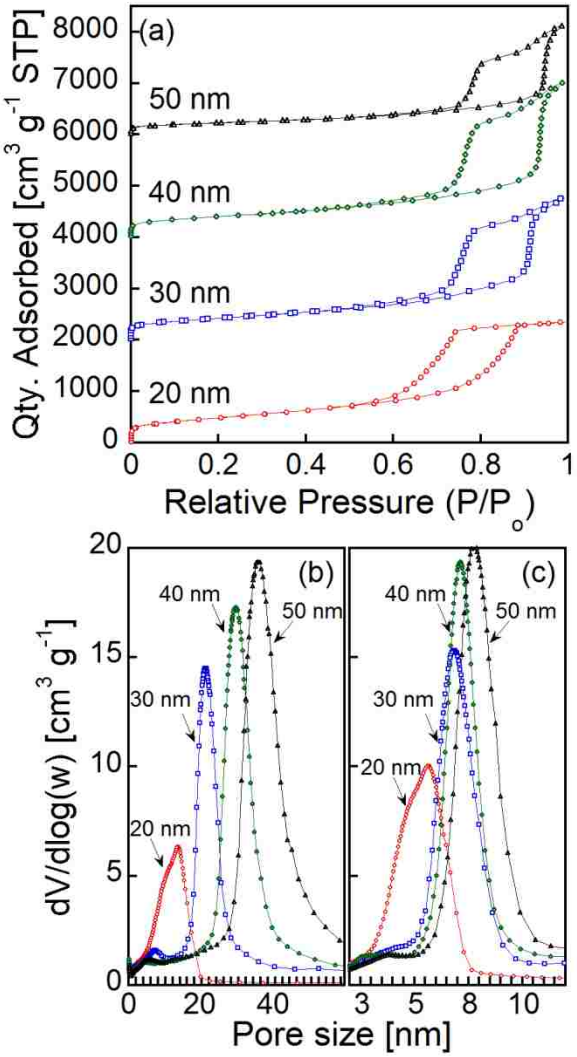

Figure 2.3: (a) Nitrogen adsorption isotherms (shifted vertically for clarity) collected on representative carbon replica powders templated on silica colloidal crystals of prescribed size, with selective template etching carried out with KOH at 180°C. BJH pore size distributions extracted from the (b) adsorption and (c) desorption branches indicate the pore body and pore window size, respectively.

2.3.3 Accommodating carbon source variety

The demonstrated viability of the templating strategy described here motivates extension to other carbon sources that bear precursor-specific intrinsic material properties (e.g., carbon molecular sieving (CMS) character, conductivity, microporosity, etc.). To this end, one benefit of the multi-step hard templating approach is the separation of the template synthesis from the carbon film formation. This separation allows for introduction of a comprehensive range of carbon sources beyond FA/OA. Namely, in addition to the FA/OA precursor, we have explored various common carbon sources, including phenol-formaldehyde, resorcinol-formaldehyde and sucrose-sulfuric acid. In each of these cases, solution composition and/or relative volatility thereof preclude PVI based replication methods.

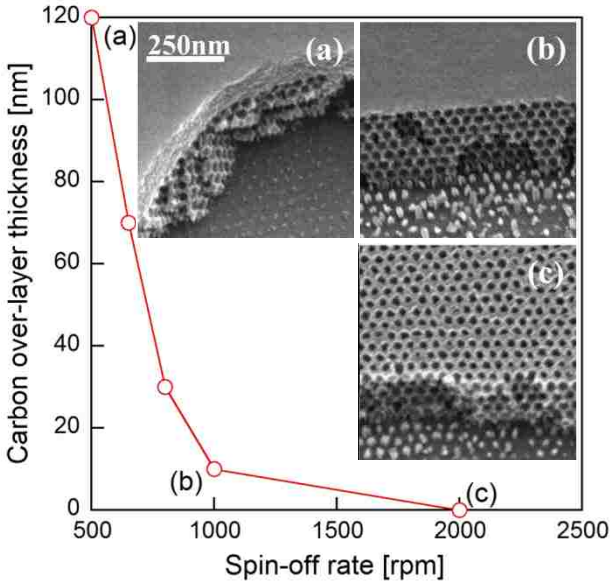

Figure 2.4: Demonstration of the decrease in carbon overlayer thickness and emergence of an open 3DOm carbon replica film structure with increasing spin-off rate intended to remove excess carbon source (here, phenol-formaldehyde) following precursor immersion and spin-off (PIS) processes.

Instead, we demonstrate that simple precursor immersion strategies (PIS) can be used to successfully infiltrate monomer solutions into the silica colloidal crystal template film, with subsequent spin-off of excess monomer solution enabling realization again of both open 3DOm

and 3DOm-supported ultra-thin carbon film morphologies. As shown in the experimentally derived correlation and complementary cross-sectional SEM images in Figure 2.4 for the example of phenol-formaldehyde, the rate of monomer spin-off can be employed as a means to control the absence or presence of the carbon over-layer, and, if present, its ultimate thickness. Namely, the thickness of the carbon top layer on the final 3DOm-supported replica film can be controlled simply by increasing monomer spin-off rates. We have found similar PIS control over mesostructure and film morphology in the case of other carbon sources such as resorcinol-formaldehyde, sucrose/sulfuric acid and FA/OA solutions (SI Figure 2.5).

2.3.4 Factors influencing translation from powder to thin film replication

Here, we highlight distinct aspects of the approaches described above that appear to play an important role in circumventing challenges plaguing earlier reported attempts at realizing hard-templating of ordered mesoporous or mesopore-containing thin films. One clear benefit of hard- relative to soft-templating is the apparent resistance to significant uniaxial pore shrinkage, common in the case of soft-templating.[12, 13, 19] This can be attributed to the role that the hard silica template plays in bolstering the carbon structure during high-temperature polymerization and carbonization processes. In addition, the bottom-up filling of the colloidal crystal template, coupled with the uniformity of the contact between the template film and the underlying substrate, seems to facilitate conformance of the replica film to the support surface and complete percolation of the 3DOm pore topology through the thickness of the film. This is revealed by the SEM image of the bottom side of the replica film (Figure 2.5a), which shows an ordered array of pores penetrating the uniform surface. These perforations of the underside of the film derive from exclusion of the precursor solution at points of contact between the colloidal crystalline template and the substrate.

The uniformity of the replica-substrate interface may be critical for bolstering film stability and adherence during processing and template sacrifice. Indeed, we find that only a short etching

time is required to fully remove the silica template, resulting in a completely intact replica film. This suggests that the nanometer scale film dimensions and associated time scales for etching of amorphous silica must be sufficient to minimize non-specific etching of the replica-substrate interface. In fact, extending the duration of etching beyond what is required to remove only the template leads to film delamination, a characteristic exploited later in the context of film transfer, and one that takes advantage of the apparent intrinsic flexibility of the replica films (Figure 2.5b), owing most likely to the sub-critical carbon film thickness (i.e., less than 1 μm).[42]

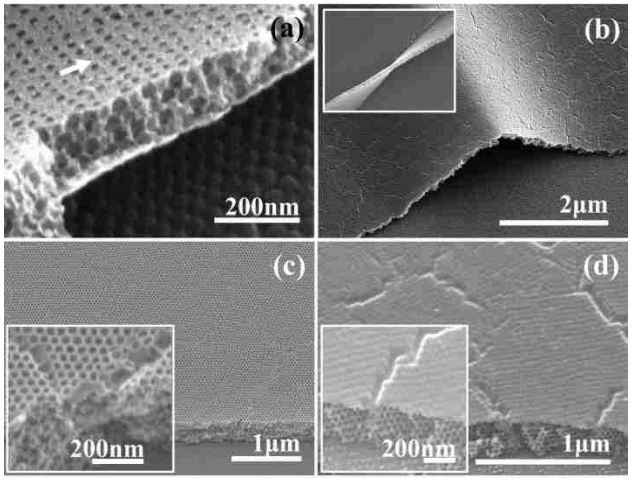

Figure 2.5: Cross-sectional SEM images showing (a) the uniform pore structure and film morphology on the underside (arrow) of a carbon replica film, (b) the apparent flexibility of the ultra-thin carbon replica films (inset, showing flexible band and inherent limits (cracks)). Without pre-calcining the silica colloidal crystal template film to temperatures greater than the carbon processing temperature, poor healing of defects occurs in both (c) the open 3DOm film morphology and (d) the carbon-overlayer morphology.

An additional key to the successful replication and template sacrifice processes, described above in the context of thin films as opposed to bulk powders, is the management of localized stresses arising during processing. Namely, a critical challenge in translating hard-template-based powder replication to thin films relates to respective isotropic and anisotropic modes of stress relaxation during in situ high-temperature processing of carbon precursor-infiltrated amorphous silica templates. At temperatures employed for carbonization (i.e., $\geq 600^{o}C$) of polymerized carbon precursors, silanol groups within the amorphous silica template undergo

condensation chemistries.[43] The resulting densification of the silica template gives rise to localized stress concentration that can be released through isotropic structural rearrangement in the case of bulk powders.

Yet, in the case of thin films, intrinsic anisotropies tend to drive stress-relaxation via film cracking. Figure 2.2a shows SEM images of a template silica film following calcination to temperatures exceeding those employed for carbonization. The concomitant silica densification due to silanol condensation[43] results in silica nanoparticle shrinkage as manifested by the opening of grain boundaries and cracks/defects. As shown in Figure 2.2c (arrow), however, once formed, these defective features can ultimately be fully healed during subsequent carbon replication, wherein localized stress formation is limited during high-temperature carbonization due to pre-densification of the silica template.

If the precursor infiltration is instead carried out prior to preemptive densification of the silica structure, polymerization and carbonization of the precursor ultimately occurs simultaneously with the template densification, leading to the introduction of defects into the final carbon film. The striking contrast between structures in the carbon replica films derived from pre- and un-calcined silica templates is underscored by the SEM images in Figures 2.5c and 2.5d that show carbon replica films prepared prior to template densification. Whereas in the case of template pre-calcination, defects appear to be fully filled by the carbon replica material (Figure 2.2c), stretching of the precursor polymer or partially/fully carbonized replica material, apparently as a result of template stress relaxation, translates to porous defects or potential points of mechanical weakness in the final carbon replica structure.

2.3.5 Film robustness in the face of substrate non-idealities

While the syntheses described above were carried out on atomically smooth silicon wafers that are capable of withstanding high-temperature calcination conditions, exploitation of the derived films for applications as diverse as membrane separations (i.e., requiring support on

porous substrates) to high surface area electrodes ultimately requires expansion of substrate diversity. Conceptually, this can be accomplished by establishing techniques for post-synthesis transfer of the films among substrates of different composition, function, or character (e.g., roughness, porosity, etc.), a particularly useful strategy in cases where processing conditions employed for fabricating the porous carbon films (e.g., polymerization/carbonization, template etching) or specific substrate properties (e.g., hydrophobicity, porosity, etc.) preclude synthesis directly on the substrate. In cases where substrates are stable under such conditions, and can accommodate coating processes involved in porous film formation, insight into the robustness of the coating and replication process on various substrates becomes critical for establishing design strategies. Below, we demonstrate film transfer techniques specific to the carbon films studied herein and test the limits of the coating process in order to establish its robustness during direct deposition upon substrates bearing characteristic roughness several fold larger than the template particle size.

We first describe a stamp-transfer technique, adapted from recently reported polymer-mediated film transfer strategies,[44] enabling detachment and transfer of porous carbon films from silicon wafers to a range of other substrates. The transfer approach involves the deposition and solidification of a layer of PDMS precursor or PMMA-acetone solution on the top of prepared carbon films to bolster the stability of the ultra-thin films during transfer. Subsequent immersion of the polymer/carbon/silicon wafer composite into 30 wt% KOH solution results in delamination of the film/polymer composite from the silicon substrate and thereby production of a free-standing PDMS/carbon or PMMA/carbon composite. The composite thin film is then pressed onto a target substrate, and the PDMS or PMMA layer is removed by simple peeling or dissolved by acetone, respectively. Representative SEM images in Figure 2.6 show 3DOm carbon films after being transferred from a silicon wafer substrate to various other substrates including a glass cover-slip, flexible plastic PET sheet, porous stainless steel support, and conductive FTO-glass plate, the latter bearing characteristic surface roughness on the order of hundreds of nanometers.

The polymer-assisted transfer technique leverages apparent flexibility and robustness of the carbon replica film in order to avoid concomitant destruction of the meso/microstructure and film continuity. Both the micro and mesostructure of the films appear robust even to cyclic bending of the films supported on flexible PET substrates. Namely, the SEM image of the film morphology and mesostructure shown in Figure 2.6e was collected on a film that has undergone more than 20 cycles of bending, with no apparent structural degradation.

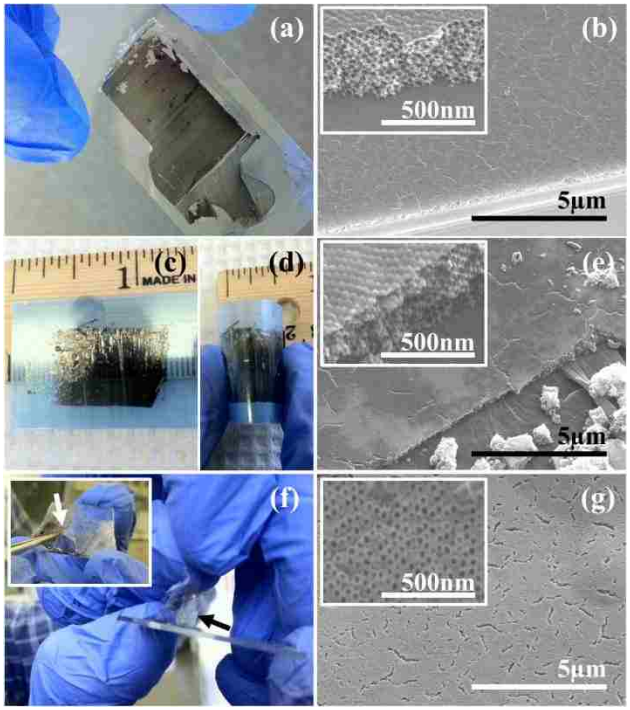

Figure 2.6: Representative images of the stamp-based film transfer from silicon wafer supports to (a,b) glass slides (inset in b shows persistent mesostructure after transfer), (c,d) flexible PET supports with film robustness during flexion underscored by (e) persistent meso- and micro-structure, and (f) FTO glass substrates with inherent surface roughness and (g) defects owing to poor adhesion resulting from surface roughness of the substrate.

Whereas high-fidelity film transfer to various smooth substrates is possible, attempts to transfer films to rough substrates, for example the polycrystalline surface of FTO glass, are challenged by poor adhesion. In such cases film defects (Figure 2.6g) result during peeling of the PDMS stamp. Moreover, poor conformal contact between the film and the underlying substrate, deriving possibly from lack of compliance of the 3DOm carbon film at the scale of the substrate

roughness, poses challenges in cases where applications require more intimate and uniform contact.

Improvement of the conformity of the porous carbon film to the detailed substrate topology of rough surfaces can be achieved if direct template deposition and carbon replication is possible. While translation of PVI and PIS replication processes is expected to be substrate-independent, both processes do rely, at least in part, on the ability to establish a highly ordered colloidal crystal template film of tunable thickness. Here, we employ FTO glass as a model rough surface. The scale of the surface roughness deriving from the polycrystalline morphology, is several fold larger than the diameter of the template particles. Figure 2.7a shows top and cross-sectional (inset) views of colloidal crystal coatings prepared as template films on FTO glass surfaces. Whereas colloidal crystallinity appears to propagate across the entire film thickness in coatings prepared on atomically smooth silicon wafers (Figure 2.1ab), coatings prepared on characteristically rough surfaces display an apparent transition from what appears to be random close packed (rcp) structures at the FTO surface (arrow in Figure 2.7a, inset) to longer-range colloidal crystallinity through the remainder of the film, thus underscoring the robustness and versatility of the coating process. The close-packed but disordered structure of the layer in immediate contact with the rough substrate is highlighted by carbon replicas of near-monolayer colloidal crystal films assembled directly on the rough support (Figure 2.7b). Despite the interfacial rcp geometry, a 3D network of multi-particle contacts still spans the full film thickness, ensuring complete accessibility of the replica film pore space and the underlying substrate.

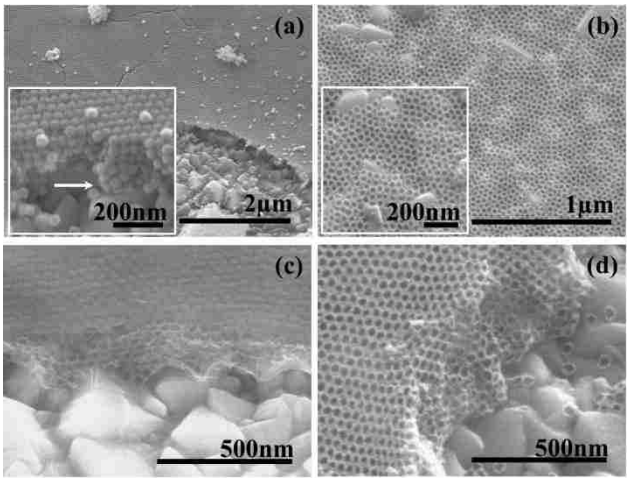

Figure 2.7: SEM images of (a) silica colloidal crystal template films deposited directly on the rough, polycrystalline surface of FTO glass. The inset shows the transition from apparent rcp-packing at the template-substrate interface, indicated by white arrow and confirmed by (b) carbon replication of a slightly disordered silica monolayer, to ordered close packed structure at the film surface. Carbon replication results in defect-free films with morphologies including (c) carbon-overlayers and (d) open 3DOm structures.

2.3.6 Tunable 3DOm films as low-cost electrodes

While the porous carbon films described above hold potential, for example, in membrane separations and sensing technologies, among others, here we have explored their suitability as low-cost alternatives to Pt-based counter-electrodes in dye-sensitized solar cell (DSSC) technologies.[45, 46] We have carried out systematic study of the sensitivity of overall cell efficiency to tunable film properties, film transfer strategies, and carbon powder deposition. Our primary aim is to gain insight into sensitivities to factors such as pore accessibility, surface area, interfacial phenomena, and carbonization as well as to assess the viability of the 3DOm carbon films as electrode materials.

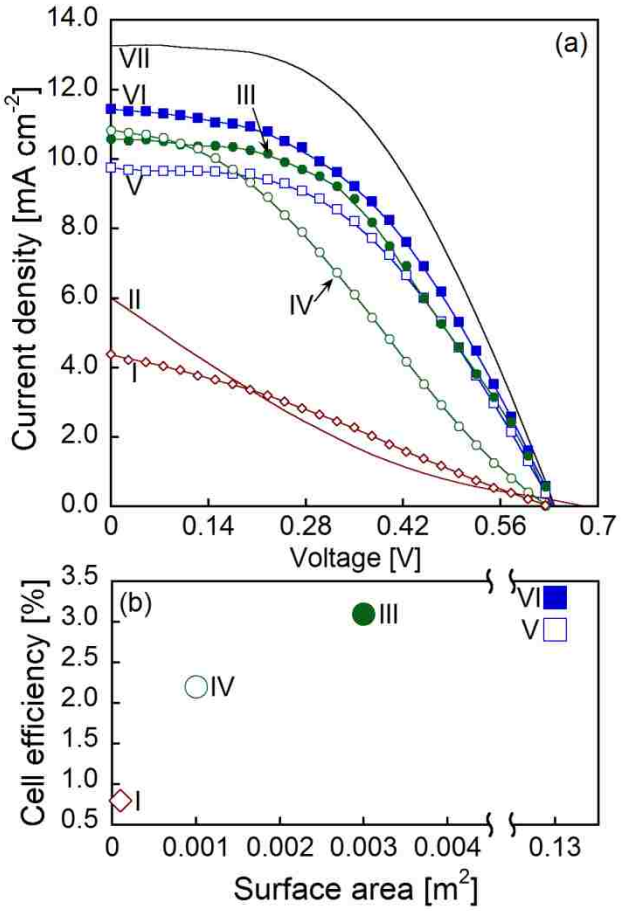

Figure 2.8: (a) Current-voltage performance and (b) sensitivity of select overall cell efficiency, η, to total electrode surface area for lab-scale dye-sensitized solar cells (DSSC) packaged with low-cost carbon counter-electrodes of various morphologies deposited on FTO glass relative to a costly conventional platinum electrode. Counter-electrode morphologies (and corresponding cell efficiencies, η) include ca. 500 nm thick 3DOm carbon films (I) stamp-transferred with open pores (η=0.7%), (II) directly deposited with carbon over-layer (0.8%), and (III) directly-deposited with open pores (3.1%); (IV) thinner 150 nm directly deposited open 3DOm films (2.2%), as well as dispersions of bulk 3DOm carbon powders that have been carbonized at (V) 600°C (2.9%) and (VI) 900°C (3.3%). Comparisons are drawn against the same cell packaging with a (VII) Pt electrode (4.1%).

Due to the temperature sensitivity of the FTO glass substrate that limits processing to 600°C or less, we prepared open 3DOm carbon films on silicon wafers with full carbonization at 900°C, and used stamp-mediated approaches to transfer them to the FTO glass surface. Corresponding I-V measurements show a correspondingly low overall cell efficiency of 0.7%. The near linear form of the I-V curve is indicative of large cell resistances.[47] We attribute such resistances to the aforementioned challenges associated with the lack of conformal contact between transferred

films and the rough FTO surface. Fabrication of templated films directly upon the FTO glass surface is also possible, but carbonization is limited to 600^{o}C due to substrate temperature sensitivity. 3DOm films of the same thickness as the stamp-transferred ones (ca. 500 nm), and thus bearing comparable surface area (ca. 3x10^{-3} m^{2} over the 1 cm^{2} area of the packaged DSSC), were fabricated directly on the FTO surface. Despite a lower degree of carbonization relative to the stamp-transferred films, dramatic improvements in cell efficiency of more than 340% are realized. Moreover, the absolute cell efficiency of 3.1% approaches the 4.1% efficiency realized with the conventional Pt electrodes, but for two orders of magnitude lower materials cost (see SI, Table S2.2).

Under the carbonization temperature limits dictated by the substrate, the overall cell efficiency seems to be sensitive to the total available surface area provided by the 3DOm carbon film (Figure 2.8b). Namely, thinner 3DOm carbon films (ca. 150 nm thick) fabricated directly on the FTO surface yield a cell efficiency of 2.2%, with further dramatic reduction in efficiency associated with low-surface area carbon electrode morphologies wherein the 3DOm structure is covered by a non-porous carbon over-layer. In fact, with fabrication of such carbon films directly on the FTO glass, overall cell efficiency drops to 0.8%, concomitant with the low efficiency measured for stamp-transferred films. Again, the low efficiency and shape of the I-V curves point to the high cell resistance, attributable to the inaccessibility of the 3DOm carbon structure to the DSSC electrolyte because of the capping carbon layer.

These data underscore how the large surface area offered by the 3DOm carbon films enable realization of overall DSSC efficiencies approaching those achieved with conventional, high-cost Pt-based electrodes. This is achieved in spite of the necessary reduction in carbonization temperature dictated by the sensitivity of the FTO substrate. Additionally, intimate contact between the carbons and the conductive layer of the FTO glass appears critical for cell performance. Distinct cost, fabrication, and stability benefits associated with film formation directly on the FTO surface exist as underscored by comparisons with simple dispersion of

corresponding 3DOm carbon powders as electrode materials in lieu of films. Namely, we find that dispersion of 3DOm powders carbonized at 900°C and 600°C on the FTO substrate results in overall cell efficiencies (3.3% and 2.9%, respectively) that are comparable to or less than efficiencies achieved with the thickest 3DOm films studied here despite deposition of more than ten times the mass, and thus the surface area, of the corresponding films. Moreover, the aggregation and general instability of the 3DOm carbon powders (i.e., release from the FTO surface into the electrolyte) underscores the distinct benefits of the 3DOm films as low-cost, scalable, and stable alternatives to Pt-based electrodes.

2.4 Conclusions

We have developed a facile and scalable strategy for realizing defect-free, hard-templated, three-dimensionally ordered meso- (3DOm) and 3DOm-supported carbon thin films of tunable thickness. To do so, we have exploited surfactant-free convective assembly of silica nanoparticles into tunable colloidal crystal thin films, a process that is robust to substrate roughness exceeding by several fold the size of the deposited nanoparticles, as a means for successfully bridging conventional powder processing and hard-templating of porous carbon films. Carbon precursor vapor infiltration (PVI) or immersion-spin-off (PIS) methods, followed by in situ polymerization, carbonization, and selective template sacrifice leads to high-fidelity replication of the colloidal crystal thin films, with film thickness and morphology tunable by template film thickness and the degree to which the template is filled. Ultimately, the strategy described herein provides a means for overcoming some of the commonly perceived challenges with hard templating of thin carbon films, including circumventing costly surfactant sacrifice from conventional mesoporous silica templates, realizing ordered and continuous mesostructure through fast and facile carbon replication, and achieving film continuity and substrate adhesion by replica uniformity. In addition, the hard-templating strategy demonstrated here addresses some key challenges associated with soft-templating approaches, including realization of

accessible, ordered, size-tunable, and film-spanning mesoporosity, resistance to uniaxial pore shrinkage, and accommodation of a wide range of carbon precursors (e.g., furfural/oxalic acid, phenol-formaldehyde, resorcinol-formaldehyde, sucrose). By exploiting the intrinsic flexibility of the thin replica films, ability to transfer them among substrates, and robustness of the replica film process to substrate surface roughness, we have demonstrated synthesis-structure-function relations for these films, underscoring their promise as low-cost electrodes for dye-sensitized solar cells.

2.5 Supporting Information

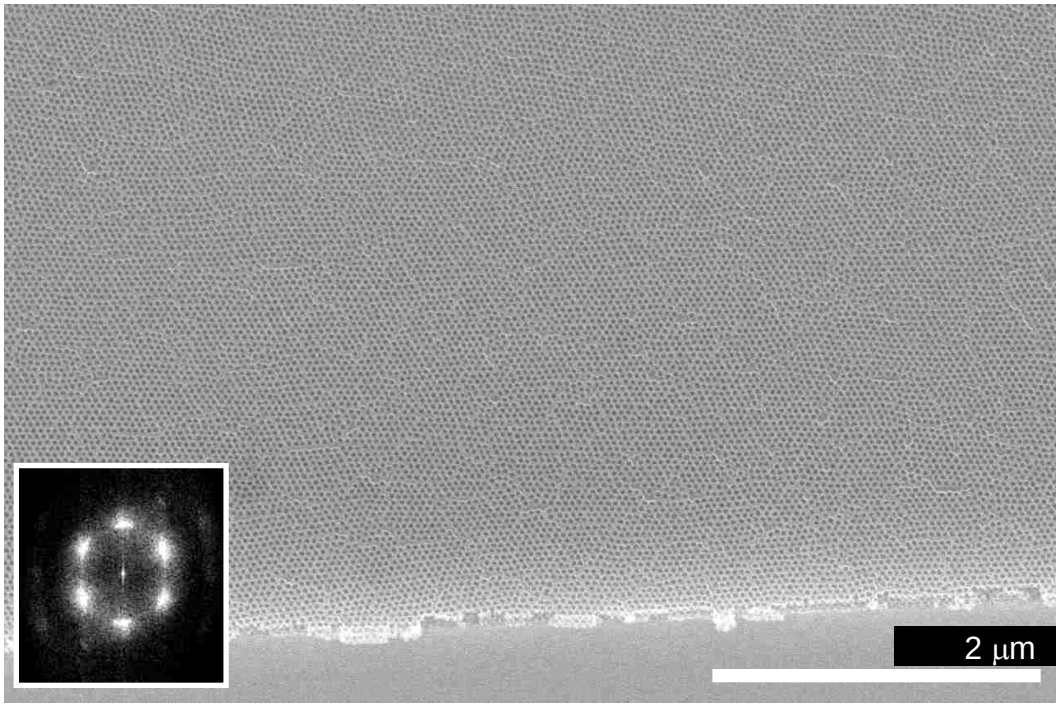

SI Figure 2.1: Low-magnification SEM image of open 3DOm replica film underscoring the long-range order of the mesopores and defect-free structure of the film itself, the latter owing to the healing of the cracks and grain boundaries in the template.

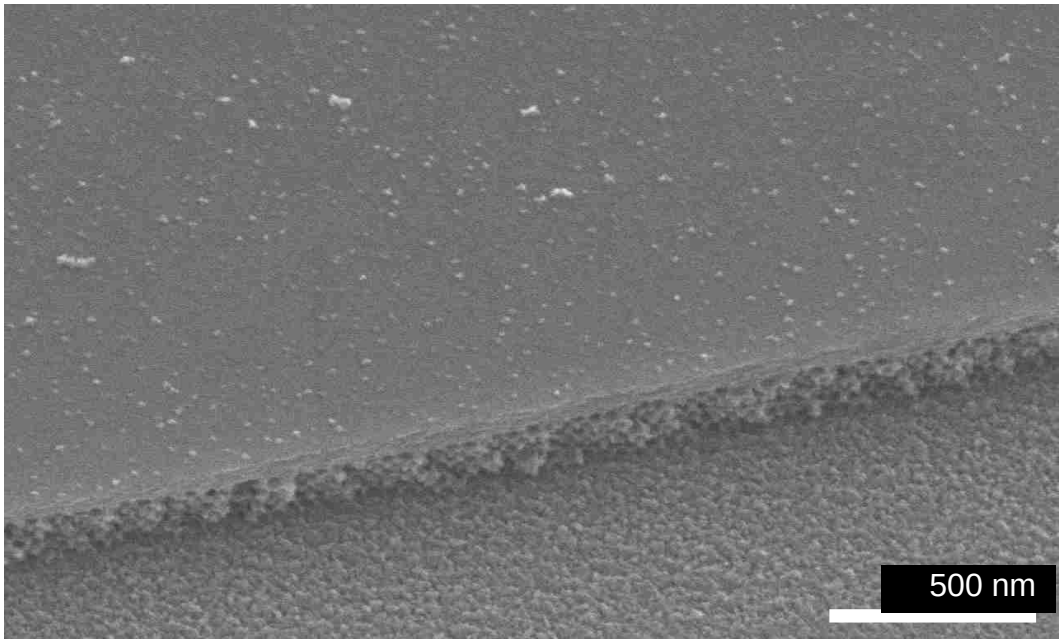

SI Figure 2.2: Low-magnification SEM image of a representative carbon replica film bearing a 3DOm-supported over-layer morphology underscoring the defect-free structure. The film was prepared by PVI processing, with the thickness of the over-layer tuned by PVI duration and the thickness of the 3DOm layer controlled by the thickness of the colloidal crystal film.

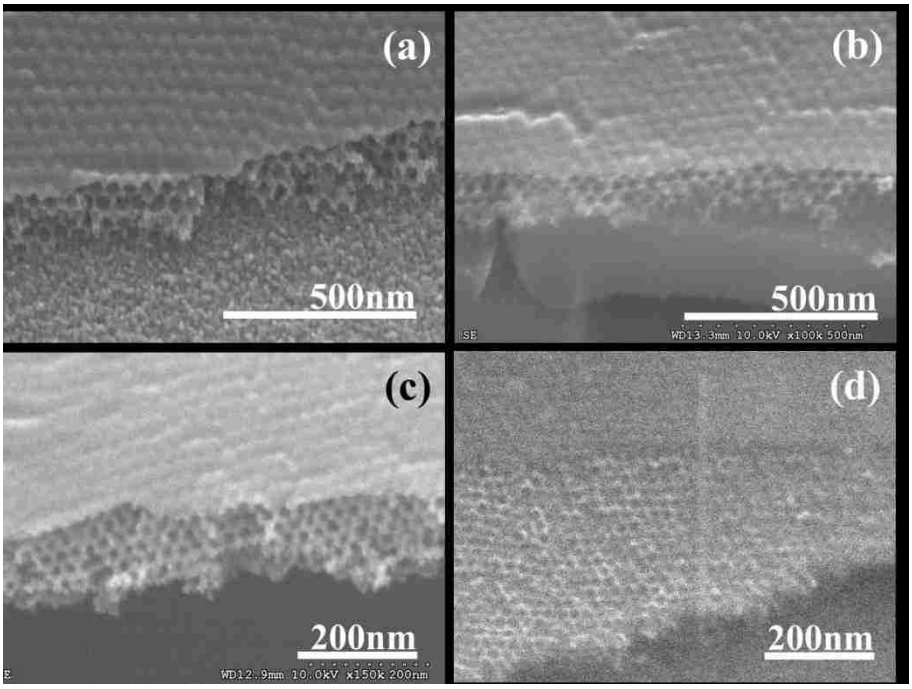

SI Figure 2.3: Representative SEM images of 3DOm carbon replicas of colloidal crystal template films comprised of (a) ca. 50, (b) ca. 40, (c) ca. 30, and (d) ca. 20 nm silica particles.

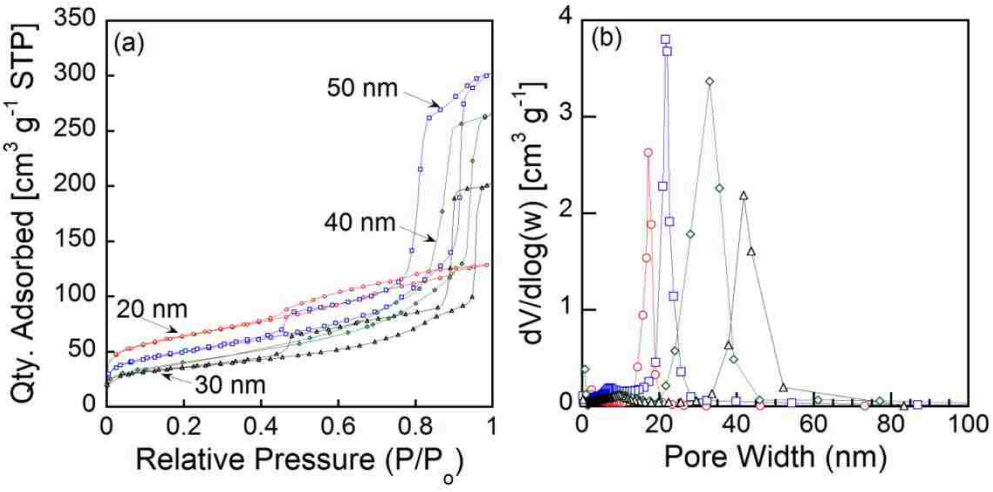

SI Figure 2.4: (a) Nitrogen adsorption isotherms and (b) BJH pore size distributions extracted from the adsorption branches collected on representative carbon replica powders templated on silica colloidal crystals of prescribed size, with selective template etching carried out with HF at room temperature. The two-step desorption branches, and cavitation of the condensed nitrogen leading to closure of the hysteresis loops for all replica materials at a consistent relative pressure, P/P_o~0.4 due to the tensile effect is indicative of pore blocking effects.[48, 49]

SI Table 2.1: Nitrogen adsorption data of silica/polymer/carbon samples

		20nm		30nm		40nm		50nm	
		Surface Area[a,b] [$m^2 g^{-1}$]	**Pore Volume [$cm^3 g^{-1}$]**	**Surface Area [$m^2 g^{-1}$]**	**Pore Volume [$cm^3 g^{-1}$]**	**Surface Area [$m^2 g^{-1}$]**	**Pore Volume [$cm^3 g^{-1}$]**	**Surface Area [$m^2 g^{-1}$]**	**Pore Volume [$cm^3 g^{-1}$]**
Silica	*Total*	170	0.17	140	0.25	122	0.23	107	0.23
	Mesopore	168	0.17	134	0.24	114	0.21	98	0.21
	Micropore	2.3	~0.005	6	~0.01	8	~0.02	8	~0.02
Silica + PFA	*Total*	~0.2	0.0007	6	0.01	~0.1	0.0003	~0.7	0.002
	Mesopore	~0	~0	5	~0	~0	~0	~0	~0
	Micropore	~0	~0	1	~0	~0	~0	~0	~0
Carbon by	*Total*	1694	3.64	1489	4.28	1410	4.65	1315	3.30
	Mesopore	543	2.35	464	2.34	378	2.14	300	2.01
	Micropore	1150	1.29	1024	1.94	1032	2.50	1015	1.28
Carbon by	*Total*	228	0.20	174	0.47	143	0.41	128	0.31
	Mesopore	213	0.17	111	0.35	109	0.32	104	0.27
	Micropore	15	0.03	62	0.12	34	0.09	24	0.05

(a) The total surface area is calculated based on Brunnauer-Emmet-Teller (BET) method.

(b) The mesopore surface area is calculated by the t-plot method, with the micropore surface area computed as the difference between total and mesopore surface area.

(c) KOH etching carried out at 180°C, leading to micropore activation manifested in textural measures.

(d) HF etching carried out at room temperature.

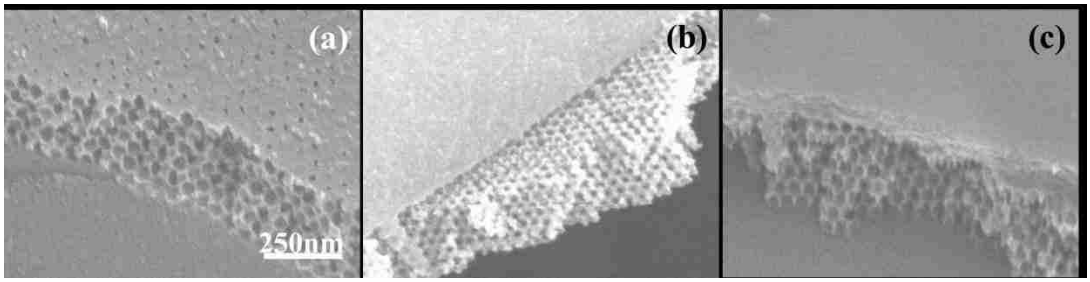

SI Figure 2.5: SEM images of carbon films formed by precursor immersion and spin-off (PIS) approach using carbon sources: (a) resorcinol-formaldehyde, (b) sucrose and (c) FA/OA.

SI Table 2.2: Comparison of specific material cost and working efficiency of Pt- and 3DOm carbon-based DSSC counter-electrodes

	Electrode material costs	
Material	**Platinum electrode**	**3DOm carbon electrode**
Solaronix Platisol T/S [$5/g]	$0.5/in^2 [0.1g/inch]	--
Silica nanoparticle sol [$0.22/g]	--	$0.0008/in^2 [50µL, 4%vol]
FA/OA solution (Sigma) [$0.07/g]	--	$0.004/in^2 [25µL]
KOH (Sigma) [$0.058/g]	--	$0.0004/in^2 [7x10^{-3} g]
Total	**$0.5/in^2**	**$0.005/in^2**

2.6 Reference

1. Liang, C. D.; Li, Z. J.; Dai, S. Mesoporous carbon materials: Synthesis and modification. *Angewandte Chemie-International Edition* **2008,** *47* (20), 3696-3717.

2. Ma, T. Y.; Liu, L.; Yuan, Z. Y. Direct synthesis of ordered mesoporous carbons. *Chemical Society Reviews* **2013,** *42* (9), 3977-4003.

3. Xia, Y.; Yang, Z.; Mokaya, R. Templated nanoscale porous carbons. *Nanoscale* **2010,** *2*, 639-659.

4. Zhao, X. S.; Su, F.; Yan, Q.; Guo, W.; Bao, X. Y.; Lv, L.; Zhou, Z. Templating methods for prepation of porous structures. *J. Mater. Chem.* **2006,** *16*, 637-648.

5. Ryoo, R.; Joo, S. H.; Jun, S. Synthesis of highly ordered carbon molecular sieves via template-mediated structural transformation. *Journal of Physical Chemistry B* **1999,** *103* (37), 7743-7746.

6. Lee, J.; Yoo, S.; Hyeon, T.; Oh, S. M.; Kim, K. B. Synthesis of a new mesoporous carbon and its application to electrochemical double-layer capacitors. *Chem. Commun.* **1999,** (21), 2177-2178.

7. Liang, C. D.; Dai, S. Synthesis of mesoporous carbon materials via enhanced hydrogen-bonding interaction. *Journal of the American Chemical Society* **2006,** *128* (16), 5316-5317.

8. Liang, C. D.; Hong, K. L.; Guiochon, G. A.; Mays, J. W.; Dai, S. Synthesis of a large-scale highly ordered porous carbon film by self-assembly of block copolymers. *Angewandte Chemie-International Edition* **2004,** *43* (43), 5785-5789.

9. Jin, J.; Nishiyama, N.; Egashira, Y.; Ueyama, K. Vapor phase synthesis of ultrathin carbon films with a mesoporous monolayer by a soft-templating method. *Chem. Commun.* **2009**, 1371-1373.

10. Pang, J.; Li, Z.; Wang, D.; Wu, Z.; Joh, V. T.; Yang, Z.; Lu, Y. Silica-templated continuous mesoporous carbon films by a spin-coating technique. *Adv. Mater.* **2004,** *16* (11), 884-886.

11. Reculusa, S.; Agricole, B.; Derre, A.; Couzi, M.; Sellier, E.; Ravaine, S.; Delhaes, P. Carbon membranes of controlled thickness from colloidal crystals. *Advanced Materials* **2006,** *18* (13), 1705-1708.

12. Song, L.; Feng, D.; Campbell, C. G.; Gu, D.; Forster, A. M.; Yager, K. G.; Fredin, N.; Lee, H.-J.; Jones, R. L.; Zhao, D.; Vogt, B. D. Robust conductive mesoporous carbon–silica composite films with highly ordered and oriented orthorhombic structures from triblock-copolymer template co-assembly. *J. Mater. Chem.* **2010,** *20*, 1691-1701.

13. Tanaka, S.; Katayama, Y.; Tate, M. P.; Hillhouse, H. W.; Miyake, Y. Fabrication of continuous mesoporous carbon films with face-centered orthorhombic symmetry through a soft templating pathway. *J. Mater. Chem.* **2007,** *17*, 3639-3645.

14. Xue, J.; Henry, C.; Lee, J.; Vogt, B. D. Large area, flexible ordered mesoporous carbon films from soft templating on polymer substrates. *RSC. Adv.* **2014,** *4*, 3675-3683.

15. Tao, Y.; Endo, M.; Inagaki, M.; Kaneko, K. Recent progress in the synthesis and applications of nanoporous carbon films. *J. Mater. Chem.* **2011,** *21*, 313-323.

16. Huang, E.; Rockford, L.; Russell, T. P.; Hawker, C. J. Nanodomain control in copolymer thin films. *Nature* **1998,** *395*, 757-758.

17. Kim, S. H.; Misner, M. J.; Xu, T.; Kimura, M.; Russell, T. P. Highly oriented and ordered arrays from block copolymers via solvent evaporation. *Adv. Mater.* **2004,** *16* (3), 226-231.

18. Villar, M. A.; Rueda, D. R.; Ania, F.; Thomas, E. L. Study of oriented block copolymers films obtained by roll-casting. *Polymer* **2002,** *43*, 5139-5145.

19. Kataoka, S.; Yamamoto, T.; Inagi, Y.; Endo, A.; Nakaiwa, M.; Ohmori, T. Synthesis of ordered mesoporous carbon thin films at various temperatures in vapor infiltration method. *Carbon* **2008,** *46*, 1358-1367.

20. Song, L.; Feng, D.; Fredin, N. J.; Yager, K. G.; Jones, R. L.; Wu, Q.; Zhao, D.; Vogt, B. D. Challenges in fabrication of mesoporous carbon films with ordered cylindrical pores via phenolic oligomer self-assembly with triblock copolymers. *ACS Nano* **2010,** *4* (1), 189-198.

21. Stein, A.; Li, F.; Denny, N. R. Morphological control in colloidal crystal templating of inverse opals, hierarchical structures, and shaped particles. *Chemistry of Materials* **2008,** *20* (3), 649-666.

22. Jun, S.; Joo, S. H.; Ryoo, R.; Kruk, M.; Jaroniec, M.; Liu, Z.; Ohsuna, T.; Terasaki, O. Synthesis of new, nanoporous carbon with hexagonally ordered mesostructure. *Journal of the American Chemical Society* **2000,** *122* (43), 10712-10713.

23. Gierszal, K. P.; Jaroniec, M. Carbons with extremely large volume of uniform mesopores synthesized by carbonization of phenolic resin film formed on colloidal silica template. *Journal of the American Chemical Society* **2006,** *128* (31), 10026-10027.

24. Han, S.; Hyeon, T. Simple silica-particle template synthesis of mesoporous carbons. *Chem. Commun.* **1999**, 1955-1956.

25. Han, S.; Lee, K. T.; Oh, S. M.; Hyeon, T. The effect of silica template structure on the pore strucure of mesoporous carbons. *Carbon* **2003,** *41*, 1049-1056.

26. Yoon, S. B.; Chai, G. S.; Kang, S. K.; Yu, J.-S.; Gierszal, K. P.; Jaroniec, M. Graphitized Pitch-Based Carbons with Ordered Nanopores Synthesized by Using Colloidal Crystals as Templates. *J. Amer. Chem. Soc.* **2005,** *127* (12), 4188-4189.

27. Li, Z.; Jaroniec, M. Colloidal Imprinting: A Novel Approch to the Synthesis of Mesoporous Carbons. *J. Amer. Chem. Soc.* **2001,** *123* (37), 9208-9209.

28. Wei, T.-C.; Hillhouse, H. W. Mass transport and electrod accessibility through periodic self-assembled nanoporous silica thin films. *Langmuir* **2007,** *23*, 5689-5699.

29. Snyder, M. A.; Lee, J. A.; Davis, T. M.; Scriven, L. E.; Tsapatsis, M. Silica nanoparticle crystals and ordered coatings using lys-sil and a novel coating device. *Langmuir* **2007,** *23* (20), 9924-9928.

30. Dimitrov, A. S.; Nagayama, K. Continuous convective assembling of fine particles into two-dimensional arrays on solid surfaces. *Langmuir* **1996,** *12* (5), 1303-1311.

31. Prevo, B. G.; Velev, O. D. Controlled, rapid deposition of structured coatings from micro- and nanoparticle suspensions. *Langmuir* **2004,** *20*, 2099-2107.

32. Chen, K.; Stoianov, S. V.; Bangerter, J.; Robinson, H. D. Restricted meniscus convective self-assembly. *Journal of Colloid and Interface Science* **2010,** *344* (2), 315-320.

33. Kumnorkaew, P.; Ee, Y. K.; Tansu, N.; Gilchrist, J. F. Investigation of the Deposition of Microsphere Monolayers for Fabrication of Microlens Arrays. *Langmuir* **2008,** *24* (21), 12150-12157.

34. Lu, Y. F.; Ganguli, R.; Drewien, C. A.; Anderson, M. T.; Brinker, C. J.; Gong, W. L.; Guo, Y. X.; Soyez, H.; Dunn, B.; Huang, M. H.; Zink, J. I. Continuous formation of supported cubic and hexagonal mesoporous films by sol gel dip-coating. *Nature* **1997,** *389* (6649), 364-368.

35. Fan, W.; Snyder, M. A.; Kumar, S.; Lee, P. S.; Yoo, W. C.; McCormick, A. V.; Penn, R. L.; Stein, A.; Tsapatsis, M. Hierarchical nanofabrication of microporous crystals with ordered mesoporosity. *Nature Materials* **2008,** *7* (12), 984-991.

36. Davis, T. M.; Snyder, M. A.; Krohn, J. E.; Tsapatsis, M. Nanoparticles in lysine-silica sols. *Chemistry of Materials* **2006,** *18* (25), 5814-5816.

37. Yokoi, T.; Sakamoto, Y.; Terasaki, O.; Kubota, Y.; Okubo, T.; Tatsumi, T. Periodic arrangement of silica nanospheres assisted by amino acids. *Journal of the American Chemical Society* **2006,** *128* (42), 13664-13665.

38. Jiang, P.; Hwang, K. S.; Mittleman, D. M.; Bertone, J. F.; Colvin, V. L. Template-directed preparation of macroporous polymers with oriented and crystalline arrays of voids. *Journal of the American Chemical Society* **1999,** *121* (50), 11630-11637.

39. Miguez, H.; Meseguer, F.; Lopez, C.; Lopez-Tejeira, F.; Sanchez-Dehesa, J. Synthesis and photonic bandgap characterization of polymer inverse opals. *Advanced Materials* **2001,** *13* (6), 393-396.

40. Cychosz, K. A.; Guo, X.; Fan, W.; Cimino, R.; Gor, G. Y.; Tsapatsis, M.; Neimark, A. V.; Thommes, M. Characterization of the Pore Structure of Three-Dimensionally Ordered Mesoporous Carbons Using High Resolution Gas Sorption. *Langmuir* **2012,** *28*, 12647-12654.

41. Choi, M.; Ryoo, R. Mesoporous carbons with KOH activated framework and their hydrogen adsorption. *Journal of Materials Chemistry* **2007,** *17* (39), 4204-4209.

42. Shiflett, M. B.; Foley, H. C. Ultrasonic deposition of high-selectivity nanoporous carbon membranes. *Science* **1999,** *285* (5435), 1902-1905.

43. Van Le, T.; Ross, E. E.; Velarde, T. R. C.; Legg, M. A.; Wirth, M. J. Sintered silica colloidal crystals with fully hydroxylated surfaces. *Langmuir* **2007,** *23* (16), 8554-8559.

44. Feng, D.; Lv, Y. Y.; Wu, Z. X.; Dou, Y. Q.; Han, L.; Sun, Z. K.; Xia, Y. Y.; Zheng, G. F.; Zhao, D. Y. Free-Standing Mesoporous Carbon Thin Films with Highly Ordered Pore Architectures for Nanodevices. *Journal of the American Chemical Society* **2011,** *133* (38), 15148-15156.

45. Huang, Y. Y.; Terentjev, E. M. Transparent Electrode with a Nanostructured Coating. *Acs Nano* **2011,** *5* (3), 2082-2089.

46. Lee, K. S.; Lee, W. J.; Park, N. G.; Kim, S. O.; Park, J. H. Transferred vertically aligned N-doped carbon nanotube arrays: use in dye-sensitized solar cells as counter electrodes. *Chemical Communications* **2011,** *47* (14), 4264-4266.

47. Hagfeldt, A.; Boschloo, G.; Sun, L. C.; Kloo, L.; Pettersson, H. Dye-Sensitized Solar Cells. *Chemical Reviews* **2010,** *110* (11), 6595-6663.

48. Van Der Voort, P.; Ravikovitch, P. I.; De Jong, K. P.; Neimark, A. V.; Janssen, A. H.; Benjelloun, M.; Van Bavel, E.; Cool, P.; Weckhuysen, B. M.; Vansant, E. F. Plugged hexagonal templated silica: a unique micro- and mesoporous composite material with internal silica nanocapsules. *Chemical Communications* **2002,** (9), 1010-1011.

49. Thommes, M. Physical Adsorption Characterization of Nanoporous Materials. *Chemie Ingenieur Technik* **2010,** *82* (7), 1059-1073.

Chapter 3: Nanocasting of bicontinuous three-dimensionally ordered mesoporous carbon films by template-replica co-assembly

3.1 Introduction

Control of the size, order, orientation, and specific topology of mesopores within carbon thin films has been the focus of extensive study, owing to their potential for applications as diverse as electrodes, catalyst supports, membranes, and adsorbents, among others.[1, 2, 3, 4, 5] So-called 'soft-templating' strategies[1, 6, 7, 8, 9] that exploit the self-assembly phase behavior of copolymer surfactants as templates and polymerizable carbon precursors have been demonstrated to enable realization of ordered mesoporous carbon films.[6, 10, 11, 12] The hallmark of 'soft-templating' is its intrinsic scalability owing to its reliance on 'one-pot' solution phase thermodynamics for the realization of carbon films of a range of pore topologies. Yet, this approach faces drawbacks, including the cost of sacrificial surfactants or polymer blocks, pore shrinkage during template removal[9, 10, 11, 13], and challenges associated with pore orientation[12, 14, 15] and wormy pore topologies[1, 7] that can lead to limits on mass transport.

Alternative hard-templating or 'nanocasting' methods,[16, 17] wherein sacrificial solid materials (commonly silica) are employed as pore-forming agents, hold potential to overcome some of these limitations.[18, 19, 20] Namely hard templates often enjoy structural robustness under polymerization and carbonization conditions, helping to bolster mesopores against uniaxial pore shrinkage during template sacrifice. These templates can also be less sensitive to interfacial effects such that replica film-spanning pore orientation may be more easily realized.[20] Despite these potential benefits, conventional 'hard-templating' is commonly discounted on the basis of its intrinsic multi-step character.[2, 9] Namely it requires pre-fabrication of template films prior to subsequent infiltration, polymerization, and carbonization of molecular carbon precursors and

template sacrifice. Complicating the process further is its common reliance on ordered mesoporous silicas (OMSs) as templates,[21, 22] for which porosity is derived from self-assembling lyotropic phases of cationic, anionic, or nonionic surfactants, thus requiring template removal prior to carbon replication. Beyond such multi-step drawbacks of the hard-templating approach, efforts to nanocast ordered mesoporous carbon films have also generally been plagued by poor scalability of the template films, the need for costly and repetitive precursor infiltration[19, 20], film discontinuity[18], and poor substrate adhesion.

As discussion in Chapter 2, we have recently addressed several of the drawbacks associated with both hard- and soft-templating through demonstration of a facile method for scalable synthesis of three-dimensionally ordered mesoporous (3DOm) carbon films of tunable pore size, morphology (e.g., 3DOm, 3DOm-supported thin films), and film thicknesses by a facile hard-templating approach.[23] To achieve this, we exploited the scalable and facile convective deposition of silica nanoparticle crystalline films as templates,[24] wherein porosity for carbon infiltration derives simply from the interstitial spaces between assembled nanoparticles and, thus, avoids the need for pore-forming agents and their ultimate removal prior to replication. While this simplifies the nanocasting of mesoporous thin films, a gap still remains relative to soft-templating approaches, embodied by the persistent need for the pre-formation of the hard sacrificial template.

In the spirit of the 'one-pot' soft templating approach to mesoporous thin films, identification of specific design strategies and template systems enabling the simultaneous assembly of the thin film template with the molecular replica precursors could help to bridge the materials gap between hard and soft templating of mesoporous carbon films. Recent work by Aizenberg and co-workers[25, 26, 27] and others[28], albeit at larger scales and for different replication medium (i.e., silica), has provided insight into a potential strategy for overcoming this materials gap. Namely, they have shown that simultaneous evaporation-induced self-assembly of polymer colloids (i.e., polystyrene, poly(methyl methacrylate)) from a range of metal (M) alkoxide sol-gel precursor solutions (M: Si, Ti, Ge) can lead to large area (cm^2) defect(crack)-free composite films, wherein

hydrolyzed alkoxides result in gels spanning the colloidal crystalline interstices. They also identify metal alkoxide concentration limits marking transitions from ordered, open macroporous replica films and ones bearing a metal oxide over-layer.

Here, by analogy, we have focused efforts on establishing a new paradigm for co-assembly of carbon molecular replica precursors with mesopore-forming moieties as a facile approach toward realizing 'one-pot' nanocasting of 3D ordered mesoporous (3DOm) thin films. We demonstrate the viability of this approach, taking advantage of the monodispersity and stability of Lys-Sil nanoparticle sols[29, 30] and their facile convective co-assembly with molecular carbon precursors into carbon-infiltrated ordered colloidal crystals. We show that a benefit of this approach is the realization of largely defect-free mesoporous films analogous to findings by Aizenberg and co-workers[25] for template-replica systems of different characteristic length scales and compositions. Moreover, we show that unique, three-dimensionally ordered bi-continuous mesoporous carbon (b3DOm C) topologies result from the convective co-deposition process.

Beyond demonstrating the novel strategy for 'one-pot' hard templating of mesoporous carbon thin films, we describe systematic studies aimed at mechanistic elucidation of the 'one-pot' process that gives rise, specifically, to the b3DOm C pore topology. We establish a pseudo-phase diagram wherein molecular replica precursors are found to mediate particle assembly, and, thus the parametric space over which the b3DOm C films can be realized. We ultimately uncover key insight into how the glucose-silica association modulates lattice spacing, which appears to eventually trigger a distinct transition between highly ordered b3DOm C films and disordered porous film morphologies. Finally, we take advantage of the facile nature of this b3DOm C film fabrication and its robustness during deposition on even rough substrates to demonstrate how the large pore volume can be exploited for high-performance electrode applications.

3.2 Materials and Methods

Materials. The following reagents were used without further purification: tetraethyl orthosilicate (TEOS, 98%), sulfuric acid (H_2SO_4, 98%), L-lysine (98%), glucose and saccharin were obtained from Sigma-Aldrich and Acros Organics. Hydrogen peroxide (H_2O_2, 30%) was obtained from Fisher Scientific. Hydrofluoric acid (HF, 49%) was obtained from Alfa Aesar. Potassium hydroxide (ACS grade) and hydrochloric acid (37% wt.) were obtained from BDH. Silicon wafers were purchased from Silicon Quest Int. and FTO-glass (fluorine doped tin oxide glass, DEC-7) plates were obtained from Pilkington North America. Solaronix Ti-Nanoxide, Platisol T/SP, Solaronix Iodolyte AN-50 electrolyte, and Solaronix Ruthenizer 535-bisTBA (Solaronix N719, prepared as 0.3 mM solution in tert-butanol (Sigma Aldrich, 99.7%) were used as received without further purification. Millipore water with resistivity 18MΩ/cm was used for all reactions and purifications.

Silica nanoparticle synthesis. Monodisperse (ca. <5% polydispersity) silica nanoparticles were prepared following previous reports on direct and seeded amino acid-facilitated synthesis of silica nanoparticles, termed 'Lys-Sil' nanoparticles[29, 30, 31, 32]. Typically, L-lysine was dissolved in water under vigorous stirring for 0.5 hr within an oil bath at 90°C. TEOS was subsequently hydrolyzed in the aqueous L-Lysine solutions at 90°C under vigorous stirring for at least 12 hrs. Sols of silica seed nanoparticles of a nominal diameter of ca. 16 nm were synthesized directly, with a final molar composition of the nanoparticle sol of x SiO_2/ y Lysine/ 9500 water/ 4x ethanol, where x=60, y=1.23, and the only ethanol was liberated upon hydrolysis of TEOS. Seeded growth of larger particles was carried out by addition of TEOS to the as-made seed Lys-Sil solution in multiple (2-4) aliquots, with intermediate hydrolysis at 90°C for at least 12 hrs under vigorous stirring, until a sufficient molar composition of TEOS (SiO_2, x) was reached to yield silica nanoparticle sols of 20 nm (x=100), 30 nm (x=210), 40 nm (x=690), and 50 nm (x=1120) nominal nanoparticle sizes. Dialysis of the resulting silica suspensions was carried out against water for 3 days with mild stirring using Spectra/Por® dialysis bags (Spectrum Labs, MW cutoff

of 3500). Water was exchanged every 8 hrs. The resulting silica solids content of the dialyzed solution was measured by mass difference between a 1 mL aliquot of the dialyzed solution before and after solvent evaporation and drying in an oven at 70^{o}C, assuming a silica density of 1.8 g/cm^{3}.[33]

Template-molecular carbon precursor solutions Glucose was used as the molecular carbon source in this study. Glucose solutions in dilute sulfuric acid, a carbonization catalyst, were typically prepared by dissolving 2.50 g of glucose into a stock aqueous sulfuric acid solution composed of 10 µL 98 wt% H_2SO_4 and 10 g of water. Preparation of silica nanoparticle-glucose solutions for convective co-deposition was accomplished by adding prescribed amounts of the glucose solution into already-dialyzed Lys-Sil nanoparticle suspensions. For example, 1mL of a dialyzed 50nm silica suspension, with a measured solids content of 3.97% v/v, was mixed with 0.2 mL of the glucose solution to achieve a precursor suspension for convective deposition with a glucose concentration of 0.035g/mL. Prior to convective co-deposition, solutions were stirred vigorously for at least 3 hours to equilibrate the silica nanoparticles with the dissolved glucose.

Convective co-deposition of silica nanoparticles and molecular carbon precursor Silicon wafers were used as the primary substrates for preparation of co-deposited coatings in this study, with use of FTO glass for the final test bed application of the deposited carbon films as counter-electrodes for dye-sensitized solar cells. To remove organic impurities and obtain super-hydrophilic surfaces, silicon wafers were immersed in piranha solution (98% wt. sulfuric acid, 30% wt. hydrogen peroxide combined in volume ratio 3:1) for at least 30min, rinsed subsequently in water until no residual acid remained, and then stored in water until their use. FTO-glass plates were rinsed with ethanol, immersed in a 0.1 M HCl ethanol solution for 20min and sonicated therein for 15 min, with ethanol used to finally rinse the substrates. All substrates were dried with a jet of ultra-pure dried nitrogen before convective deposition was carried out. The experimental convective deposition setup, described previously in Refs. [34, 35], employs a glass microscope slide as a coating blade, fixed approximately 0.5 mm above and at an angle of 45^{o} to an underlying

substrate. The bottom edge of the glass slide/blade is made hydrophobic by attaching a strip of Parafilm. Convective co-deposition of silica template particles with the molecular carbon precursor (glucose) is accomplished by first injecting 25μL of the precursor solution in the angle between the blade and the substrate. The substrate is then driven at a prescribed rate, $7.5\mu m/s \leq u_0 \leq 20\mu m/s$, relative to the fixed blade by a linear motor, sweeping the meniscus containing the silica nanoparticle-glucose precursor solution across the substrate. Convective deposition was carried out under controlled relative humidity of below 40%.

Carbonization and template etching Co-assembled glucose-silica films were treated at 100°C and 160°C for 3 hrs each (5°C/min ramp rate) for partial polymerization and carbonization, respectively, according to Refs. [36, 37]. Subsequent carbonization was carried out for films prepared on silicon wafers and FTO glass at 900°C and 600°C, respectively, for 3 hrs under ultra-pure N_2 flow (ca. 2 L/min), with a heating ramp of 5°C/min. Following the cooling of the films, selective etching of the silica nanoparticle template was accomplished by depositing 5% wt. HF and 30% wt. KOH onto the surface of the films, supported, respectively, on Si-wafers and FTO-glass, in a sufficient quantity (e.g., ca. 2 mL for coating a ca. 1 in/ x 1.5 in film) to coat the film. Etching was carried out for 2 hrs at room temperature, followed by careful rinsing of the HF or KOH from the sample with water and ethanol. Samples were subsequently dried under ambient conditions.

Glucose-silica adsorption studies The silica nanoparticle and glucose precursor solutions employed for convective co-deposition were also used for quantifying glucose adsorption onto dispersed Lys-Sil nanoparticles. This was accomplished by equilibration of the glucose-silica nanoparticle solutions of prescribed silica solids content and incipient glucose concentration for 12 hours after their initial preparation by vigorous stirring for 1min. After equilibration, the solutions were centrifuged at 30,000 RPM for 30 min (BECKMAN L8-55M Ultracentrifuge) to separate silica nanoparticles. 100 μL of the particle-free supernatant was then extracted and mixed with 400 μL of saccharin-water solution (0.125g saccharin and 50g water), the latter employed as an internal standard for High Performance Liquid Chromatography (HPLC). HPLC

was carried out on an Agilent 1100 Series HPLC system equipped with refractive index (RID) and UV detectors, and a Bio-Rad Aminex HPX-87H column maintained at 60^{o}C. 10 µL sample injections were made with a mobile phase (0.5 mL/min) of 5 mM sulfuric acid in deionized water. The amount of glucose adsorbed on the silica particles was quantified based on measurement of the incipient glucose composition, $C_{glucose,0}$ [g/mL], and final glucose composition, $C_{glucose,f}$ [g/mL], of the equilibrated supernatant, and calculated using the approximate relation $(C_{glucose,0} - C_{glucose,f})V_{soln,o}/m_{SiO2}$. For estimating the time associated with the approach to glucose-silica adsorption equilibrium, transient study of glucose adsorption onto silica particles was carried out in a mixture of 13.33g water and 2.59mL glucose-H_2SO_4 solution (0.035 g/mL), into which 1g of pelletized Lys-Sil nanoparticle powder was added under low stirring (i.e., to avoid break-up of silica pellets and circumvent the need for centrifuge-based silica separation). Periodically, 100µL aliquots of the supernatant were removed and mixed with 400 µL of saccharin-water solution (0.125g saccharin and 50g water) for quantitative HPLC measurement of the glucose concentration as described above.

Materials characterization Scanning electron microscopy (SEM) was employed to characterize the morphology of the convectively co-deposited films. SEM was carried out on a Hitachi 4300 SE/N with accelerating voltages of 5kV and 10kV. Films supported on silicon wafers and FTO glass substrates were mounted directly on an aluminum SEM stub using conductive carbon tape, and subsequently sputter-coated with iridium to minimize charging.

Dye-sensitized solar cell (DSSC) preparation and measurement We employed DSSCs as an example system for testing the electrocatalytic performance of co-assembled 50nm porous carbon films of different thickness prepared on FTO glass substrates and incorporated as counter-electrodes in dye-sensitized solar cells. The photoanode was prepared by blade coating of Solaronix Ti-Nanoxide D paste onto an FTO surface. The anatase porous titania layer was obtained by thermal treatment at 500°C for 2 hours, and then immersed into a 0.3mM Solaronix N719 dye solution with acetonitrile/tert-butanol (volume ratio of 1:1) as solvents for over 12

hours. As a reference, a platinum cathode was prepared by blade-coating of platinum sol on FTO glass, followed with thermal treatment at 400°C for 30min. Cells were assembled with a 50μm thick spacer between the anode and counter electrode plates. The photocurrent density and photovoltage of the DSSCs were measured with active sample areas of exactly 1cm^2 using AM (air mass) -1.5 simulated sunlight produced by an ABET 10500 Low Cost Solar Simulator.

3.3 Results and Discussion

We have previously shown in Chapter 2 how evaporation-induced convective deposition of size-tunable silica nanoparticles from Lys-Sil nanoparticle solutions[29] results in multi- to near mono-layer crystalline nanoparticle films.[24] These films can be subsequently exploited as sacrificial thin film templates for carbon replication in the formation of three-dimensionally ordered mesoporous (3DOm) carbon films by a multi-step nanoreplication process.[23] Here, motivated on the one hand by the attractive properties of the hard-templated films, namely the large pore volumes, resistance to uniaxial pore shrinkage, and control over mesopore size, and on the other by the limiting multi-step character intrinsic to hard-templating strategies, we study the influence and implications of co-assembly of a surrogate molecular carbon precursor with the silica nanoparticle templates in an effort aimed at realizing 'one-pot' hard-templating of mesoporous carbon films.

3.3.1 'One-pot' template-replica co-deposition of tunable bicontinuous 3DOm carbon films

We specifically chose glucose as a low-cost carbon precursor to prepare aqueous solutions containing a prescribed volume fraction of silica nanoparticles and dilute sulfuric acid as a carbonization catalyst that we then coated on cleaned silicon substrates by convective deposition. As schematized in Figure 3.1(a), the multi-component molecular precursor/nanoparticle sols (inset a) are held between a substrate and a blade, moved relative to one another with a linear velocity, u_0. Evaporation at the contact line, formed by the fluid meniscus with the underlying

substrate, drives particle convection through the fluid to the drying front, and has been shown for as-made Lys-Sil solutions (i.e., absent the molecular carbon precursor)[24] and other larger colloidal particles[34, 38] to result in capillary particle pinning in the production of ordered crystalline nanoparticle arrays.

Figure 3.1(b) shows SEM images of the top surface and cross-section of a representative film resulting from the co-deposition of ca. 50 nm silica nanoparticles with molecular glucose from a dilute aqueous sulfuric acid solution. The presence of co-deposited glucose and sulfuric acid catalyst does not appear to disrupt the long-range nanoparticle crystallinity of the deposited films, at least for the nominal solution conditions discussed here (i.e., 3.29% v/v SiO_2, 0.035 g/mL glucose). This is somewhat striking since the sulfuric acid reduces the solution pH to 2.05 ± 0.1, close to the isoelectric point for silica. As such, the measured zeta potential of the silica nanoparticles under these solution conditions is weakly negative ($\zeta = -0.30 \pm 0.57$ mV). Despite the apparently weak electrostatic repulsion among the silica particles, the crystallinity of the nanoparticle films indicates that the particles are sufficiently stable in freshly prepared solutions so as to resist aggregation prior to their individual deposition at the drying front.

Despite little SEM-visible material within the interstices of the silica nanoparticle template in Figure 3.1(b), subsequent carbonization and HF-induced silica sacrifice results in three-dimensionally ordered mesoporous (3DOm) thin films, as confirmed by SEM images of cross-sectional and top views of the film in Figures 3.1(c) and 3.1(d), respectively. Higher-magnification SEM imaging (Figure 3.1(e)) of the periodic pore openings on the top surface of the films reveals a unique pore structure that is distinct from the pore topology obtained when pre-formed silica nanoparticle crystalline powders[30, 31] and thin films[23] are replicated by carbon back-filling. In those cases the inter-particle interstices of the colloidal template are completely filled with carbon precursor, such that subsequent polymerization, carbonization, and template etching yields three-dimensionally ordered spherical pore bodies where the template particles

once existed. Those pore bodies are interconnected by pore windows, formed by precursor occlusions at the points of contact between adjacent template particles.

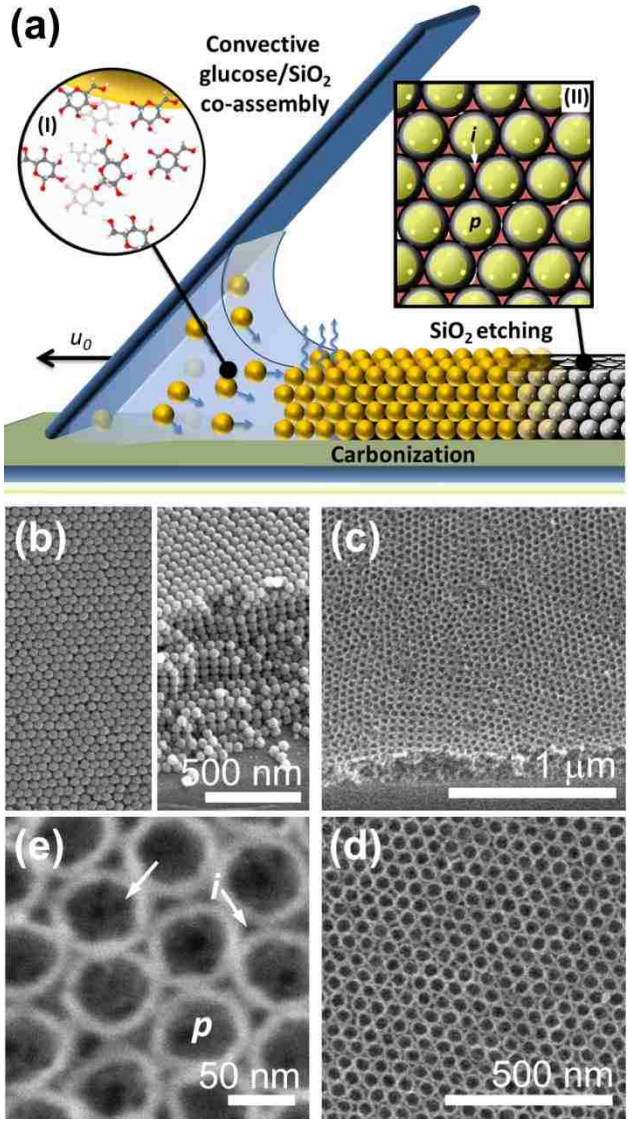

Figure 3.1: Blade-based convective co-assembly (a) of glucose and silica nanoparticles (inset I) results in (b) three-dimensionally ordered glucose-silica composite nanoparticle crystalline films, for which subsequent carbonization and silica etching leads to (c,d) three-dimensionally ordered mesoporous carbon films with (e, inset a.II) apparent bi-continuous pore structures (b3DOm C films) comprised of three-dimensionally spherical pore bodies ('*p*') connected to adjacent pore bodies by pore windows (arrow, e), and tetrahedrally and octahedrally connected interstitial pores ('*i*').

In contrast, the template-replica co-assembled films described here display an apparent bi-continuous pore structure, consisting of what appears to be two independent pore channels. One

pore channel is comprised of 3D-interconnected spherical pores (denoted as '*p*' in Figures 3.1(a), (e)) resulting from replication of the colloidal template particles. This class of pores is akin to the monomodal pores in conventional back-filled 3DOm replica materials, with pore body interconnectivity realized through pore windows, observable in Figure 3.1(e) (arrow). A second pore channel is defined by tetrahedrally and octahedrally interconnected pores (denoted as '*i*' in Figure 3.1(a)(e)) associated with the interstices of the colloidal crystal template. These interstitial pores are typically closed during conventional back-filling-based carbon replication. In the case of template-replica co-assembly, however, they remain open and apparently independent from the interconnected spherical pores, separated by carbon pore walls of only several nanometers in thickness. For simplicity and clarity, from this point forward we refer to template-replica co-assembled carbon films bearing this bi-continuous 3D-ordered mesopore topology as 'b3DOm C' films.

Typically, such bimodal mesoporous materials are prepared by adopting two templates; for soft-templating, a mixture of two block-co-polymers is adopted as a template structure,[39, 40] and for hard-templating, two precisely controlled colloidal crystal particles are used[41]. However, such dual-mesoporous materials with adjustable mesoporosity and well-defined ordered monosized porous structure have proven challenging to achieve, due to the difficulty in controlling self-assembly in dual-templating systems, which have the tendency to form micelle mixtures or to undergo macroscopic phase separation[42, 43]. These challenges only emphasize the apparent simplicity of the convective co-deposition approach described here for realizing b3DOm C films.

The b3DOm C films remain fully intact and adherent to the underlying substrate even upon templating etching. Lower magnification SEM imaging of the top surface of the films (Figure 3.2) reveals two additional remarkable characteristics, including the long-range periodicity of the mesoporous structure, as assessed based upon the pore openings on the surface of the film, and the absence of large grain boundaries or cracks. The extent of the long-range pore ordering is revealed by the FFT patterns (A-C) in Figure 3.2, computed based upon various specified areas

(a-c) of the porous carbon film. The semi-discrete nature of the diffraction patterns in FFTs (A) and (B) is indicative of subtle variability in lattice orientation among adjacent single crystalline domains and/or within a given crystalline domain spanning areas of more than 20 μm^2. We show in region (a) of the SEM image in Figure 3.2 (a) representative variation in lattice spacing of only 6^o within a given "single-crystalline" porous region. An onset of distinct polycrystallinity is observed for areas of more 30 μm^2, denoted by the ringed diffraction pattern in FFT (C).

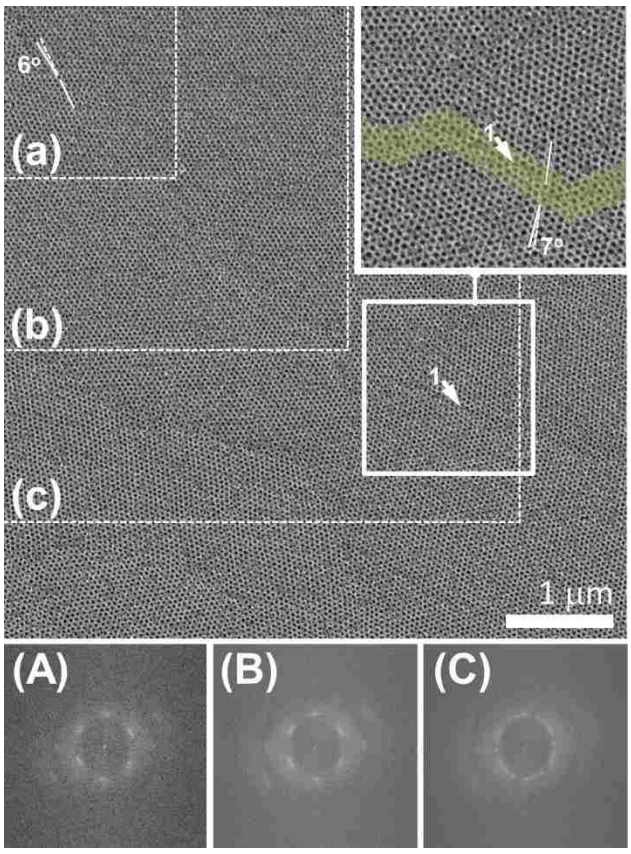

Figure 3.2: SEM image of the top surface of a b3DOm C film, with FFT diffraction patterns (A-C) computed for the correspondingly specified regions (a-c, dashed borders) of the original image. Minor mismatch of pore lattice orientation within a given crystalline region is shown in subset (a). The inset (top right) shows a magnified view of the specified grain boundary (1), across which a minor ca. 7^o mismatch in pore lattice orientation exists.

Figure 3.2 ultimately shows relatively subtle dislocations and replicated grain boundaries (e.g., arrow labeled '1', magnified view in inset SEM) marking the interface between single crystalline nanoparticle domains and, thereby, the replicated pore domains of different orientation. The grain boundaries appear to be narrow (i.e., only several template particles wide), with only

subtle mismatch in the pore lattice orientation, consistent with that which is observed within 'single-crystalline' pore domains. The subtlety of the grain boundaries in spite of the high-temperature carbonization conditions (e.g., >600^{o}C) is especially striking given that densification and opening of grain boundaries of the silica template itself are observed for template assembly in the absence of molecular glucose (see SI Figure S3.1). This suggests that the co-assembled molecular carbon precursor may help, perhaps by modulating interparticle interactions, to effectively counteract capillary forces during drying of the composite template-replica film and to, in some way, dissipate anisotropic stress build-up within the films during carbonization. The lack of cracks and large grain boundaries in the case of template-replica co-assembly is consistent with the recent findings by Aizenberg and co-workers for metal oxide systems.[25, 44] Here, we demonstrate a similar phenomenon for a system of a different composition and dramatically smaller pore forming particles, with clear implications for facile preparation of mesoporous rather than macroporous materials.

The co-assembly of b3DOm C films also allows for control of both pore size and film thickness. By exploiting the tunability of Lys-Sil nanoparticles, we demonstrate that the co-assembly process is robust to changing particle sizes. Specifically, SI Figure S3.2 shows SEM images of b3DOm C films prepared with silica template particles of several representative sizes as small as ca. 20 nm. The degree of long-range pore ordering observed for the nominal 50 nm b3DOm C films appears to persist as template particle size is decreased. Moreover, the b3DOm C morphology appears robust to changes in film thickness, which can be tuned simply by controlling the rate of deposition (u_0, Figure 3.1(a)). SI Figure S3.3 shows SEM images of cross-sections of b3DOm C films prepared by controlling the draw rate from 20 μm/s to 7.5 μm/s, with concomitant tunability of the b3DOm C film thickness (i.e., for 50 nm template particles) from as thin as ca. 200 nm to more than ca. 1 μm, respectively. Coupled with the tunability of silica particle size, and thereby mesopore size, this facile tunability of film thickness without destroying

the b3DOm C mesostructure underscores the potential versatility of this 'one-pot' template-replica co-assembly approach for realizing tunable porous carbon films.

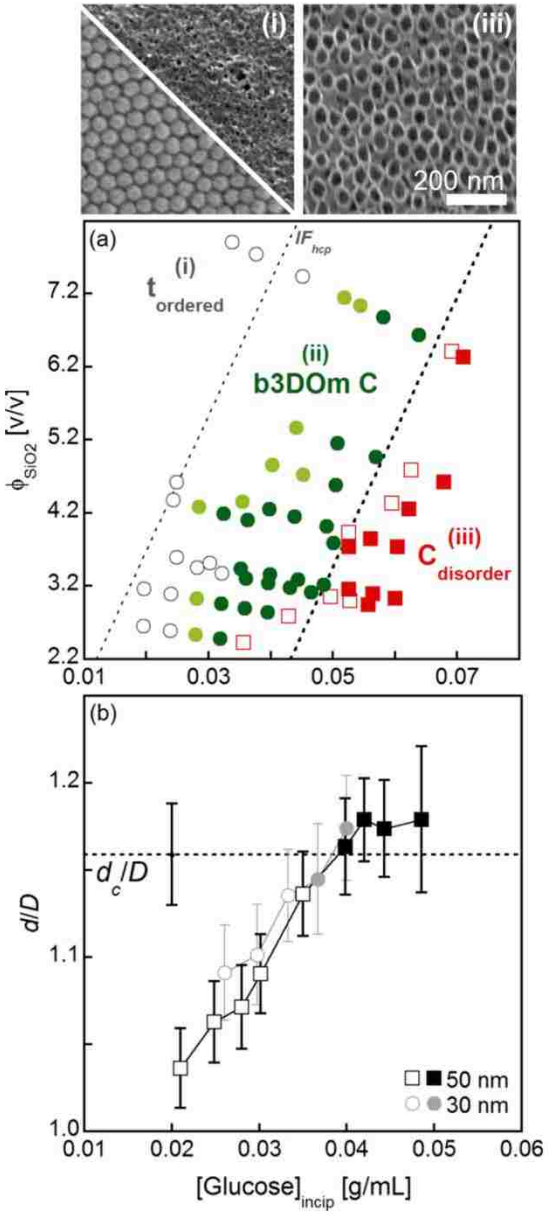

Figure 3.3: (a) Pseudo phase diagram depicting morphology of films convectively co-assembled with specified silica solids content (ϕ_{SiO2}) and incipient glucose concentration: (i) $t_{ordered}$-phase (open circles) characterized by ordered co-assembled templates, but collapsed template-etched carbon films (bottom and top SEM images (i), respectively), (ii) b3DOm C film phase (closed circles, degree of order higher for darker symbols), and (iii) $C_{disorder}$-phase (squares, degree of disorder higher for solid symbols) characterized by disordered pores (SEM image (iii)). Evolution of the normalized lattice spacing, d/D, of co-assembled template particles is shown in (b) for specified template particle sizes as a function of incipient glucose concentration, with a critical normalized lattice spacing, d_c/D specified. Lines are simply guides to the eye.

3.3.2 Mechanistic insight into b3DOm carbon pore topology

In an effort to elucidate a mechanistic understanding and specific synthesis-structure relations governing the replica-template co-assembly process, we have carried out extensive and systematic studies on the sensitivity of carbon replica film morphology to parametric combination of silica solids content (ϕ_{SiO2}) and incipient glucose composition, $[Gluocose]_{incip}$. Figure 3.3(a) maps the corresponding pseudo phase space for parametric combinations thereof, with symbols colored and shaped to denote different morphological characteristics of the resulting co-assembled films. Namely, we have employed both cross-sectional and plan view SEM imaging to assess the morphology and quality of the resulting films at two stages of fabrication: immediately after glucose-silica convective co-assembly from acidified solutions, and following *in situ* carbonization and template sacrifice. We look specifically for 2- and 3-dimensional order, assessed, respectively, by top- and cross-sectional views and analysis (e.g., FFT) of the array of pore bodies (and particles prior to template removal) comprising the co-assembled films.

Three specific classes of film morphologies emerge as the incipient glucose concentration is increased, i) those for which intermediate characterization shows long-range ordering of the co-assembled template even upon carbonization, but loss/collapse of 3D order upon template etching (termed the $t_{ordered}$ *phase*), ii) the nominal case described up to now where long-range template and b3DOm pore ordering is observed for the intermediate and etched cases, respectively, and iii) those that display disordering of the co-assembled nanoparticle template and the etched mesopores (termed $C_{disorder}$). Representative SEM images of the two newly defined film morphologies are shown for reference in Figures 3.3(i) and 3.3(iii), with the former depicting both the ordered co-assembled template and the apparently collapsed carbon replica film following template etching. A full set of SEM images tracking the evolution of the final replica film morphologies for a series of samples of similar solids content (ca. 3.97%) and systematically varied incipient glucose composition is shown in SI Figure S3.4. These images and the pseudo phase space reveal that transitions from the $t_{ordered}$ phase (i) and b3DOm C phase (ii) are fairly

diffuse, whereas the transition between the b3DOm C phase (ii) and the $C_{disorder}$ phase (iii) is more pronounced.

Two lines of reference (dashed) have been superimposed on the pseudo phase diagram in Figure 3.3a to help rationalize these transitions. Specifically, the left line labeled as IF_{hcp} represents the theoretical prediction of the incipient glucose concentration that would be required to completely fill the interstitial space of an ideal nanoparticle colloidal crystal arranged with the densest particle packing (i.e., hexagonally close-packed (*hcp*) or face-centered cubic (*fcc*)). This is estimated as $[\text{Glucose}]_{incip}=\phi_{SiO2}\cdot[\phi/(1-\phi)]_{hcp}\cdot\rho_{glu}$, where ϕ_{SiO2} is the volume fraction of silica in solution, ϕ_{hcp} is the porosity of the *hcp* arranged crystal ($\phi_{hcp}=\phi_{fcc}=0.26$) such that $(1-\phi)_{hcp}$ is the corresponding solid fraction, and ρ_{glu} is the density of solid glucose (1.54 g/mL). The IF_{hcp} line marks a locus of points associated with glucose concentration and silica volume fraction pairs for which convective co-assembly results experimentally in an ordered template before and after carbonization, but yields no 3D ordered porosity upon template sacrifice (i.e., $t_{ordered}$-phase). One would expect, however, that if the void space is, in fact, completely filled by the replicating molecular carbon (i.e., the definition of the incipient filling point), than subsequent carbonization and template removal would result in self-supporting porous structures as shown to be the case for conventional nanocasting by carbon back-filling. This suggests that more void space may be present in the actual structure (i.e., lower packing fraction) than theoretically predicted, such that a specific phase boundary between the $t_{ordered}$ and b3DOm C phases is difficult to define without *a priori* knowledge of the spacing between template particles within the co-assembled film. Instead, we simply hypothesize that the somewhat diffuse transition between the $t_{ordered}$ and b3DOm C phases results from the total co-deposited glucose falling below a critical amount required for the resulting carbon framework to be self-supporting upon template sacrifice.

We find that the IF_{hcp} line also provides a useful, albeit qualitative, reference for estimating an order-to-disorder pseudo phase boundary (right dashed line, Figure 3.3(a)). Namely, without

modification of the slope of the IF_{hcp} line, but only translation to higher glucose concentrations, we are able to thread the b3DOm C and $C_{disorder}$ experimental data remarkably well across the wide range of silica content and glucose concentrations considered. This line ultimately marks incipient glucose concentrations that are far too large for precise filling of a theoretical, hcp-packed nanoparticle crystal. Exacerbating this mismatch between theory and experiment is the specific bi-continuous morphology of the carbon replica pores (Figure 3.1(e)) appearing to have thin carbon walls in lieu of full interstitial filling. Taken together, this suggests again that the spacing between the silica template particles must be larger than theoretical *hcp* or *fcc* structures.

3.3.3 Glucose-modulation of b3DOm lattice spacing toward order-disorder limit

Insight into this discrepancy and ultimately the nature of the order-to-disorder transition can be derived from Figure 3.3(b), wherein lattice spacing, *d*, has been measured as a function of incipient glucose concentration. Namely, *d* is quantified experimentally as either particle-to-particle spacing within the co-assembled template or pore-to-pore spacing of the b3DOm C films, as assessed from plan view SEM images of each. Here, we report the normalized lattice spacing, where *D* is the average diameter of the template particle. Open symbols represent compositions for which the $t_{ordered}$ phase, (i), results from convective co-assembly, whereas closed symbols correspond to conditions for which b3DOm C films (i.e., phase (ii)) result.

Data for the 50 nm template are shown in Figure 3.3(b) with square symbols. They reveal that, underlying the pseudo-phase behavior is a sensitivity of the lattice spacing of the co-assembled template to incipient glucose concentration. Specifically, the lattice spacing increases with increasing incipient concentration of glucose. Initially, a nearly linear increase is observed before plateauing at the highest glucose concentrations in advance of the order-to-disorder transition. Analysis of the corresponding lattice spacing for b3DOm C films, prepared from various incipient glucose and silica volume fractions falling closely along the order-to-disorder transition proposed in Figure 3.3(a) (i.e., dashed right line), reveals an apparent critical

normalized lattice spacing of d_c/D = 1.16 ± 0.03, plotted as the horizontal dashed line in Figure 3.3(b). In Figure 3.3(b), we also plot the evolution of the lattice spacing for a case where 30 nm silica particles were co-assembled with molecular glucose, again denoting $t_{ordered}$ and b3DOm C films by open and closed circles, respectively. The normalized lattice spacing evolves similar to the case of the 50 nm co-assembled films with increasing incipient glucose concentration. The critical normalized lattice spacing, marking the order-to-disorder transition in the 30 nm case, is fully consistent with that which we measured for 50 nm templating. We hypothesize that the critical lattice spacing may mark a characteristic relative dimension for the co-assembled systems beyond which the crystalline template structure is no longer self-supporting.

This modulation of the lattice spacing begs questions regarding the influences of glucose. To answer these questions, we perceive that the molecular glucose ultimately assumes either a solvated state or state associated with the Lys-Sil nanoparticles within the incipient glucose-silica nanoparticle solution employed for film co-assembly. While evidence in the literature suggests little measurable glucose adsorption on unmodified silica surfaces given the hydrophilic nature of both the hydroxylated silica surface and glucose, precedence does exist for amine-mediated adsorption of glucose onto silica.[45, 46] This is of particular relevance here since the Lys-Sil nanoparticles that we use are prepared from an aqueous solution of lysine. While the as-made silica nanoparticle sols are dialyzed prior to addition of glucose and sulfuric acid, we have shown previously[47] that such dialysis, while purifying the solvent of dispersed lysine, may leave residual lysine associated with the silica surface.

We have carried out systematic experiments to assess whether glucose does adsorb onto dispersed Lys-Sil nanoparticles. Figure 3.4(a) shows a glucose adsorption isotherm for fixed incipient silica nanoparticle content over a range of incipient glucose concentrations spanning the three characteristic regions identified in the pseudo phase diagram (Figure 3.3(a)). Finite glucose adsorption onto suspended silica nanoparticles is measured, with a signature of surface saturation appearing at [Glucose]~0.05 g/mL followed by possible multi-layer adsorption indicated by the

rise in adsorbed glucose at the highest glucose concentrations probed. This saturation and apparent multi-layer adsorption coincides with the plateau in the normalized lattice spacing (Figure 3.3(b)) and the order-to-disorder transition of the corresponding co-assembled films.

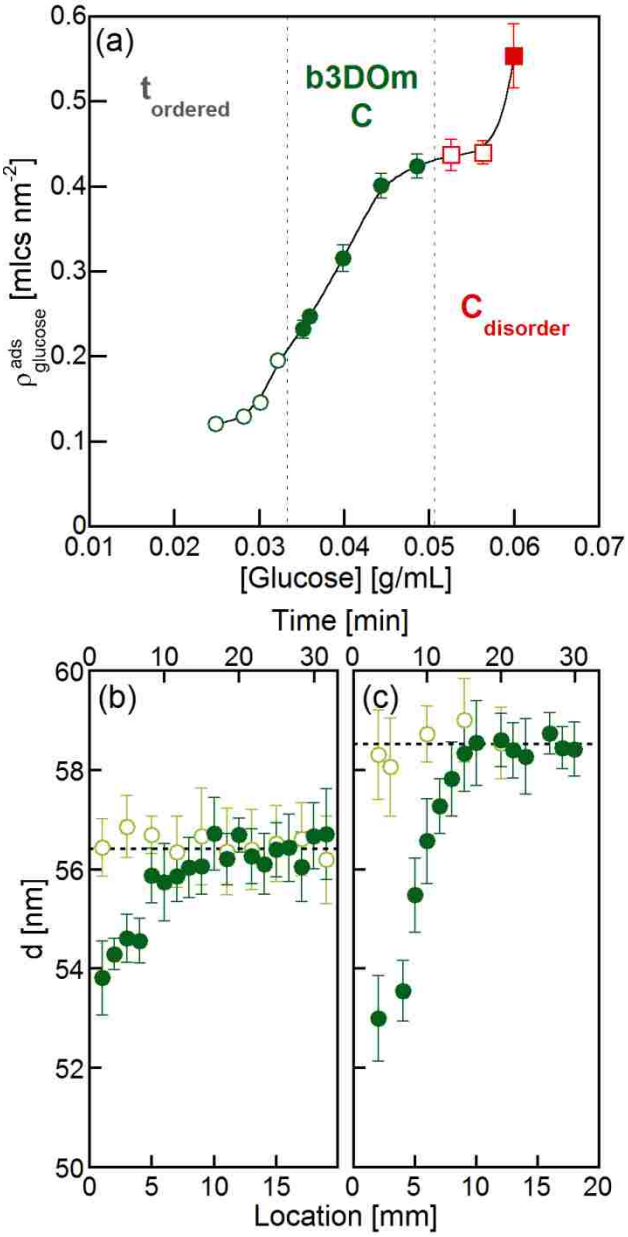

Figure 3.4: Quantification of (a) glucose adsorption onto dispersed silica nanoparticles, with symbols differentiating the corresponding phase of convectively co-assembled films among $t_{ordered}$ (open circles), b3DOm C (closed circles), and $C_{disorder}$ (squares, closed more disordered than open). The line is simply provided as a guide to the eye. Spatial variation of lattice spacing along the coating direction for convectively co-assembled films prepared from aged (open symbols) and fresh (closed symbols) glucose-silica solutions for two incipient glucose concentrations, (b) 0.035 g/mL and (c) 0.042 g/mL. Silica solids content in all cases is ca. 3.97% v/v.

While this provides tacit indication of a linkage between the lattice spacing and apparent glucose adsorption, we wish to more conclusively decouple the role therein of bulk-solvated versus silica-adsorbed glucose. Transient adsorption data presented in SI Figure S3.5 indicate that the approach to adsorption equilibrium occurs within less than 30 min. For a coating rate of 10μm/s, a film of nearly 20 mm in length can be obtained over the time period associated with the approach to equilibrium. Therefore, if the observed evolution of lattice spacing with changing incipient glucose concentration results specifically from glucose adsorption to the particle surface, a spatially dependent lattice-spacing should result from convective co-assembly of freshly prepared silica-glucose solutions (i.e., transient approach to adsorption equilibrium occurring during the duration of the coating). On the other hand, films co-deposited from aged glucose-silica solutions, wherein glucose-silica adsorption equilibrium should already be established, should result in spatially invariant lattice spacing.

We have carried out convective co-assembly of silica nanoparticles and glucose carbon precursor from freshly prepared and aged (i.e., more than 3 hrs, six times the measured approach to equilibrium) solutions. Figures 3.4(b) and 3.4(c) compare the absolute lattice spacing, *d*, for ca. 50 nm template particles measured at positions along the length of the co-assembled film (corresponding time shown on top x-axis for reference) prepared from fresh (solid symbols) and aged (open symbols) glucose-silica solutions for two incipient glucose concentrations (0.035 g/mL, 0.042 g/mL). In each case, b3DOm C films prepared from aged glucose-silica solutions (open symbols) show relatively constant lattice spacing along the length of the film, excluding initiation/edge effects. In the case of co-assembly of freshly prepared glucose-silica solutions, Figures 3.4(b) and 3.4(c) show a systematic increase in the lattice spacing extending from the leading edge of the film until a lattice constant consistent with that obtained from equilibrated solutions is reached. This provides strong evidence that the change in lattice spacing with increasing incipient concentration of the carbon precursor (Figure 3.3(b)) is governed by glucose adsorption onto the silica particle surface and its apparent modulation of inter-particle interactions.

Thus the order-to-disorder transition for b3DOm C films appears inextricably linked to and controlled by association of the molecular carbon precursor with the silica nanoparticle templates.

3.3.4 b3DOm C film deposition on rough surfaces for electrode applications

The strategy we describe here for continuous 'one-pot' nanocasting of crack-free, ordered mesoporous thin films bearing a novel bi-continuous pore topology, holds potential for applications as diverse as membrane-based macromolecular separations to electrode applications, the former exploiting the tunability of the pore size, and the latter leveraging the accessible, 3D-ordered pore volume and surface area. Briefly, here we highlight the specific potential of the scalable b3DOm C films for electrode applications, employing the counter-electrode of dye-sensitized solar cells (DSSCs) as a suitable test bed. In the process, we indirectly demonstrate the robustness of the convective template-replica co-deposition process to deviation of substrate properties away from the pristine silicon wafers employed heretofore. Namely, SI Figure S3.6 shows SEM images of representative cross-sectional views of b3DOm C films deposited on rough (i.e., characteristic roughness of hundreds of nanometers) FTO glass substrates. As in the case of films on smooth silicon wafers, here we find crack-free electrodes with thickness tunable by deposition rate from as thin as ca. 150 nm to as thick as ca. 500 nm. We package these films as a counter-electrode in a DSSC, and study the achievable overall power conversion efficiency of the cell relative to that which is possible with a lab-scale platinum counter-electrode.

The current density-voltage (IV) performance of the cells with representative thin (ca. 150 nm) and thick (ca. 500 nm) b3DOm C counter-electrodes is compared in Figure 3.5 to that achieved on the lab scale for costly platinum electrodes. The overall cell efficiency achievable with the b3DOm C films appears to be a strong function of the available surface area (i.e., film thickness), with the thickest b3DOm C electrode studied here yielding an overall cell efficiency of η=3.5%, approaching that which is achievable with a costly platinum electrode (η=4.1%). Despite being attractive given the cost differential, our focus here goes beyond the specific DSSC

cell performance toward the establishment of a versatile and apparently robust, continuous nanocasting strategy suitable for realizing novel bi-continuous, three-dimensionally ordered porous films.

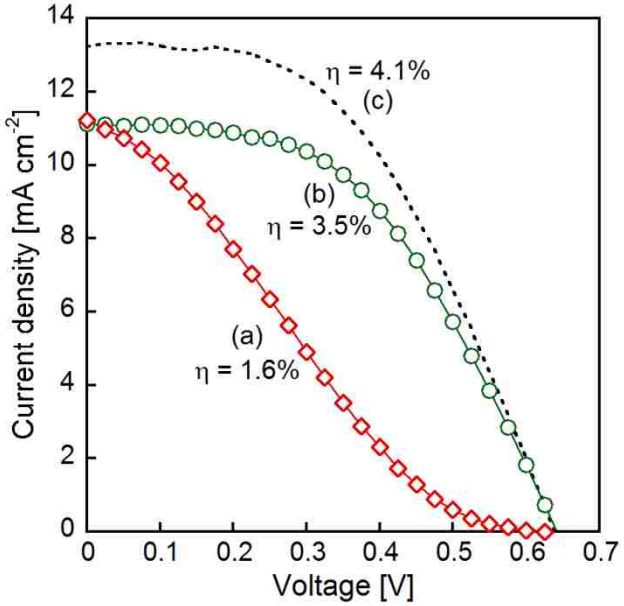

Figure 3.5: Current-voltage performance for dye-sensitized solar cells with (a) thin and (b) thick b3DOm C counter-electrodes relative to the performance of a costly (c) platinum-based electrode, with cell efficiencies, η, specified.

3.4 Conclusions

We have demonstrated how convective co-assembly of glucose as a surrogate molecular carbon precursor with size-tunable silica nanoparticles enables 'one-pot' realization of a new class of apparently bi-continuous, three-dimensionally ordered mesoporous carbon (b3DOm C) films. Tunability of the silica nanoparticle size translates to pore size control, with the b3DOm C structure also robust to control over film thickness. Systematic studies of the role of silica solids content and incipient glucose concentration in the precursor solutions, in modulating the morphology of the co-assembled films, reveal two distinct pseudo-phases beyond b3DOm C. These include carbon structures that collapse upon etching of the ordered template ($t_{ordered}$ phase) at low enough glucose compositions, and disordered mesoporous carbon films ($C_{disorder}$ phase) at

high enough glucose compositions. We identify a parametric window wherein b3DOm C films can be consistently prepared by the template-replica co-assembly approach. While the low-concentration transition between the $t_{ordered}$ and b3DOm C phases is relatively diffuse and potentially related to the deposition of a sub-critical amount of glucose required for self-supported carbon structures upon template sacrifice, the high-concentration order-to-disorder transition is defined by an apparent critical lattice spacing in the co-assembled films. Adsorption and transient convective co-assembly experiments reveal how glucose adsorption onto the silica nanoparticle surface leads to systematic increase in the lattice spacing, and triggering of this transition. Finally, we have demonstrated the robustness of this process through facile fabrication of ordered mesoporous carbon electrodes for dye-sensitized solar cells, which nearly rival the performance of costly platinum electrodes for dramatically lower cost.

3.5 Supporting Information

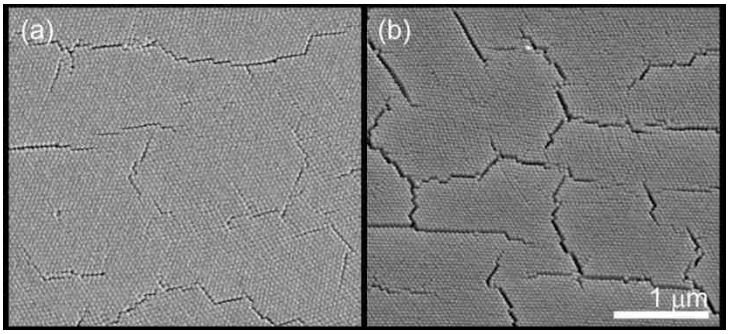

SI Figure S3.1: Grain boundary structure in convectively deposited silica nanoparticle crystalline films (i.e., from as-made solutions *without* the co-deposition of glucose) (a) before and (b) after high-temperature (900°C) calcination, showing the existence of initial grain boundaries and their opening upon calcination.

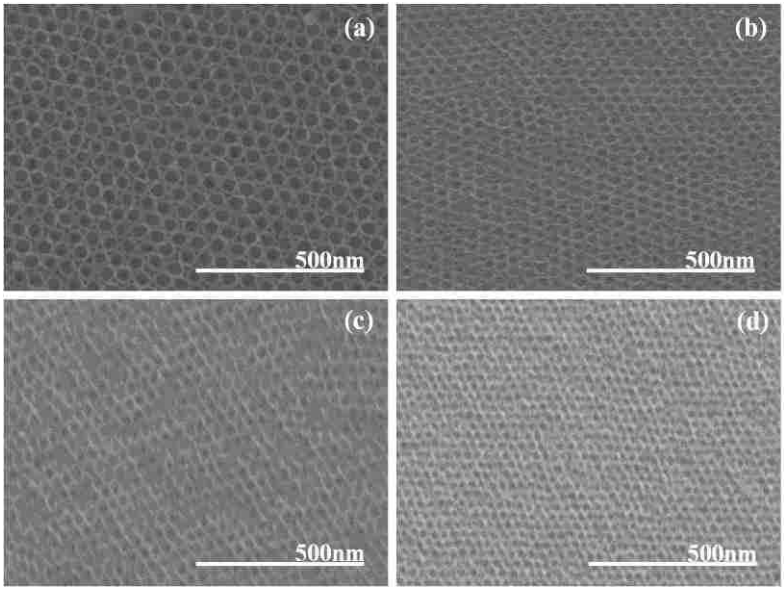

SI Figure S3.2: SEM images of the top surface of b3DOm C films synthesized using different sized templated particles: (a) 50nm, (b) 40nm, (c) 30nm and (d) 20nm.

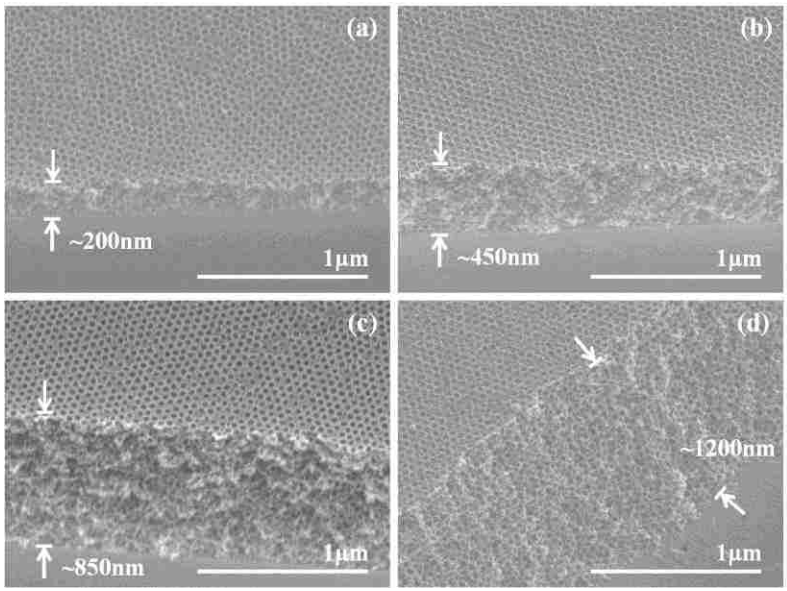

SI Figure S3.3: Cross-sectional SEM images of b3DOm C films of various thickness, resulting from convective co-assembly of 50nm silica particles with molecular glucose at prescribed coating rates, u_0, of, (a) 20μm/s, (b) 15 μm/s, (c) 10 μm/s and (d) 7.5 μm/s. In all cases, the solids content of the original silica suspension was 8.64%.

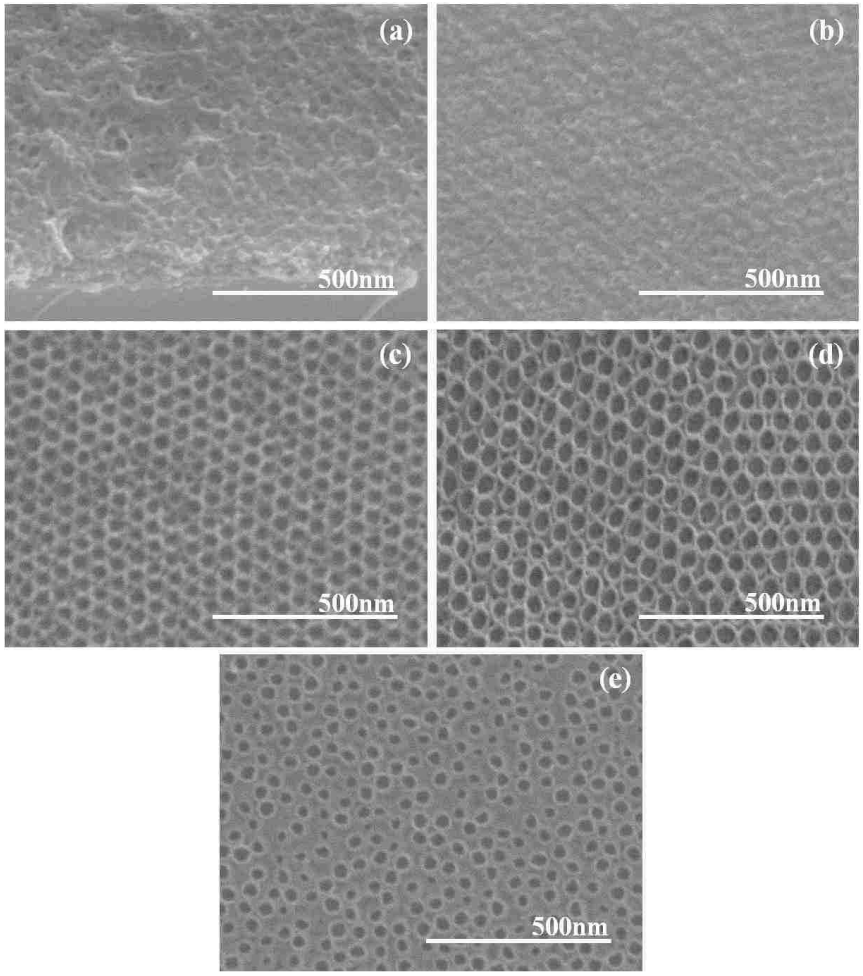

SI Figure S3.4: SEM images of films resulting from glucose-silica (50 nm) convective co-deposition, carbonization, and silica etching for incipient glucose concentrations (and assigned phases) of (a) 0.021g/mL ($t_{ordered}$-phase, i), (b) 0.028g/mL ($t_{ordered}$-phase, i), (c) 0.035g/mL (b3DOm C-phase, ii), (d) 0.042g/mL (b3DOm C-phase, ii), and (e) 0.054g/mL ($C_{disorder}$-phase, iii).

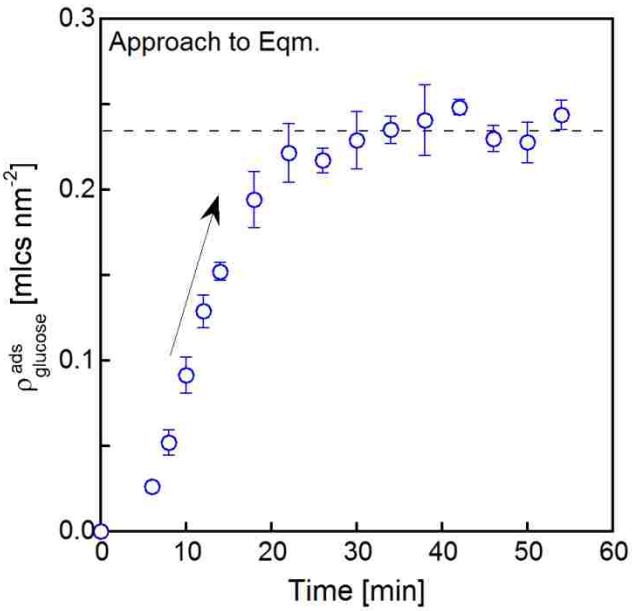

SI Figure S3.5: Transient adsorption of glucose at incipient concentration [Glucose]$_{incip}$ = 0.035 /mL, revealing that the approximate approach to equilibrium occurs over a period of ca. 30 min. This estimate of the time to equilibrium may be elongated by mass transport limitations associated with molecular diffusion into the large (i.e., several mm) sized 50 nm silica colloidal crystal employed for this specific transient study.

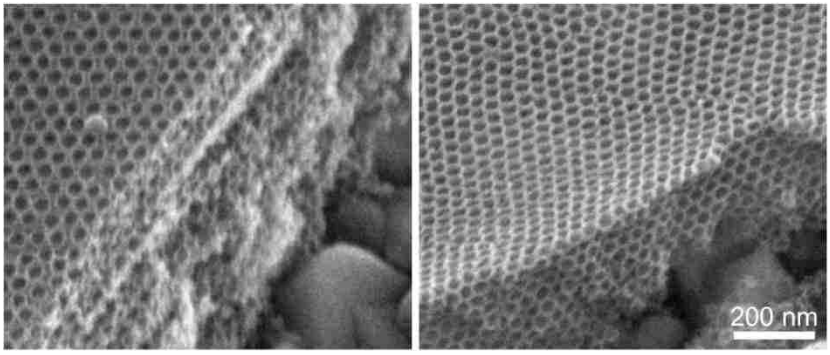

SI Figure S3.6: Representative cross-sectional SEM images of b3DOm C films deposited by template (50 nm Lys-Sil particles)-replica convective co-deposition directly on the rough polycrystalline surface of FTO glass as counter-electrodes for dye-sensitized solar cells (DSSCs).

3.6 Reference:

1. Liang, C. D.; Dai, S. Synthesis of mesoporous carbon materials via enhanced hydrogen-bonding interaction. *Journal of the American Chemical Society* **2006,** *128* (16), 5316-5317.

2. Ma, T. Y.; Liu, L.; Yuan, Z. Y. Direct synthesis of ordered mesoporous carbons. *Chemical Society Reviews* **2013,** *42* (9), 3977-4003.

3. Xia, Y.; Yang, Z.; Mokaya, R. Templated nanoscale porous carbons. *Nanoscale* **2010,** *2*, 639-659.

4. Zhao, X. S.; Su, F.; Yan, Q.; Guo, W.; Bao, X. Y.; Lv, L.; Zhou, Z. Templating methods for prepation of porous structures. *J. Mater. Chem.* **2006,** *16*, 637-648.

5. Tao, Y.; Endo, M.; Inagaki, M.; Kaneko, K. Recent progress in the synthesis and applications of nanoporous carbon films. *J. Mater. Chem.* **2011,** *21*, 313-323.

6. Liang, C. D.; Hong, K. L.; Guiochon, G. A.; Mays, J. W.; Dai, S. Synthesis of a large-scale highly ordered porous carbon film by self-assembly of block copolymers. *Angew. Chem.-Int. Edit.* **2004,** *43* (43), 5785-5789.

7. Meng, Y.; Gu, D.; Zhang, F. Q.; Shi, Y. F.; Cheng, L.; Feng, D.; Wu, Z. X.; Chen, Z. X.; Wan, Y.; Stein, A.; Zhao, D. Y. A family of highly ordered mesoporous polymer resin and carbon structures from organic-organic self-assembly. *Chemistry of Materials* **2006,** *18* (18), 4447-4464.

8. Meng, Y.; Gu, D.; Zhang, F. Q.; Shi, Y. F.; Yang, H. F.; Li, Z.; Yu, C. Z.; Tu, B.; Zhao, D. Y. Ordered mesoporous polymers and homologous carbon frameworks: Amphiphilic surfactant templating and direct transformation. *Angew. Chem.-Int. Edit.* **2005,** *44* (43), 7053-7059.

9. Schuster, J.; Kohn, R.; Doblinger, M.; Keilbach, A.; Amenitsch, H.; Bein, T. In Situ SAXS Study on a New Mechanism for Mesostructure Formation of Ordered Mesoporous Carbons: Thermally Induced Self-Assembly. *Journal of the American Chemical Society* **2012,** *134* (27), 11136-11145.

10. Song, L. Y.; Feng, D.; Campbell, C. G.; Gu, D.; Forster, A. M.; Yager, K. G.; Fredin, N.; Lee, H. J.; Jones, R. L.; Zhao, D. Y.; Vogt, B. D. Robust conductive mesoporous carbon-silica composite films with highly ordered and oriented orthorhombic structures from triblock-copolymer template co-assembly. *Journal of Materials Chemistry* **2010,** *20* (9), 1691-1701.

11. Tanaka, S.; Katayama, Y.; Tate, M. P.; Hillhouse, H. W.; Miyake, Y. Fabrication of continuous mesoporous carbon films with face-centered orthorhombic symmetry through a soft templating pathway. *J. Mater. Chem.* **2007,** *17*, 3639-3645.

12. Jin, J.; Nishiyama, N.; Egashira, Y.; Ueyama, K. Vapor phase synthesis of ultrathin carbon films with a mesoporous monolayer by a soft-templating method. *Chem. Commun.* **2009**, 1371-1373.

13. Kataoka, S.; Yamamoto, T.; Inagi, Y.; Endo, A.; Nakaiwa, M.; Ohmori, T. Synthesis of ordered mesoporous carbon thin films at various temperatures in vapor infiltration method. *Carbon* **2008,** *46* (10), 1358-1360.

14. Huang, E.; Rockford, L.; Russell, T. P.; Hawker, C. J. Nanodomain control in copolymer thin films. *Nature* **1998,** *395*, 757-758.

15. Song, L.; Feng, D.; Fredin, N. J.; Yager, K. G.; Jones, R. L.; Wu, Q.; Zhao, D.; Vogt, B. D. Challenges in fabrication of mesoporous carbon films with ordered cylindrical pores via phenolic oligomer self-assembly with triblock copolymers. *ACS Nano* **2010,** *4* (1), 189-198.

16. Lee, J.; Yoo, S.; Hyeon, T.; Oh, S. M.; Kim, K. B. Synthesis of a new mesoporous carbon and its application to electrochemical double-layer capacitors. *Chem. Commun.* **1999,** (21), 2177-2178.

17. Ryoo, R.; Joo, S. H.; Jun, S. Synthesis of highly ordered carbon molecular sieves via template-mediated structural transformation. *Journal of Physical Chemistry B* **1999,** *103* (37), 7743-7746.

18. Pang, J.; Li, Z.; Wang, D.; Wu, Z.; Joh, V. T.; Yang, Z.; Lu, Y. Silica-templated continuous mesoporous carbon films by a spin-coating technique. *Adv. Mater.* **2004,** *16* (11), 884-886.

19. Reculusa, S.; Agricole, B.; Derre, A.; Couzi, M.; Sellier, E.; Ravaine, S.; Delhaes, P. Carbon membranes of controlled thickness from colloidal crystals. *Advanced Materials* **2006,** *18* (13), 1705-1708.

20. Gierszal, K. P.; Jaroniec, M. Carbons with extremely large volume of uniform mesopores synthesized by carbonization of phenolic resin film formed on colloidal silica template. *Journal of the American Chemical Society* **2006,** *128* (31), 10026-10027.

21. Brinker, C. J.; Lu, Y. F.; Sellinger, A.; Fan, H. Y. Evaporation-induced self-assembly: Nanostructures made easy. *Adv. Mater.* **1999,** *11*, 579-585.

22. Wei, T.-C.; Hillhouse, H. W. Mass transport and electrod accessibility through periodic self-assembled nanoporous silica thin films. *Langmuir* **2007,** *23*, 5689-5699.

23. Tian, Z.; Snyder, M. A. Hard-templating of symmetric and asymmetric carbon thin films with three-dimensionally ordered mesoporosity. *Langmuir* **2014,** *Submitted*.

24. Snyder, M. A.; Lee, J. A.; Davis, T. M.; Scriven, L. E.; Tsapatsis, M. Silica nanoparticle crystals and ordered coatings using Lys-Sil and a novel coating device. *Langmuir* **2007,** *23*, 9924-9928.

25. Hatton, B.; Mishchenko, L.; Davis, S.; Sandhage, K. H.; Aizenberg, J. Assembly of large-area, highly ordered, crack-free inverse opal films. *Proceedings of the National Academy of Sciences of the United States of America* **2010,** *107* (23), 10354-10359.

26. Mishchenko, L.; Hatton, B.; Kolle, M.; Aizenberg, J. Patterning hierarchy in direct and inverse opal crystals. *Small* **2012,** *8* (12), 1904-1911.

27. Vasquez, Y.; Kolle, M.; Mishchenko, L.; Hatton, B. D.; Aizenberg, J. Three-phase co-assembly: In situ incorporation of nanoparticles into tunable, highly ordered, porous silica films. *ACS Photonics* **2013,** *1*, 53-60.

28. Guo, W. H.; Wang, M.; Xia, W.; Dai, L. H. Two Substrate-Confined Sol-Gel Coassembled Ordered Macroporous Silica Structures with an Open Surface. *Langmuir* **2013,** *29* (20), 5944-5951.

29. Davis, T. M.; Snyder, M. A.; Krohn, J. E.; Tsapatsis, M. Nanoparticles in lysine-silica sols. *Chemistry of Materials* **2006,** *18* (25), 5814-5816.

30. Fan, W.; Snyder, M. A.; Kumar, S.; Lee, P. S.; Yoo, W. C.; McCormick, A. V.; Penn, R. L.; Stein, A.; Tsapatsis, M. Hierarchical nanofabrication of microporous crystals with ordered mesoporosity. *Nature Materials* **2008,** *7* (12), 984-991.

31. Yokoi, T.; Sakamoto, Y.; Terasaki, O.; Kubota, Y.; Okubo, T.; Tatsumi, T. Periodic arrangement of silica nanospheres assisted by amino acids. *Journal of the American Chemical Society* **2006,** *128* (42), 13664-13665.

32. Yokoi, T.; Wakabayashi, J.; Otsuka, Y.; Fan, W.; Iwama, M.; Watanabe, R.; Aramaki, K.; Shimojima, A.; Tatsumi, T.; Okubo, T. Mechanism of Formation of Uniform-Sized Silica Nanospheres Catalyzed by Basic Amino Acids. *Chemistry of Materials* **2009,** *21* (15), 3719-3729.

33. Iler, R. K. *The Chemistry of Silica*; John Wiley & Sons: New York, 1979.

34. Kumnorkaew, P.; Ee, Y. K.; Tansu, N.; Gilchrist, J. F. Investigation of the Deposition of Microsphere Monolayers for Fabrication of Microlens Arrays. *Langmuir* **2008,** *24* (21), 12150-12157.

35. Kumnorkaew, P.; Gilchrist, J. F. Effect of Nanoparticle Concentration on the Convective Deposition of Binary Suspensions. *Langmuir* **2009,** *25* (11), 6070-6075.

36. Jun, S.; Joo, S. H.; Ryoo, R.; Kruk, M.; Jaroniec, M.; Liu, Z.; Ohsuna, T.; Terasaki, O. Synthesis of new, nanoporous carbon with hexagonally ordered mesostructure. *Journal of the American Chemical Society* **2000,** *122* (43), 10712-10713.

37. Wang, X. X.; Li, G.; Wang, W. H.; Jin, C. Z.; Chen, Y. Y. Synthesis, characterization and catalytic performance of hierarchical TS-1 with carbon template from sucrose carbonization. *Microporous and Mesoporous Materials* **2011,** *142* (2-3), 494-502.

38. Prevo, B. G.; Velev, O. D. Controlled, rapid deposition of structured coatings from micro- and nanoparticle suspensions. *Langmuir* **2004,** *20*, 2099-2107.

39. Zhang, J. Y.; Deng, Y. H.; Wei, J.; Sun, Z. K.; Gu, D.; Bongard, H.; Liu, C.; Wu, H. H.; Tu, B.; Schuth, F.; Zhao, D. Y. Design of Amphiphilic ABC Triblock Copolymer for Templating Synthesis of Large-Pore Ordered Mesoporous Carbons with Tunable Pore Wall Thickness. *Chemistry of Materials* **2009,** *21* (17), 3996-4005.

40. Niu, D. C.; Ma, Z.; Li, Y. S.; Shi, J. L. Synthesis of Core-Shell Structured Dual-Mesoporous Silica Spheres with Tunable Pore Size and Controllable Shell Thickness. *Journal of the American Chemical Society* **2010,** *132* (43), 15144-15147.

41. Kuroda, Y.; Sakamoto, Y.; Kuroda, K. Selective Cleavage of Periodic Mesoscale Structures: Two-Dimensional Replication of Binary Colloidal Crystals into Dimpled Gold Nanoplates. *Journal of the American Chemical Society* **2012,** *134* (20), 8684-8692.

42. Kuang, D. B.; Brezesinski, T.; Smarsly, B. Hierarchical porous silica materials with a trimodal pore system using surfactant templates. *Journal of the American Chemical Society* **2004,** *126* (34), 10534-10535.

43. Smarsly, B.; Antonietti, M. Block copolymer assemblies as templates for the generation of mesoporous inorganic materials and crystalline films. *European Journal of Inorganic Chemistry* **2006,** (6), 1111-1119.

44. Phillips, K. R.; Vogel, N.; Hu, Y. H.; Kolle, M.; Perry, C. C.; Aizenberg, J. Tunable Anisotropy in Inverse Opals and Emerging Optical Properties. *Chemistry of Materials* **2014,** *26* (4), 1622-1628.

45. Kulikova, G. A.; Ryabinina, I. V.; Parfenyuk, E. V. Effect of chemical nature of nanosized silica surface on the adsorption of D-glucose. *Colloid Journal* **2010,** *72* (2), 224-229.

46. Francisco, M.; Mlinar, A. N.; Yoo, B.; Bell, A. T.; Prausntiz, J. M. Recovery of gluose from an aqueous ionic liquid by adsorption onto a zeolite-based solid. *Chemical Engineering Journal* **2011,** *172*, 184-190.

47. Snyder, M. A.; Demirgoez, D.; Kokkoli, E.; Tsapatsis, M. Benign, 3D encapsulation of sensitive mammalian cells in porous silica gels formed by Lys-Sil nanoparticle assembly. *Micropor. Mesopor. Mater.* **2009,** *118*, 387-395.

Chapter 4: Hard-template-mediated hierarchical control of porous carbon powders

4.1 Introduction

Recent developments in portable electronics have promoted the increasing demand for high-performance energy-storage systems that are lightweight and flexible, such as solar cells[1], photovoltaic cells[2, 3] and Li-ion batteries[4, 5]. Among these systems, supercapacitors are an important class of energy-storage devices that have attracted significant attention because of their higher power density, cycle efficiency, and charge/discharge rates as compared to traditional batteries[6]. Energy storage within supercapacitors is based upon charge accumulation in the double layer formed at the electrode/electrolyte interface.[7] As such, electrode surface area, its facile molecular accessibility, and electrical conductivity are critical design factors determining how well supercapacitor electrodes[8] are capable of achieving high performance in terms of both capacitance and rate.

Due to abundant availability and structural diversity, porous carbon is one of the most studied electrode materials. Tunable microporosity of carbons can lead to large surface areas suitable for enhancing capacitance. Yet, the narrowness of micropores (i.e., < 2 nm) precludes facile access by the liquid electrolyte, and thereby adversely impacts the power performance of purely microporous materials. Alternatively, hierarchically porous materials comprised of microporous frameworks percolated by larger pores (e.g., mesopores, macropores) can facilitate electrolyte access to the micropores and thus electrode performance.[9, 10]

While transport limitations can be reduced by simply increasing pore size, a trade-off exists between concomitant losses in active micropore volume, and thus power density, and gains in transport enhancement. Specifically, large macropores waste active volume of the material, reducing its specific energy density in their capacity only as electrolyte reservoirs and

contributing little to the total capacitance. Alternatively, hierarchical carbons that combine large micropore volumes suitable for ion storage with intercalated mesopores capable of facilitating ion transport, serve as desirable electrode morphologies for high-performance supercapacitors. Moreover, the ability to realize highly monodisperse, three-dimensionally ordered and interconnected mesopore topologies within a microporous matrix in lieu of broadly distributed and disordered mesopores is desired. Such ordered mesopore topologies ultimately facilitate ion transport by minimizing characteristic diffusion length.[11]

To date, the utilization of various carbonaceous chemicals, including graphitic materials, carbide-derived carbons (CDCs), carbon nanotubes (CNTs), activated carbons (ACs) and ordered mesoporous carbons (OMCs) has been widely studied for usage as electrochemical double-layer capacitors (EDLCs). While these materials bear attractive features for applications as supercapacitor electrodes, each also faces drawbacks. For example, despite exceptionally high thermal and electrical conductivity as well as high surface area of up to 2675m^2/g, graphene sheets have a tendency to restack during all phases of preparation and subsequent electrode production procedures, leaving intergraphene pore sizes that are insufficient for facile electrolyte access and the formation of electrochemical double-layer charges/discharges.[12] Even after chemical post-treatment to obtain reduced graphene oxide (rGO) through oxidation-derived intercalation expansion and then quick removal of these oxygen groups, the obtained samples are only partially exfoliated and still contain extensive domains of staked graphitic layers. The obtained samples are wormlike or accordion-like and therefore characterized by an apparently lower specific surface area (typically lower than 100 m^2/g) compared to the few-layered graphenes reported recently.[13] CDCs can only deliver a high capacitance at a moderate rate of charge and discharge due to relatively slow ion-shell desolvation and ion transport in micropores (less than 1 nm).[14]

CNTs have unique pore structure and superior electronic conductivity and stability; however, most of the CNTs are known to bundle together due to van der Waals forces, where only the

outermost tubes in a bundle are accessible to the electrolyte and the inter-tube space is insufficient for the formation of EDL.[15] In addition, challenges in purification and the high cost of CNT production stymie their practical application.[7]

Despite develoments of more exotic materials, currently high surface-area activated carbons remain the predominant electrode materials for commercial supercapacitors. However, only about 10%~20% of the "theoretical" capacitance is achievable with ACs due to the presence of electrolyte-inaccessible micropores, electrolyte wetting deficiencies, and/or the inability to successfully form a double layer in the pores.[16]

To overcome this drawback, ordered mesoporous carbons (OMCs) with a narrow distribution in the mesopore range (2–50 nm) and a uniform pore connection have been studied.[14] These OMCs exhibit much better electrochemical performance than conventional ACs, especially at high current rates since the ordered mesopore channels and interconnections provide a more favorable path for ion transport.[11] Two common approaches to realizing ordered mesoporous carbons with large meso- and micropore volumes and concomitantly high surface areas include so-called soft- and hard-templating. As discussed in Chapter 1, the former approach benefits from its 'one-pot' process, but suffers from the undulating nature of the templated pores, their often limited dimensionality, and their tendency to shrink or even collapse under high-temperature processing employed, for example, in the case of electrode materials, for improving graphene content. The latter approach employs a multi-step process, involving the pre-fabrication of a porous template for subsequent carbon replication, replica-template processing (i.e., polymerization, carbonization, and possible graphitization), and template sacrifice.

Early reports of CMK carbon materials, resulting from hard-templating on SBA-15, have demonstrated how a combination of micropore-derived high surface area and ordered mesoporosity can lead to attractive supercapacitor performance. Additional improvement in supercapacitor performance has more recently been demonstrated by structures derived from

assembly of graphitic sheets into mesoporous materials, yet economical approaches to 3D-ordered mesostructured electrodes with high graphitic content remain a challenge.

As an alternative to conventional hard-template-derived mesoporous carbons such as those in the CMK class of materials, which require synthesis of SBA silica templates and thereby a complex multi-step fabrication process, we have previously established strategies for realizing 3DOm carbon powders by facile replication of pre-formed colloidal crystals comprised of size-tunable (ca. 10-50 nm) silica nanoparticles[17]. The resulting carbon replica structures are endowed with 3D-ordered spherical pore bodies of diameters concomitant with the template particles that are connected via window constrictions to adjacent pore bodies. In order to have high energy densities under high charge/discharge rates, the 3D interconnected porous structure in a carbon electrode is desired. As such, one advantage of the hard-templating technique employing silica colloidal crystals is the stability the template provides for the carbon framework during carbonization at high temperature (i.e. 900°C in this work), thus preventing structural collapse. While the pore topology of the resulting 3DOm carbon materials offers large pore volumes, and the framework is amenable to micropore activation by high-temperature KOH treatment employed to remove the silica template[18], these materials suffer from the multi-step nature of their synthesis, a general bane of the hard-templating or nanocasting process.

In this Chapter, we leverage the mechanistic insight from the template-precursor co-assembly described in Chapter 3 to establish a new route to hierarchical, bi-continuous 3D-ordered mesoporous carbon powders (b3DOm C). Beyond bringing the nanocasting process in line with the ‘one-pot’ soft-templating approach, this new strategy toward hard-templating of porous materials offers distinct advantages in terms of bolstering pore topology during carbonization, establishing three-dimensional order, interconnectivity, and bi-continuity of the resulting pore topology with large pore volumes and activated micropore surface areas exceeding what is possible by conventional multi-step routes. Moreover, unforeseen benefits of the co-assembly process include apparent template-mediated control over interfacial microstructure of the carbon,

namely the tunability of the sp^2-hybridized fraction of the resulting b3DOm C frameworks. We test this novel carbon structure as a potentially stable and high-capacitance supercapacitor electrode, and demonstrate attractive power density, discharge rate, and cyclic stability relative to the reported performance of comparable reference materials from the literature.

4.2 Materials and Methods

Materials. The following reagents were used without further purification: tetraethyl orthosilicate (TEOS, 98%), sulfuric acid (H_2SO_4, 98%), L-lysine (98%), D-glucose, acetylene carbon black (99.99% wt.), polyvinylidene fluoride (PVdF) and 1-methyl-2-pyrrolidinone (NMP) were obtained from Sigma-Aldrich and Acros Organics. Potassium hydroxide (KOH, ACS grade) was obtained from BDH. Millipore water with resistivity 18MΩ/cm was used for all reactions.

Silica nanoparticle synthesis. Highly monodisperse silica nanoparticles were prepared following previous reports on direct and seeded amino acid facilitated synthesis of Lys-Silica particles[17, 19, 20, 21]. Typically, L-lysine was dissolved in water under vigorous stirring for 0.5 hr within an oil bath at 90°C. TEOS was subsequently hydrolyzed in the aqueous L-Lysine solutions at 90°C under vigorous stirring for at least 12 hrs. The silica seed nanoparticles were synthesized directly, with a molar composition, x SiO_2/ y Lysine/ z water/ $4x$ ethanol, of x=60, y=1.23, z=9500. Additional TEOS was introduced multiple times until the prescribed molar composition (x=1120, y=1.23, z=9500) of the 50 nm particle sol was reached, with intermediate hydrolysis at 90°C for at least 12 hrs following each aliquot addition. Dialysis of the resulting 50nm silica suspensions was carried out against water for 3 days with mild stirring using Spectra/Por® dialysis bags (Spectrum Labs, MW cutoff of 3500). Water was exchanged every 8 hrs.

Co-assembly of bi-continuous 3D ordered mesoporous carbon (b3DOm C). Glucose-based carbon precursor solution was typically prepared by dissolving 2.5 g of glucose into an acid solution, composed of 10 µL 98% wt. H_2SO_4 and 10 g of water. A variety of co-assembly suspensions were prepared by adding different amounts of glucose precursor solution into

dialyzed silica suspensions. For example, using 1 mL dialyzed 50 nm silica nanoparticle suspensions of 3.79% by vol. solids content, 0.11 mL of the glucose-acid solution was added to achieve silica-carbon precursor suspensions with a glucose concentration of 0.021g/mL. Similarly, 0.15 mL, 0.20 mL and 0.24 mL of the glucose-acid solution was added dropwise to the dialyzed silica solution to achieve prescribed glucose concentrations of 0.028 g/mL, 0.035 g/mL, and 0.040g/mL, respectively. Equilibration of the silica and glucose carbon precursors in suspension was carried out under vigorous stirring for at least 3 hrs. Co-assembly of the 50 nm silica nanoparticles and glucose carbon precursor as carried out by evaporative drying at room temperature in a vented turbulent-flow fume hood.

The freshly dried co-assembled silica-glucose composite powders were then thermally treated at 100°C and 160°C, each for 3 hrs for respective polymerization and partial carbonization[22, 23]. The resulting carbon-silica composites were fully carbonized at 900°C for 3 hrs under ultra-high pure N_2 flow (~2L/min) with a heating ramp of 5°C/min. 30% wt. KOH solution was used to etch the silica nanoparticle template at room temperature for 3 days. Aqueous washing and centrifugation steps were employed to respectively rinse excess reactants and etching agents and isolate b3DOm C powders for subsequent drying at 70^{o}C.

Preparation of 3DOm carbon. An incipient wetness technique was used to prepare traditional hard-templated 3DOm carbon. The same glucose-acid solution used for co-assembly was used as the carbon source. For example, 1.445 mL of glucose-acid solution was dropped onto 1g of 50 nm colloidal crystalline powder prepared by room temperature drying of dialyzed silica, followed by evaporation of water at room temperature. The same carbonization and etching processes employed for the co-assembled materials were applied to realize 3DOm carbon powders.

Product characterization. Scanning electron microscopy (SEM, Hitachi 4300 SE/N, 5kV and 10kV), transmission electron microscopy (TEM, JEOL JEM-2000FX, 200kV) and high-resolution TEM (HRTEM, JEM-ARM 200F) were used to characterize the carbon materials.

Raman spectra were recorded by using a Horiba-Jobin Yvon LabRam HR Raman system. Nitrogen adsorption and desorption isotherms were measured at 77 K with a Micromeritics ASAP 2020 system. The Brunaer–Emmett-Teller (BET) method was used for the determination of the surface area. XPS measurements were taken on a Scienta ESCA-300 spectrometer with a monochromatic Al Kα X-ray source at a power of up to 7.5kW and a multichannel detector.

Electrochemical measurement. For the preparation of electrodes, the b3DOm C powders were mixed with 5% wt. polyvinylidene fluoride (PVdF, dissolved in NMP of 0.025g/mL as the binder) and 5% wt. carbon black in ethanol and extensively ground in a mortar to form a homogeneous mixture. The resulting sticky slurry was pressed onto carbon cloth and dried in an oven at 70°C for 12hr. The typical mass load of the active b3DOm C in an electrode was 5mg.

The electrochemical study was performed in a three-electrode test system. The b3DOm C powders acted as the working electrode. Ag/AgCl with saturated KCl and a Pt sheet were adopted as the reference and counter electrodes, respectively. Electrochemical measurements of the asymmetric supercapacitors were carried out using 1M H_2SO_4 and 6M KOH aqueous solutions as electrolytes. Cyclic voltammetry (CV), galvanostatic charge/discharge and electrochemical impedance spectroscopy (EIS) experiments were performed on a Gamry Instruments Reference 3000 at room temperature. CV was performed at different voltage scan rates, between 1 mV/s and 200 mV/s, with the range from 0 to -1V in KOH and from -0.2 to 0.8V in H_2SO_4. Galvanostatic measurements were carried out at various rates, from 1 A/g to 10 A/g. Electrochemical impedance spectroscopy (EIS) measurements were recorded from 1MHz to 10mHz with 5mV sinusoidal voltage input.

4.3 Results and Discussions

4.3.1 Leveraging thin film co-assembly for realizing b3DOm C powders

Guided by elucidation of the silica-carbon precursor co-assembly mechanism discussed in Chapter 3, here we explore its extension to the preparation of bulk carbon powders. Namely, in

the case of co-assembled thin films, a parametric window was identified in the pseudo-phase space, defined by carbon precursor concentration and silica volume fraction, wherein self-supporting bi-continuous ordered mesoporous carbon (b3DOm C) films could be realized. While an order-disorder transition was observed at high enough carbon precursor concentrations, the lower bound on the parametric window marked a transition between b3DOm C films and ordered co-assembled structures that, once etched, yielded no self-supporting porous carbon structure. This lower bound on carbon precursor concentration, therefore, was attributed to the lack of sufficient carbon deposition during the co-assembly process, and thus reduced mechanical stability of the resulting material.

Guided by the pseudo phase space derived from convective thin film assembly, we have studied the bulk co-assembly of silica nanoparticles with carbon precursors at specific points spanning the identified parametric coating window. We find that the bound for order-disorder transition persists in the case of bulk assembly, with b3DOm C materials and disordered mesoporous carbons produced at carbon precursor concentrations lower and higher, respectively, than those defining the order-disorder transition for thin films. Distinct differences, however, are observed between the bulk and thin film assembly at the lower parametric bound, predicted in the case of thin films, where b3DOm C films can still be realized. Namely, in bulk co-assembly of the silica template particles and the carbon precursor, b3DOm C materials can be realized at carbon precursor concentrations well below the concentration limits determined in thin film studies. While the pseudo phase space associated with bulk co-assembly appears to agree well with thin-film predictions for upper compositional limits, the b3DOm C viability window is largely expanded to include carbon precursor compositions well below the lower compositional limits predicted by thin film co-assembly. In other words, concentrations associated with what was identified as "$t_{ordered}$" and "b3DOm C" phases in the b3DOm C film studies in Chapter 3 (Figure 3.3), both lead to b3DOm C powders. Similar to the case of co-assembled b3DOm C films, conditions associated with the "$C_{disorder}$" phase for the thin films result in disordered

mesoporous powders. We attribute this largely expanded parametric phase space to the subtle difference between bulk and convective assembly, wherein all of the carbon precursor must deposit on the template during solvent evaporation in the case of the former, while only the local carbon precursor confined to the interstices of the convectively deposited film must deposit in the case of the latter.

Figure 4.1(a) shows SEM images of a cleaved surface of a representative b3DOm C powder, showing evidence of the hierarchical bi-continuous mesoporous framework within the bulk carbon structures akin to that observed for the thin films in Chapter 3. Here, again, these separate, but inter-digitated pore topologies are associated with i) the spherically interconnected pore bodies templated by the silica nanoparticles and ii) the 3D-interconnected interstitial spaces isolated from the spherical pore bodies by thin carbon walls as highlighted by arrows in Figure 4.1(a). The pore topologies of the b3DOm C materials exist in stark contrast to the traditional 3DOm carbon materials, akin to structures discussed in Chapter 2, prepared by complete back-filling of the interstitial pore space of pre-formed silica colloidal crystal templates. The mesoscale ordering of the b3DOm C materials is comparable to conventional 3DOm carbons as revealed by the representative TEM image in Figure 4.1(c) and corresponding FFT pattern, suggesting an ordered packing geometry.

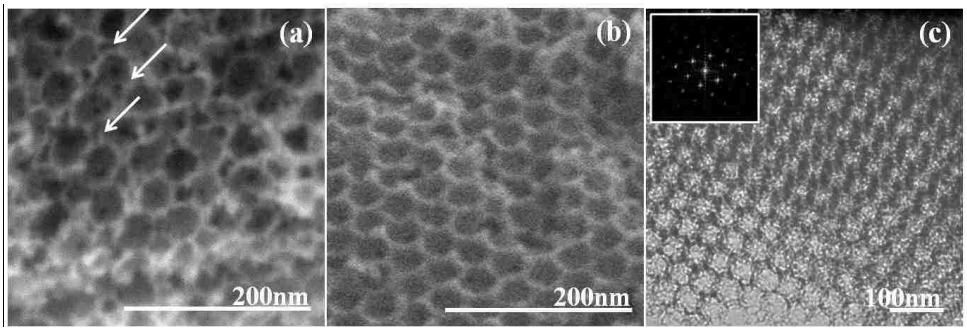

Figure 4.1: Representative electron microscope images of 3DOm carbon powders by hard-templating technique. SEM (a) and TEM (c) of co-assembly prepared sample from suspension with [glucose]=0.021g/mL; SEM (b) back-filling prepared sample.

Figure 4.2 shows the nitrogen adsorption-desorption isotherms of four carbon powder materials, three of which have been obtained by the bulk carbon-silica co-assembly approach (top three isotherms) and one (bottom) obtained by traditional back-filling techniques. In each case, a sulfuric acid-glucose solution was employed as the carbon precursor. The three co-assembled (b3DOm C) materials differ only by the concentration of the carbon source used during co-assembly (i.e., 0.021 g/mL, 0.028 g/mL, 0.035 g/mL, respectively), but share the same incipient silica nanoparticle solids content (i.e. 3.79% vol.). The precipitous nitrogen uptake at low relative pressure for all samples is indicative of micropore filling, whereas characteristic hysteresis loops measured in all cases confirm the existence of mesopores.

Table 4.1 lists the corresponding textural properties of the mesoporous materials including BET surface area as well as the total, micro- and meso-pore volumes. The lowest total surface area (1036 m^2/g) and pore volume (3.7 cc/g) is measured for the conventional back-filled 3DOm carbon material. The co-assembled b3DOm C materials all exhibit enhanced textural measures relative to the back-filled 3DOm carbon materials. We attribute this to the additional interdigitated mesopore topology associated with the interstices of the 3D-interconnected pore bodies.

Within the class of b3DOm C materials, textural properties appear strongly sensitive to the incipient concentration of the carbon precursor. Namely, with decreasing amounts of the carbon precursor over the range studied here, we observe clear enhancement of surface area, total pore volume, and mesopore volume of the b3DOm C materials over the back-filled 3DOm materials by nearly 30%, 56%, and 62%, respectively. These textural differences appear to be driven by the mesopore topology, with micropore texture, assessed by non-local density functional theory (NLDFT)-derived cumulative pore volume, appearing relatively insensitive to carbon synthesis strategy and carbon precursor concentration. We attribute the textural changes among the b3DOm C materials with decreasing incipient carbon precursor concentration to coupled effects of concomitantly decreasing d-spacing (see Chapter 3) and shrinking pore wall thickness

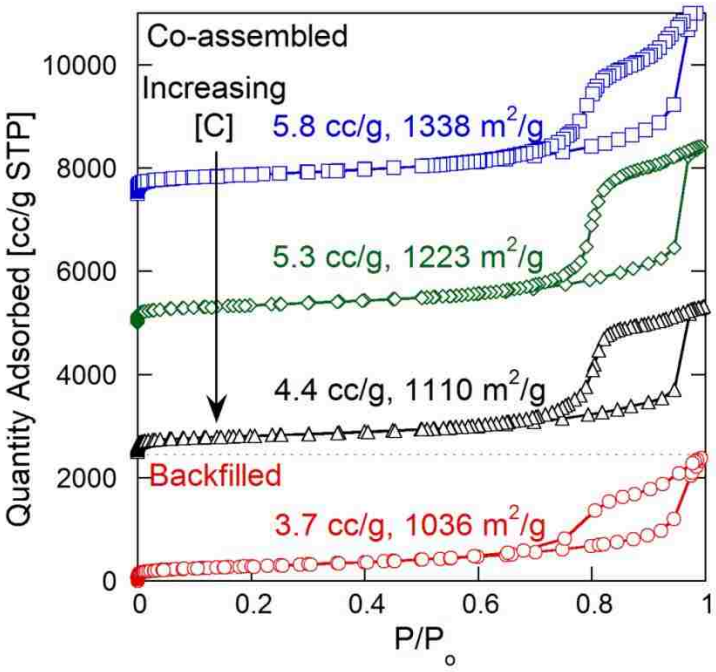

Figure 4.2 Nitrogen adsorption-desorption isotherms of hard-templating 3DOm 50nm carbon by back-filling technique and co-assembly with 3.79% vol. silica suspension and various glucose concentrations .

Table 4.1 Specific BET surface area and pore volume of 50nm template porous carbon samples

Samples	BET Surface Area (m^2/g)	Total Pore Volume (cm^3/g)	Micropore Volume (cm^3/g)	Mesopore Volume (cm^3/g)
Co-assembly C, [Glu.]=0.021g/mL	1338	5.82	0.16	5.66
Co-assembly C, [Glu.]=0.028g/mL	1223	5.28	0.14	5.14
Co-assembly C, [Glu.]=0.035g/mL	1110	4.35	0.21	4.14
Hard-templating C by Back-filled Tech.	1036	3.67	0.17	3.50

4.3.2 Template- and concentration-induced carbon microstructure control

With high-performance supercapacitor electrode applications as a target for the b3DOm C materials derived here, we are keen to elucidate the graphene or sp^2-hybridized character of these materials. To this end, we have carried out comprehensive characterization of the carbon

microstructure through complementary Raman spectroscopy, X-ray photoelectron spectroscopy (XPS), and high-resolution TEM (HR-TEM) imaging.

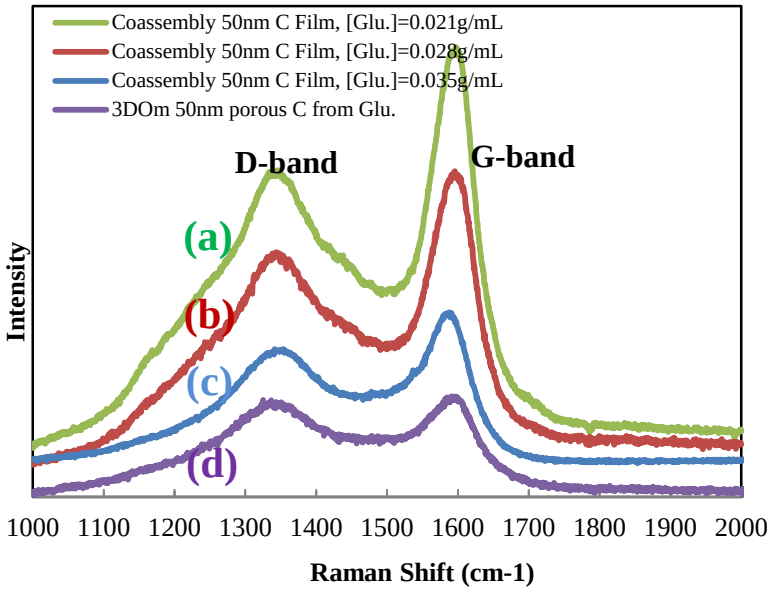

Figure 4.3 Raman spectra of template 50nm mesoporous carbon samples: (a), (b) and (c) are prepared by co-assembly technique with various glucose concentrations, i.e. 0.021g/mL, 0.028g/mL and 0.035g/mL, respectively; (d) sample prepared by traditional back-filling method.

Raman spectroscopy is widely accepted as a tool for identifying and characterizing the graphitization degree of carbon materials. Both the defect band (D-band) and graphitic band (G-band) are the characteristic signals of local domains of graphene sheets contained in a given carbon. Figure 4.3 shows the Raman spectra for the three b3DOm C materials co-assembled from solutions with tuned incipient carbon precursor concentrations and the 3DOm carbon realized by back-filling of pre-formed colloidal crystalline template. Two strong characteristic peaks at 1360cm^{-1} (D-band) and 1590cm^{-1} (G-band) can be observed for all samples, corresponding to the disordered/imperfect structures and C-C bonding vibrations of sp^2-hybridized carbon atoms, respectively[24]. The intensity ratio of the D-band versus G-band (I_D/I_G) is commonly used to estimate the graphitic degree of the carbon materials,[25] with larger magnitudes of this ratio indicating more disorder. The specific ratios derived from the Raman spectra in Figure 4.3 are

tabulated in Table 4.2. The I_D/I_G ratio is found to be largest for the back-filled 3DOm carbon (0.94), whereas the ratio systematically decreases with the controlled reduction of the carbon precursor concentration for the co-assembled b3DOm C materials. This decrease in the I_D/I_G ratio seems to indicate a higher degree of graphitization of the co-assembled b3DOm C materials than for the back-filled 3DOm carbons, and, among the b3DOm C materials, for the lowest carbon precursor concentrations. Such template-induced or concentration-induced tunability of the nature of the graphene content may prove important for tuning performance as supercapacitor electrodes.

Table 4.2 Raman spectrum I_D/I_G ratios for corresponding coassembly and back-filled carbon

	Coassembly C, [Glu.]=0.021g/mL	Coassembly C, [Glu.]=0.028g/mL	Coassembly C, [Glu.]=0.035g/mL	3DOm C from Glu.
I_D/I_G	0.67	0.70	0.74	0.94

In addition, the carbon allotrope composition of the templated porous carbons was assessed by X-ray photoelectron spectroscopy (XPS). As shown by the representative spectrum in Figure 4.4(a) collected for the b3DOm C material synthesized from a precursor solution with incipient glucose concentration of 0.021 g/mL, a survey reveals characteristic peaks corresponding to carbon and oxygen. Detailed scans of the C1s spectrum, e.g., Figure 4.4(b), can be deconvoluted into contributions from various functional groups and carbon allotropes, with the primary peak at a binding energy of 284.5 eV indicative of C-C sp^2 hybridized bonding in graphene domains[26, 27]. For the case shown in Figure 4.4, this sp^2 peak is even larger than the peak associated with the defective carbon at 285.3eV and other peaks related to C-O bonding, thus underscoring the limited defects in the co-assembly carbon samples, consistent with the Raman analysis described above. Table 4.3 summaries the peak assignment and the corresponding relative allotrope content

obtained from deconvolution of the C1s spectrum for the three specific b3DOm C materials and one 3DOm carbon studied here.

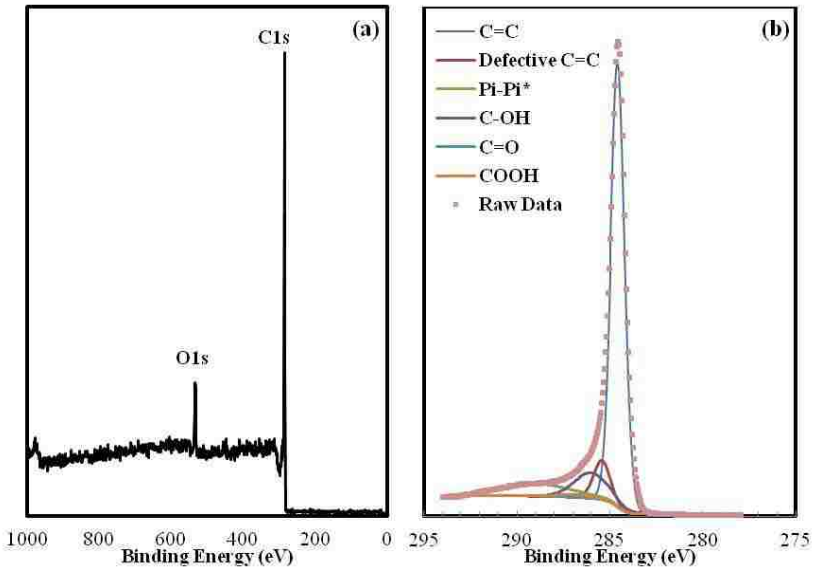

Figure 4.4 Survey X-ray photoelectron spectrum (a) and C1s spectrum analysis of obtained template 50nm mesoporous carbon by co-assembly technique with [glucose]=0.021g/mL.

Table 4.3 shows a remarkable rise in the fraction of sp^2-hybridized carbon within the b3DOm C materials as the incipient glucose concentration is decreased over the range studied. Specifically the sp^2 content rises nearly 70% in decreasing the incipient glucose concentration from 0.035 g/mL to 0.021 g/mL.

Table 4.3 Characteristic peak assignment and corresponding relative content from curve fitting of the C1s XPS

Samples	C-C sp^2	Defective C-C	Pi-Pi*	C-OH	COOR	C=O
Co-assembly C, [Glu.]=0.021g/mL	84	1	0	13	1	0
Co-assembly C, [Glu.]=0.028g/mL	72	8	4	13	3	0
Co-assembly C, [Glu.]=0.035g/mL	50	32	2	0	7	9
Hard-templating C by Back-filled Tech.	32	37	0	27	0	4

Complementary high-resolution TEM of the b3DOm C material realized by co-assembly from a solution with incipient glucose concentration of 0.021 g/mL is shown in Figure 4.5. The high-resolution image reveals the nature of the carbon near and away from the pore surface, an interface where the carbon precursor was once in intimate contact with the silica colloidal crystal template during high-temperature carbonization. The graphene-like ribbons at this interface are consistent with the measured sp^2 content and character of these materials. An apparent gradient in sp^2 character is revealed by the HR-TEM images, wherein graphene-like ribbons seem to be concentrated at the pore surface and give way to more amorphous carbon within several nanometers of that interface.

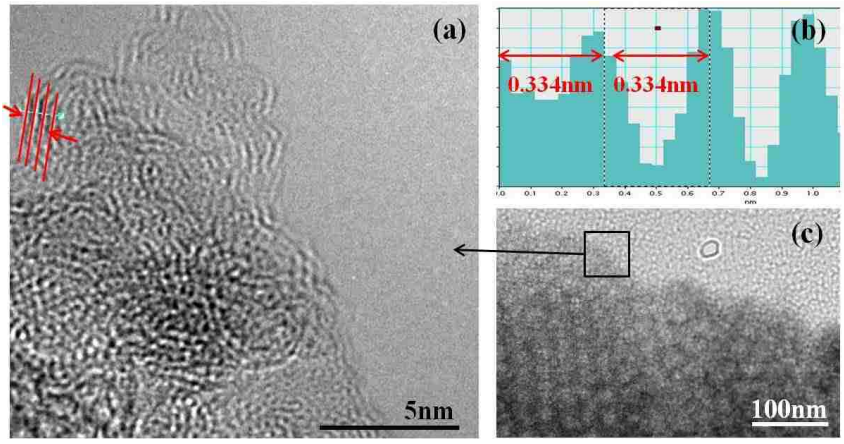

Figure 4.5 High-resolution TEM imaging of the b3DOm C material with incipient [glu]=0.021 g/mL indicating morphology consistent with interface-induced sp^2 content.

The microstructure revealed by HR-TEM suggests that the silica-carbon interface may play an important role in effectively inducing sp^2 allotrope formation within the carbon structure, perhaps during polymerization and/or carbonization. This interfacial concentration of sp^2 character is ultimately consistent with the systematic increase in sp^2 composition with decreasing incipient carbon precursor concentration. Namely, with decreasing glucose concentration, similar interface-induced sp^2 character among b3DOm C materials would lead to an enhanced volume fraction of that allotrope within the carbon walls.

4.3.3 Electrochemical properties

Here, we have identified a strategy for facile synthesis of a new class of b3DOm carbon materials, defined by large surface areas, attractive pore volumes, and unanticipated template- and concentration-induced control over sp^2 content and character with controlled glucose concentrations. This marks what we perceive to be an exciting step forward in nanocasting, and provides a potentially impactful material for meeting the transport and power density needs for high-performance supercapacitor electrodes, among other applications.

As such, we have explored the electrochemical properties of these materials for use as supercapacitor electrodes, using a three-electrode system. Figure 4.6 (a), (b) and (c),(d) show the representative cyclic voltammetry (CV) curves of the b3DOm C electrode prepared from incipient glucose composition of 0.021g/mL in both acidic (1M H_2SO_4) and basic (6M KOH) media, respectively. The nearly rectangular shapes of the CV curves, indicate an electron double-layer capacitance (EDLC) behavior. Specifically, at low scan rates (i.e. 1 mV/s, 5 mV/s, 10 mV/s and 20mV/s) shown in Figure 4.6(a), the rectangular shape but characteristic hump in such CV curves shows capacitive behavior from the combination of EDLC and redox reactions, which might be due to the nitrogen–containing heteroatom functionality during the carbonization process[28]. The nearly rectangular shapes are maintained at 20mV/s; however, the characteristic CV curves become slightly deformed at 50m V/s, as shown in Figure 4.6(b). Such deformations at higher rates are proof that faradaic reactions are involved during scanning. The humps at around 0.3~0.4V are more obvious in acid electrolyte than in basic medium, probably due to the nitrogen heteroatom functionality.

The redox reactions can be also seen in the galvanostatic charge/discharge curves, Figure 4.6(c) and (f). With generally linear and triangular shaped characteristics, a transition can be seen around 0.4V in acidic electrolyte, Figure 4.6(c), matching with the observation in the CV curves. On the contrary, for measurement in the basic electrolyte, the conversions shown in Figure 4.6(f) are not so obvious to determine. Even at current loads as high as 10A/g, the Ohmic drop is too

small to be identified, showing good electronic conductivity and fast charge/discharge propagation in both acidic and basic electrolytes. With high accuracy, galvanostatic charge/discharge curves (Figure 4.6(c) and (f)) are used to calculate capacitance of such porous carbon materials. The specific calculated capacitances are about 275F/g in H_2SO_4 and 284F/g in KOH with a current density of 1A/g. When increasing density to 10A/g, the specific capacitances are ca. 248F/g in H_2SO_4 and 242F/g in KOH, showing retentions of 90% and 85%, respectively. The capacitance and retention of conventional 3DOm carbon materials (i.e., multi-step back-filled materials bearing a unimodal pore topology) appears comparable to that reported for porous graphitic[11] electrodes, which show performance enhancements over the ordered mesoporous carbon[29], CMK-3. The b3DOm C powders, however, show remarkably high resistance to capacitance decay under high charge/discharge currents and comparatively attractive capacitance, as shown in Figures 4.7(a) and (b). This may be a coupled effect of the facile electrolyte infiltration and ion transport that should be enabled by the bi-continuous pore topology of the b3DOm C materials.

Figure 4.7(c) compares the cycling performance test for two b3DOm C materials with that of conventional back-filled 3DOm carbon. Under the current density of 1A/g, the capacitance of all tested materials changes only slightly after at least 500 cycles, with over 98% of their starting capacitances maintained. While it is difficult to decouple effects of material properties derived from the co-assembly approach, including attractive surface areas and pore volumes, the bi-continuous pore topology, and the fraction and nature of sp^2-hybridized carbon content, the b3DOm carbon materials display attractive performance metrics as high-quality and stable supercapacitor electrodes.

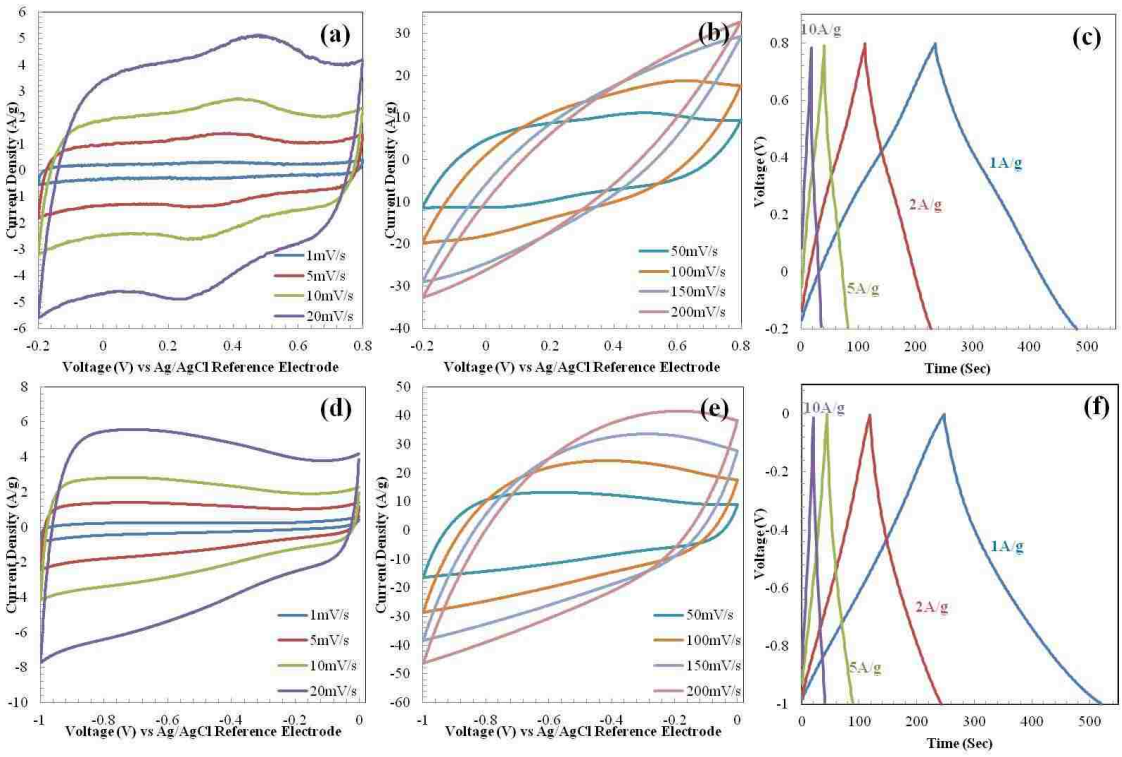

Figure 4.6 Electrochemical performance tests of the co-assembly prepared carbon sample with initial [glucose]=0.021g/mL using a three-electrode system: cyclic voltammetry (CV) measurement at different scan rates from 1mV/s to 200mV/s in 1M H2SO4 (a),(b) and 6M KOH (d),(e); and corresponding galvanostatic charge/discharge programs of various current densities from 1A/g to 10A/g in 1M H2SO4 (c) and 6M KOH (f).

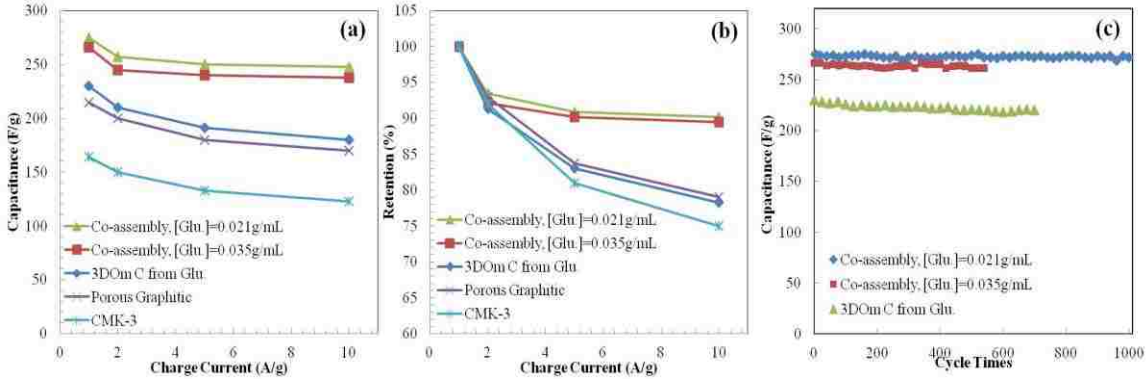

Figure 4.7 Comparison of capacitance decay between porous carbons by various techniques (a) and (b); cycling performance of the co-assembly templated porous carbon with initial [glucose]=0.021g/mL, 0.035g/mL and 3DOm C by back-filling at charge/discharge current of 1A/g.

The complex plane plots of the AC impedance spectra for the carbon samples prepared by co-assembly and back-filling techniques are shown in Figure 4.8. It is seen that the plots both exhibit two distinct traits: a semicircle in the high frequency range and a nearly vertical sloped line in the low frequency range, characteristic of capacitive behavior[30]. Generally, the short x-intercept (ohm), small diameter of the semicircle (ohm), and high slope at low frequency reveals that the hard-templating prepared 3DOm C electrodes have low internal and charge transfer (R_{ct}) resistance, as well as excellent pore accessibility for the electrolyte[31, 32]. The point intersecting with the real axis in the range of high frequency is the equivalent series resistance (ESR), including the total resistance of the ionic resistance of the electrolyte, the intrinsic resistance of active material, and the contact resistance at the active material/current collector interface[33]. The corresponding resistance values of coassembly b3DOm C samples based upon [glu.]=0.021g/mL and 0.035g/mL and 3DOm C by back-filling are 0.86, 0.87 and 0.91 ohm, respectively. Because these electrodes were prepared with 5% wt. conducting carbon black, no significant conductivity difference is observed. The small difference may be attributed to the relatively higher sp^2 hybridized C-C bonding among coassembly b3DOm carbon powders than back-filling prepared sample.

Moreover, the semicircle in the high-frequency range associates with the surface properties of the porous electrode, as magnified in the inset of Figure 4.8, which corresponds to the faradic charge transfer resistance[34]. The obtained charge transfer resistances of the coassembly b3DOm C of [glu.]=0.021g/mL and 0.035g/mL and back-filling 3DOm C are 0.23, 0.24 and 0.55 ohm, respectively, showing a lower charge transfer resistance for such b3DOm C powder samples. This lower charge transfer resistances indicate the additional presence of increased diffusion and migration pathways for electrolyte ions during charge/discharge process due to the additional smaller mesoporosity by co-assembly templating technique.

Additionally, b3DOm C samples have a larger Warburg angle than that of the 3DOm C by back-filling, suggesting faster electrolyte diffusion in the b3DOm electrode pores. For an ideal

supercapacitor without diffusion barrier, the impedance spectrum at low frequency is perpendicular to the real axis[35]. As shown in the magnified impedance spectrum, it nearly follows the ideal perpendicular characteristic confirming fluent ion transport via hydrated open porous structures.

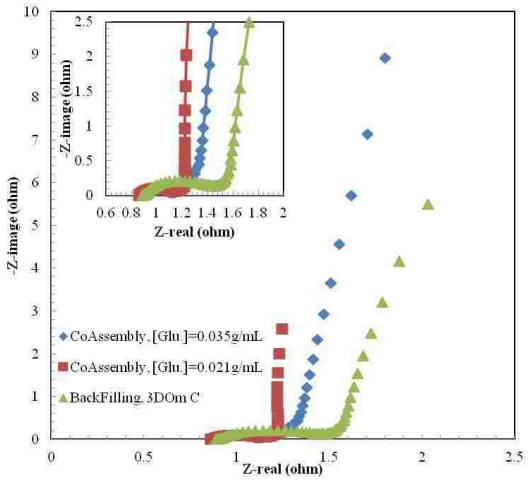

Figure 4.8: Nyquist plots for coassembly b3DOm C sample of [glu.]=0.021g/mL and 0.035g/mL and 3DOm C by back-filling.

4.4 Conclusions

A simplified 'one-pot' hard-templating method employing the co-assembly of template and replica precursors has been developed to prepare bicontinuous 3D-ordered mesoporous (b3DOm) carbon powders with controlled textural properties. The parametric range over which b3DOm C as opposed to disordered mesoporous carbons is successfully synthesized is expanded in comparison to the narrower parametric window for b3DOm C films discussed in Chapter 3. Moreover, by controlling the incipient concentration of the carbon precursor, glucose, high surface area, large pore volume materials displaying a remarkable tunability of the nature and content of graphitic domains has been realized. Taken together, the b3DOm C powders show promising performance as supercapacitor electrodes.

4.5 Reference

1. Lipomi, D. J.; Tee, B. C. K.; Vosgueritchian, M.; Bao, Z. N. Stretchable Organic Solar Cells. *Advanced Materials* **2011,** *23* (15), 1771-+.

2. Sun, Y. G.; Choi, W. M.; Jiang, H. Q.; Huang, Y. G. Y.; Rogers, J. A. Controlled buckling of semiconductor nanoribbons for stretchable electronics. *Nature Nanotechnology* **2006,** *1* (3), 201-207.

3. Yoon, J.; Baca, A. J.; Park, S. I.; Elvikis, P.; Geddes, J. B.; Li, L. F.; Kim, R. H.; Xiao, J. L.; Wang, S. D.; Kim, T. H.; Motala, M. J.; Ahn, B. Y.; Duoss, E. B.; Lewis, J. A.; Nuzzo, R. G.; Ferreira, P. M.; Huang, Y. G.; Rockett, A.; Rogers, J. A. Ultrathin silicon solar microcells for semitransparent, mechanically flexible and microconcentrator module designs. *Nature Materials* **2008,** *7* (11), 907-915.

4. Wang, C. Y.; Zheng, W.; Yue, Z. L.; Too, C. O.; Wallace, G. G. Buckled, Stretchable Polypyrrole Electrodes for Battery Applications. *Advanced Materials* **2011,** *23* (31), 3580-+.

5. Gaikwad, A. M.; Zamarayeva, A. M.; Rousseau, J.; Chu, H. W.; Derin, I.; Steingart, D. A. Highly Stretchable Alkaline Batteries Based on an Embedded Conductive Fabric. *Advanced Materials* **2012,** *24* (37), 5071-5076.

6. Nishihara, H.; Kyotani, T. Templated Nanocarbons for Energy Storage. *Advanced Materials* **2012,** *24* (33), 4473-4498.

7. Zhang, L. L.; Zhao, X. S. Carbon-based materials as supercapacitor electrodes. *Chemical Society Reviews* **2009,** *38* (9), 2520-2531.

8. Wang, G. P.; Zhang, L.; Zhang, J. J. A review of electrode materials for electrochemical supercapacitors. *Chemical Society Reviews* **2012,** *41* (2), 797-828.

9. Simon, P.; Gogotsi, Y. Materials for electrochemical capacitors. *Nature Materials* **2008,** *7* (11), 845-854.

10. Pech, D.; Brunet, M.; Durou, H.; Huang, P. H.; Mochalin, V.; Gogotsi, Y.; Taberna, P. L.; Simon, P. Ultrahigh-power micrometre-sized supercapacitors based on onion-like carbon. *Nature Nanotechnology* **2010,** *5* (9), 651-654.

11. Wang, D. W.; Li, F.; Liu, M.; Lu, G. Q.; Cheng, H. M. 3D aperiodic hierarchical porous graphitic carbon material for high-rate electrochemical capacitive energy storage. *Angew. Chem.-Int. Edit.* **2008,** *47* (2), 373-376.

12. Liu, C. G.; Yu, Z. N.; Neff, D.; Zhamu, A.; Jang, B. Z. Graphene-Based Supercapacitor with an Ultrahigh Energy Density. *Nano Letters* **2010,** *10* (12), 4863-4868.

13. Lv, W.; Tang, D. M.; He, Y. B.; You, C. H.; Shi, Z. Q.; Chen, X. C.; Chen, C. M.; Hou, P. X.; Liu, C.; Yang, Q. H. Low-Temperature Exfoliated Graphenes: Vacuum-Promoted Exfoliation and Electrochemical Energy Storage. *Acs Nano* **2009,** *3* (11), 3730-3736.

14. Wang, Y. G.; Xia, Y. Y. Recent Progress in Supercapacitors: From Materials Design to System Construction. *Advanced Materials* **2013,** *25* (37), 5336-5342.

15. Inagaki, M.; Konno, H.; Tanaike, O. Carbon materials for electrochemical capacitors. *Journal of Power Sources* **2010,** *195* (24), 7880-7903.

16. Anouti, M.; Timperman, L.; el Hilali, M.; Boisset, A.; Galiano, H. Sulfonium Bis(trifluorosulfonimide) Plastic Crystal Ionic Liquid as an Electrolyte at Elevated Temperature for High-Energy Supercapacitors. *Journal of Physical Chemistry C* **2012,** *116* (17), 9412-9418.

17. Fan, W.; Snyder, M. A.; Kumar, S.; Lee, P. S.; Yoo, W. C.; McCormick, A. V.; Penn, R. L.; Stein, A.; Tsapatsis, M. Hierarchical nanofabrication of microporous crystals with ordered mesoporosity. *Nature Materials* **2008,** *7* (12), 984-991.

18. Cychosz, K. A.; Guo, X. F.; Fan, W.; Cimino, R.; Gor, G. Y.; Tsapatsis, M.; Neimark, A. V.; Thommes, M. Characterization of the Pore Structure of Three-Dimensionally Ordered Mesoporous Carbons Using High Resolution Gas Sorption. *Langmuir* **2012,** *28* (34), 12647-12654.

19. Davis, T. M.; Snyder, M. A.; Krohn, J. E.; Tsapatsis, M. Nanoparticles in lysine-silica sols. *Chemistry of Materials* **2006,** *18* (25), 5814-5816.

20. Yokoi, T.; Sakamoto, Y.; Terasaki, O.; Kubota, Y.; Okubo, T.; Tatsumi, T. Periodic arrangement of silica nanospheres assisted by amino acids. *Journal of the American Chemical Society* **2006,** *128* (42), 13664-13665.

21. Yokoi, T.; Wakabayashi, J.; Otsuka, Y.; Fan, W.; Iwama, M.; Watanabe, R.; Aramaki, K.; Shimojima, A.; Tatsumi, T.; Okubo, T. Mechanism of Formation of Uniform-Sized Silica Nanospheres Catalyzed by Basic Amino Acids. *Chemistry of Materials* **2009,** *21* (15), 3719-3729.

22. Jun, S.; Joo, S. H.; Ryoo, R.; Kruk, M.; Jaroniec, M.; Liu, Z.; Ohsuna, T.; Terasaki, O. Synthesis of new, nanoporous carbon with hexagonally ordered mesostructure. *Journal of the American Chemical Society* **2000,** *122* (43), 10712-10713.

23. Wang, X. X.; Li, G.; Wang, W. H.; Jin, C. Z.; Chen, Y. Y. Synthesis, characterization and catalytic performance of hierarchical TS-1 with carbon template from sucrose carbonization. *Microporous and Mesoporous Materials* **2011,** *142* (2-3), 494-502.

24. Armandi, M.; Bonelli, B.; Geobaldo, F.; Garrone, E. Nanoporous carbon materials obtained by sucrose carbonization in the presence of KOH. *Microporous and Mesoporous Materials* **2010,** *132* (3), 414-420.

25. Ruiz-Hitzky, E.; Darder, M.; Fernandes, F. M.; Zatile, E.; Palomares, F. J.; Aranda, P. Supported Graphene from Natural Resources: Easy Preparation and Applications. *Advanced Materials* **2011,** *23* (44), 5250-5255.

26. Paredes, J. I.; Martinez-Alonso, A.; Tascon, J. M. D. Multiscale Imaging and tip-scratch studies reveal insight into the plasma oxidation of graphite. *Langmuir* **2007,** *23* (17), 8932-8943.

27. Zhang, W. X.; Cui, J. C.; Tao, C. A.; Wu, Y. G.; Li, Z. P.; Ma, L.; Wen, Y. Q.; Li, G. T. A Strategy for Producing Pure Single-Layer Graphene Sheets Based on a Confined Self-Assembly Approach. *Angew. Chem.-Int. Edit.* **2009,** *48* (32), 5864-5868.

28. Zhao, L.; Fan, L. Z.; Zhou, M. Q.; Guan, H.; Qiao, S. Y.; Antonietti, M.; Titirici, M. M. Nitrogen-Containing Hydrothermal Carbons with Superior Performance in Supercapacitors. *Advanced Materials* **2010,** *22* (45), 5202-+.

29. Xia, K. S.; Gao, Q. M.; Jiang, J. H.; Hu, J. Hierarchical porous carbons with controlled micropores and mesopores for supercapacitor electrode materials. *Carbon* **2008,** *46* (13), 1718-1726.

30. Saha, D.; Li, Y. C.; Bi, Z. H.; Chen, J. H.; Keum, J. K.; Hensley, D. K.; Grappe, H. A.; Meyer, H. M.; Dai, S.; Paranthaman, M. P.; Naskar, A. K. Studies on Supercapacitor Electrode Material from Activated Lignin-Derived Mesoporous Carbon. *Langmuir* **2014,** *30* (3), 900-910.

31. Huang, C. H.; Zhang, Q.; Chou, T. C.; Chen, C. M.; Su, D. S.; Doong, R. A. Three-Dimensional Hierarchically Ordered Porous Carbons with Partially Graphitic Nanostructures for Electrochemical Capacitive Energy Storage. *Chemsuschem* **2012,** *5* (3), 563-571.

32. Yang, S. J.; Kim, T.; Im, J. H.; Kim, Y. S.; Lee, K.; Jung, H.; Park, C. R. MOF-Derived Hierarchically Porous Carbon with Exceptional Porosity and Hydrogen Storage Capacity. *Chemistry of Materials* **2012,** *24* (3), 464-470.

33. Zhi, J.; Deng, S.; Zhang, Y. X.; Wang, Y. F.; Hu, A. G. Embedding Co3O4 nanoparticles in SBA-15 supported carbon nanomembrane for advanced supercapacitor materials. *Journal of Materials Chemistry A* **2013,** *1* (9), 3171-3176.

34. Wang, K.; Zhao, P.; Zhou, X. M.; Wu, H. P.; Wei, Z. X. Flexible supercapacitors based on cloth-supported electrodes of conducting polymer nanowire array/SWCNT composites. *Journal of Materials Chemistry* **2011,** *21* (41), 16373-16378.

35. Zhu, Y. W.; Murali, S.; Stoller, M. D.; Ganesh, K. J.; Cai, W. W.; Ferreira, P. J.; Pirkle, A.; Wallace, R. M.; Cychosz, K. A.; Thommes, M.; Su, D.; Stach, E. A.; Ruoff, R. S. Carbon-Based Supercapacitors Produced by Activation of Graphene. *Science* **2011,** *332* (6037), 1537-1541.

Chapter 5: Binary colloidal crystal and carbon replica thin films by multi-modal nanoparticle co-deposition

5.1 Introduction

During the past decades, colloidal crystals with a two-dimensional (2D) or three-dimensional (3D) ordered packing structure of monodispersed colloidal spheres have attracted great attention because of their potential practical applications in a variety of fields, such as photonic materials[1, 2, 3], catalysis[4], lithography and superhydrophobic surfaces. So far, most of these studies mainly focus on the fabrication process of colloidal crystals composed by single diameter colloidal spheres[5]. In previous chapters, we discussed the preparation of ordered colloidal crystal thin films based upon silica nanoparticles by different coating techniques, and related corresponding inverse replication materials with controlled mesoporosity. However, such monosized colloidal crystals have certain limitations in the structural controllability and restrict the tunability of their working performances[6, 7]. For example, the structures obtained are mostly limited to close-packed lattices, such as face-centered cubic (fcc) or hexagonal close-packed (hcp) configuration, because the thermodynamic stable position with the minimum free energy are preferred to be adopted by the building units[8]. Extra post-treatment steps[9, 10, 11, 12], which are more complex and challenging, are required to prepare ordered but non-close-packed (ncp) colloidal crystals using the monosized particles. It is reported that monomer photopolymerization[10] and reactive ion etching[9] are adopted to achieve the final ncp structure. Also, the growth of crystal structures distinct from face-centered cubic or hexagonal close-packed, and the realization of visible photonic bandgap materials cannot be achieved using monocomponent colloidal assembly. These limitations can be overcome by employing the self-assembly of large and small particles into binary colloidal crystals[13].

By combining beads of different sizes it is also possible to realize more complex crystal structures. Since the first discovery of binary superlattice in native Brazilian opal[14], the fabrication of structurally diverse binary colloidal crystals has gained growing interest and exhibited many more advantages in some practical applications and theoretical developments[15]. It has been shown that entropy is sufficient to cause bulk crystallization of structures with different superlattices, i.e. 1:2 and 1:13 stoichiometric ratios of large to small particles[16, 17]. For instance, such binary colloidal crystals can lead to photonic band-gap tunablity[18], be used as templates for ordered porous films with controlled flexible structures,[19] and are suitable for crystallographic model research studies[20].

Pusey's pioneering work studied the conditions to obtain stable binary mixtures of hard spheres[21] similar to those found in natural opals or in charged stabilized colloidal suspensions[22]. Their structures are primarily determined by the size ratio of large to small colloidal spheres and the number ratio of large to small spheres[17, 23]. More recently, different approaches have been taken to control the growth of binary structures by vertical deposition: In 2D, Kitaev et al. prepared patterns of hexagonally closed-packed binary colloid crystals with optimal quality over an area of several square centimeters via co-assembly of binary dispersion of monodispersed microspheres[24]. On the basis of the confined convective assembly, 2D binary colloidal crystals with various superlattices have been successfully fabricated. By adjusting the ratio of the diameters of the small and large particles as well as the concentration of the small colloidal particles, binary colloidal crystals of different superlattices are successfully obtained, whose number ratio of large to small can be adjusted to 1:2, 1:3, and more complicated 1:4 and 1:5[25].

When extending this method to 3D, a simple layer-by-layer growth of well-ordered binary particles has been successfully achieved[17]. With similar methods, such as stepwise spin-coating and sequential vertical deposition, a hexagonally close-packed monolayer of the large particles is first grown, and the small particles are directed to settle over the monolayer under the influence of capillary, electrostatic, and entropic forces. The small particles arrange themselves in regular

structures depending on their volume fraction and size ratio. In the third step, another layer of large particles was then deposited, and these steps were successfully repeated to grow a 3D structure of the desired thickness and composition. However, the major limitation of the methods based on the layer-by-layer principle is the growth of binary colloidal crystals with limited stoichiometric configurations over large areas[13]. Yet, these approaches are time-consuming and have difficulty in providing uniform and well-controlled binary colloidal crystals with large dimensions[15]. For example, for the layer-by-layer method, the 2D hexagonal close-packed crystal of large particles was grown with a rate of 1 to 2mm per day[17]. For general self-assembly methods, it is difficult to get large scale binary colloidal crystals, especially for 2D structure, because in a mixed suspension with colloidal spheres of two sizes, sedimentation of large particles is usually faster than small ones[15]. Also, such assembly techniques are challenged to achieve ordered binary colloidal crystals when adopting nanoparticles or large colloidal spheres larger than 600nm[26].

Dramatic scaling down of particle size to the order of 10nm shows promise for realizing novel mesoporous and even microporous materials. Up to now, there have been few research reports about binary particles with feature sizes below 100nm. In 2012, Kuroda reported that ordered binary silica nanoparticle assembly in bulk powder with AB_2 and AB_{13} type structure was achieved[27], adopting mesosized silica nanoparticles (i.e. <50nm) as building blocks. However, to our knowledge, there are no publications about converting bulk binary colloidal crystal structures to the ultrathin, three-dimensionally ordered binary nanoparticulate films, possibly due to the difficulty in precisely controlling particle size, spherical shape and uniformity in mesosize range.

In this chapter, we demonstrate proof-of-concept for the convective deposition of binary dispersion of monodisperse silica nanoparticles with specific size ratio (20/50nm, size ratio of 0.4) and number ratio (1:1, AB type) to produce 3D close-packed film structures of large nanoparticles arranged on a cubic lattice, with small 114articles confined within the interstices. Preliminary investigation of the effects of solvent and solution composition over the coating

structure of binary nanoparticles was conducted for the purpose of enlarging the area of the uniform binary film. Finally, bi-modal carbon replica films with regions of ordered binary mesoporous structure were prepared by traditional hard-templating methods employed in Chapter 2.

5.2 Materials and Experiments

5.2.1 Materials

The following reagents were used without further purification: tetraethyl orthosilicate (TEOS, Acros Organics, 98%), sulfuric acid (H_2SO_4, 98%, Sigma Aldrich), L-lysine (Sigma Aldrich, 98%), furfuryl alcohol (FA, Acros Organics, 98%) and oxalic acid (OA, Acros Organics, 98%) were obtained from Sigma-Aldrich. Hydrofluoric acid (HF, 49%) was obtained from Alfa Aesar. Hydrogen peroxide (30% wt.) was obtained from Fisher Scientific. Ethanol 200 proof was obtained from Decon Labs, Inc. Silicon wafers were purchased from Silicon Quest Int. and deionized water with resistivity 18MΩ was used for all reactions.

5.2.2 Experiments

Preparation of silica nanoparticles

As mentioned in Chapter 2, highly monodisperse silica nanoparticles with diameters of 20 nm and 50 nm were prepared with modified recipes following previous reports on direct and seeded amino acid facilitated synthesis of Lysine-Silica nanoparticles[28, 29, 30, 31]. Silica nanoparticles of 16 nm in diameter were synthesized directly, with a final molar composition, x SiO_2/ y Lysine/ z water/ 4x ethanol, of x=60, y=1.23, z=9500. Sols of larger 20 nm (x=100, y=1.23, z=9500) and 50 nm (x=1120, y=1.23, z=9500) diameter particles were prepared through a seeded growth process, in which 1 and 4 respective aliquots of TEOS were added to sols of the prepared 16 nm particles until the prescribed molar composition was reached, with intermediate hydrolysis at 90°C for at least 12 hrs following each aliquot addition. Dialysis of the resulting silica suspension

was carried out against water for 3 days with mild stirring using Spectra/Por® dialysis bags (Spectrum Labs, 3500 molecular weight cutoff). Water was exchanged every 8 hrs during dialysis until pH~5.5 was reached.

Preparation of binary silica nanoparticle suspensions and films by convective deposition

After successful hydrothermal preparation and sequential dialysis of 20nm and 50nm silica particle suspensions, the nanoparticle volume fraction of the as-made and dialyzed suspensions were measured by evaporation at 70°C. Volume fraction of the as-made 20nm and 50nm silica nanoparticle suspensions reported here were 2.01% and 8.17%, respectively. Accordingly, to prepare the AB type binary silica nanoparticle assemblies, aqueous mixture of the two sizes of silica nanoparticles were prepared. For example, 0.26mL of the 20nm as-made particle suspension and 1mL of the 50nm as-made suspension were mixed with 1.26mL of water, vortexed, and subsequently sonicated for 30min. Additionally, to further investigate the ethanol content effect over binary nanoparticulate coatings, various amounts of ethanol were added to the dialyzed 20/50nm binary suspension.

As described in previous chapters, a microliter volume (i.e. 50μL) of binary nanparticle suspension was placed between the coating blade and hydrophilic silicon wafer. The substrate was drawn at 10μm/s by a linear motor.

Binary mesoporous carbon replica films were prepared following the same hard-templating method, as described in Chapter 2. Colloidal crystal binary silica nanoparticle films were infiltrated with furfuryl alcohol/oxalic acid by precurosr vapor infiltration (PVI) in a well-sealed beaker at 90°C. After carbonization at 900°C for 3 hours under nitrogen, the silica template was selectively removed from the films by covering the films with a thin layer of diluted HF solution (5% wt.) for 1 hour. Copious amounts of ethanol were subsequently used to rinse off HF droplets from the films.

5.2.3 Characterization

Silica and carbon nanoparticles and films were characterized at ambient temperature using a Hitachi S-4300 scanning electronic microscope (SEM) and JEOL 2000FX transmission electronic microscope (TEM).

5.3 Results and Discussion

5.3.1 Convective silica nanoparticulate suspension

As shown in Chapter 2, the convective deposition of dialyzed unary silica nanoparticle suspension leads to continuous, thickness-controllable colloidal crystal films. In this chapter, coating of binary nanoparticle sols (20/50nm, AB type) results in a colloidal crystal film comprised of three regions of distinctly different binary particle morphologies along the coating direction as schematized in Figure 5.1. We attribute the variation along the film length to systematically changing solution conditions as described below (e.g., evaporation rate, particle volume fraction), and proffer that this continuum of transitioning film morphologies points to the existence of a deposition window in which particle fluxes are critically matched and other solution conditions (e.g., particle volume fraction) are ideal for successful realization of ordered binary thin films.

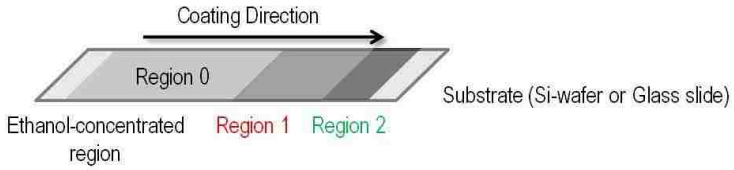

Figure 5.1: Illustration of multiple regions observed in binary nanoparticle coatings bearing differences in final binary structure.

The primary region of the film (Region 1, Figure 5.1) bears a thickness of ca. 300-400 nm and an AB (e.g., NaCl isostructural) stoichiometric binary structure with distinct cubic symmetry. Figure 5.2 shows a series of representative SEM and TEM images of this region of the film,

highlighting the local to long-range binary ordering therein. At low magnification, as shown in Figure 5. 2(b), locally ordered binary colloidal crystal domains can be observed, which is further confirmed by the fast-Fourier transform (FFT) diffraction, Figure 5.3.2(b) inset. SEM images of high magnification, Figure 5.2(a), (b) and (c) show classical cubic stoichiometry of large particles, whose interstitial spaces offer the confinement for the smaller particles. As shown in Figure 5.2(a), we can also observe the grain boundary between binary crystal domain of different orientation. Such simple NaCl-like structure is further confirmed by TEM image of corresponding binary film, Figure 5.2(d), scratched from the Si wafer support.

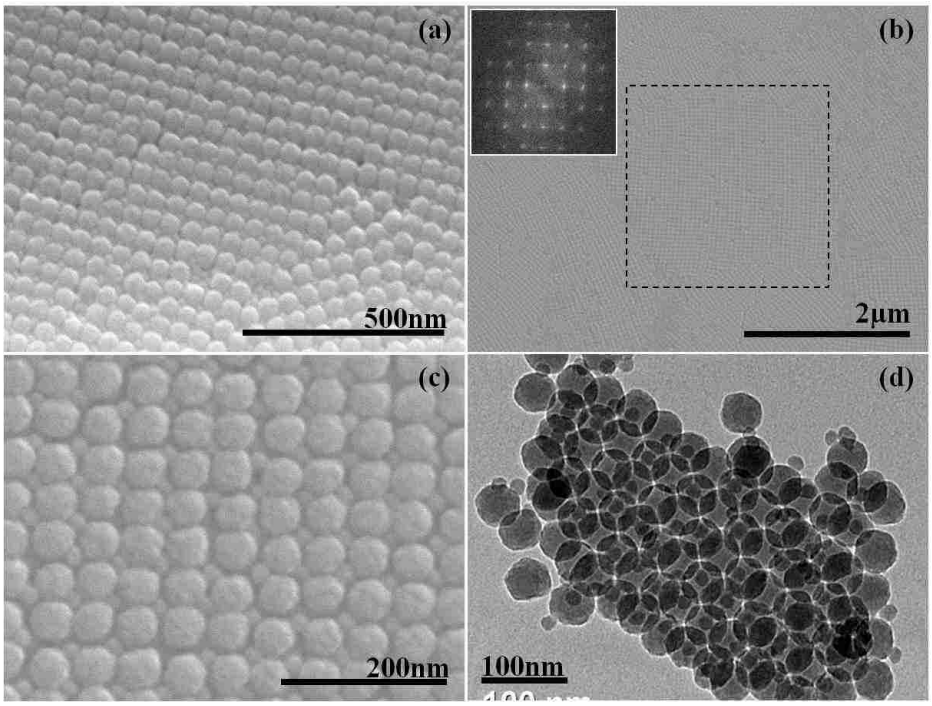

Figure 5.2: Representative SEM and TEM images of top surface of ordered binary silica nanoparticle colloidal crystal film composed of 20/50nm binary particle mixture of AB-type symmetry. (a) High magnification SEM image with transition region from one crystal domain to another; (b) Low magnification SEM image with an inset FFT diffraction to confirm the ordered cubic stoichiometry; (c) High magnification SEM image of cubic packing of large particles with confined pattern of small particles; (d) TEM image of the corresponding Region 1 section, which is scratched off from the silicon-wafer substrate.

Despite the extended binary coating in Region 1, variation in film properties are observed at shorter and longer coating times. Specifically, at short deposition times (Region 0, Figure 5.1)

the nanoparticulate film is defined by relatively thick (order of microns), strongly segregated assemblies of 50 nm particles, with dispersed 20 nm particles or clusters thereof observed (Figure 5.3 (a)). We attribute the observed nanoparticulate structure, namely the apparent segregated assembly favoring the larger 50 nm particles and the larger film thickness, to the potential modulation of the underlying fluid dynamics within the nanoparticle sol. Specifically, enhanced evaporation during the initial deposition resulting from ethanol in the as-made nanoparticle sols would impact the rate of particle convection to the drying front. This has the potential to tune properties away from possibly critically matched particle velocities required for realizing ordered binary assemblies.

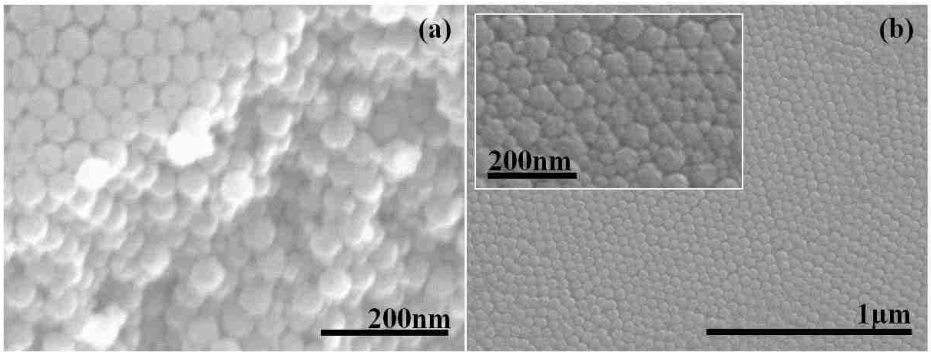

Figure 5.3: SEM image of representative (a) "Region 0" and (b) "Region 2" of binary colloidal crystal coating.

The decrease in film thickness and transition to ordered binary assemblies in progressing from Region 0 to Region 1 (Figure 5.2) can be attributed to a transition in coating properties owing to changes in both evaporation rate and particle volume fraction. As established for convectively deposited unary colloidal crystal films, decreasing film thickness for a given coating speed can be triggered by lower rates of solvent evaporation as well as lower particle volume fractions. While precise delineation between the dominant effects in this case is not possible, both effects are consistent with the progression of deposition. Namely, a gradual decrease in evaporation rate accompanying depletion of ethanol over the deposition time, and lower effective volume fraction of 50 nm particles due to their enhanced deposition within the characteristically

thicker film deposited in Region 0, are consistent with conditions required for realizing thinner films in Region 1.

A third and final region of the film, denoted as Region 2 in Figure 5.1, for which SEM images are shown in Figure 5.3 (b), shows a transition to colloidal crystal films characterized by local hexagonally close-packed symmetry and spatially non-uniform distribution of the smaller 20 nm particles. Some regions show clear HCP packing of the larger 50 nm particles with single 20 nm particles within the interstices, while others show larger clustering of the 20 nm particles.

Ultimately, Region 1 (Figure 5.1) represents idealized coating conditions for successfully achieving binary thin films. As observed previously in the case of unary nanoparticle colloidal crystal (Figure 5.4), the binary colloidal crystal films (Figure 5.2) are polycrystalline. Specifically, single crystal domains spanning regions on the order of microns in scale are separated by grain boundaries with clear inter-grain lattice mismatch. Despite the presence of these grain boundaries, very few cracks are observed in the binary thin film. In comparing the binary nanoparticle films from Region 1 to unary films of comparable thickness and the same primary particle size (Figure 5.2), two distinct differences can be observed: unary colloidal crystal films display more extensive single crystal domains than observed in the binary films, but seem to be characterized by a higher density of packing faults (e.g., arrow, Figure 5.4). The demands for precise dynamic registry of the 20 nm and 50 nm particles during assembly could conceivably give rise to more frequent nucleation of single crystal grains during deposition in the binary systems, but this secondary particle population seems also to help minimize packing faults.

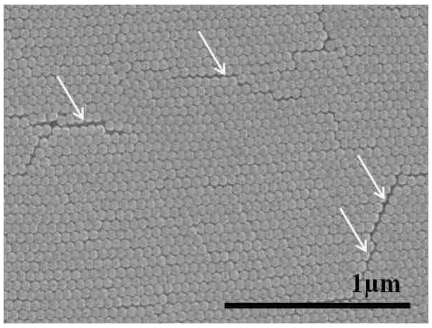

Figure 5.4: SEM image of top surface of unary 50nm nanoparticulate film by convective deposition with packing defects as highlighted by white arrow.

Based upon previous discussions about coatings of as-made 20/50nm silica suspensions, a limited region of single- and polycrystalline binary colloidal crystals is obtained. However, due to the existence of ethanol, such coating film was non-uniform, as shown in Figure 5.1. As illustrated in Chapter 2, films with ethanol-free unary silica suspensions prepared by convective deposition are uniform with single hexagonal closed packing (HCP) structures. As shown in Figure 5.5(a), when adopting the already-dialyzed 20/50nm silica suspension with 1:1 large:small stoichiometry, the final film thickness is quite uniform; scanning through the whole film along the coating direction, the binary particles were packed into semi-disordered structures. This indicates that there might be two possible parameters determining ordered binary packing during convective co-depositon: lysine and ethanol in suspension. When adding tuned amounts of Lysine to the dialyzed binary AB-type 20/50nm silica suspension to achieve the same concentration of lysine as the as-made binary mixture, the coating film, Figure 5.5(b), is uniform but with the similar semi-disordered structure as observed for the dialyzed binary suspension.

It has been reported that for binary microparticle polymer suspensions without any surfactants, fabrication of large-area films (i.e. more than $10cm^2$) can be obtained based on ethanol-assisted self-assembly at the air/water interface[15]. Also with accelerated solvent evaporation rate, uniform binary colloidal microsphere films on the scale of a few square centimeters were prepared[24]. During such rapid evaporation, large particles were first deposited

into ordered packing structure with small spheres confined exclusively in striking designs within the preformed interstitial pattern. Accordingly, when adding ethanol to the dialyzed binary suspension to increase ethanol concentration to different levels, ordered binary structures were obtained with apparently tunable area relative to what is achieved in the nominal Lysine-free binary suspension, as shown in Figure 5.6 and summarized in Table 5.1. With various ethanol concentrations, three similarly distinct regions were observed across the films. This data suggests that the combination of enhanced sedimentation of particles and capillary force might significantly contribute to such ordered binary packing.

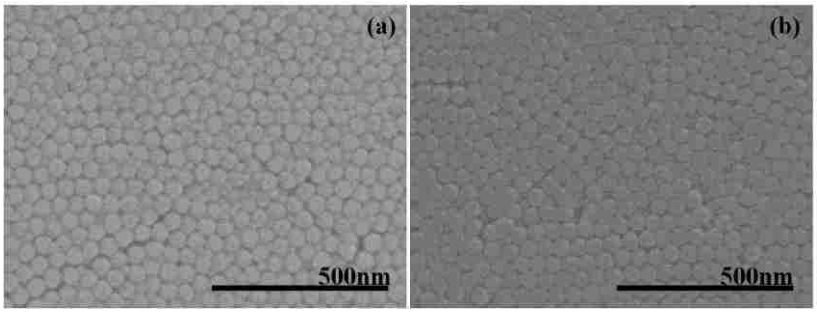

Figure 5.5: SEM images of binary silica nanoparticulate coating film based upon (a) dialyzed suspension and (b) ethanol-free suspension by dialysis and followed by adding of lysine.

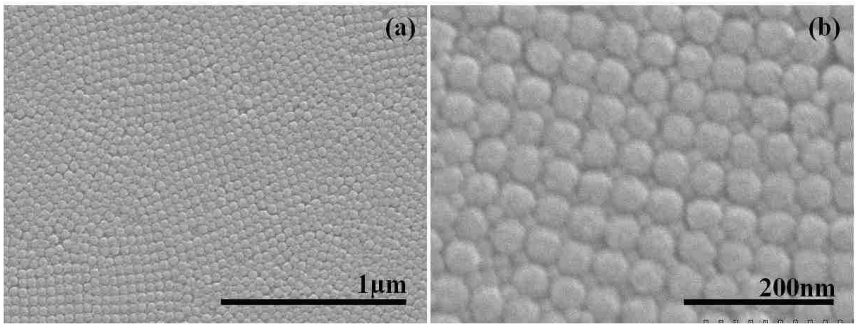

Figure 5.6: SEM images of binary cubic ordering sections of films based upon dialyzed binary 20/50nm mixture with extra adding of ethanol. (a) [Ethanol]=10% and (b) [Ethanol]=0.5% vol.

Table 5.1. Summary of ethanol and lysine existence effect over binary 20/50nm silica nanoparticulate coating films.

Sample	20nm	Vol. %	50nm	Vol. %		EtOH (wt. %)	Silica (20/50nm, wt. %)	Lysine (wt. %)	Structure	Domain Size	Crystal Content Quality
1	As-made	1.59%	As-made	11.06%		18.62%	6.98%	0.034%	Order	3~5mm	40~50%
2	Dialyzed	1.24%	Dialyzed	4.06%		0%	6.26%	0%	Disorder	0mm	0%
3	As-made	1.59%	Dialyzed	4.06%		0.63%	6.82%	0.0061 %	Order	10mm	30~40%
4	Dialyzed	1.24%	As-made	11.06%		19.25%	6.78%	0.0167 %	Order	3mm	40~50%
5	Dialyzed	1.24%	Dialyzed	4.06%		18.62%	5.09%	0%	Order	3mm	30~40%
6	Dialyzed	1.24%	Dialyzed	4.06%		14.30%	5.36%	0%	Order	5mm	70~80%
7	Dialyzed	1.24%	Dialyzed	4.06%		10%	5.36%	0%	Order	4mm	30~40%
8	Dialyzed	1.24%	Dialyzed	4.06%		5%	5.36%	0%	Order	4m	30~40%
9	Dialyzed	1.24%	Dialyzed	4.06%		2%	5.36%	0%	Order	3mm	30~40%
10	Dialyzed	1.24%	Dialyzed	4.06%		1%	5.36%	0%	Order	6mm	30~40%
11	Dialyzed	1.24%	Dialyzed	4.06%		0.5%	5.36%	0%	Order	8mm	30~40%
12	Dialyzed	1.24%	Dialyzed	4.06%		0.25%	5.36%	0%	Order	7mm	30~40%

5.3.2 Preparation of ordered binary nanoporous carbon films

In addition to realizing binary colloidal crystal films themselves, these films serve as a robust platform for realizing highly ordered, multi-modal replica porous film structures. While the binary silica nanoparticle template should be able to accommodate numerous replication agents, we specifically carry out carbon replication. This replication is carried out through infiltration of a furfural/oxalic acid mixture into the colloidal crystal film, followed by polymerization and carbonization, and, finally, selective etching of the sacrificial silica template film. The result, shown through SEM images in Figure 5.7, is an inverse replication of the original template film. Due to the relative small binary 20/50nm silica nanoparticulate colloidal crystal domains, the corresponding inverse carbon film shows similar regions of polycrystalline binary porosity, Figure 5.7(a). Under high magnification (Figure 5.7(b)), both large (50nm) and small (20nm) mesopores can be observed, with the ordering of the structure confirmed by the inset FFT diffraction pattern. In addition, the cross-sectional view of the final inverse carbon films, Figure 5.8, reveal the binary ordered 20/50nm mesoporosity spanning the full film thickness.

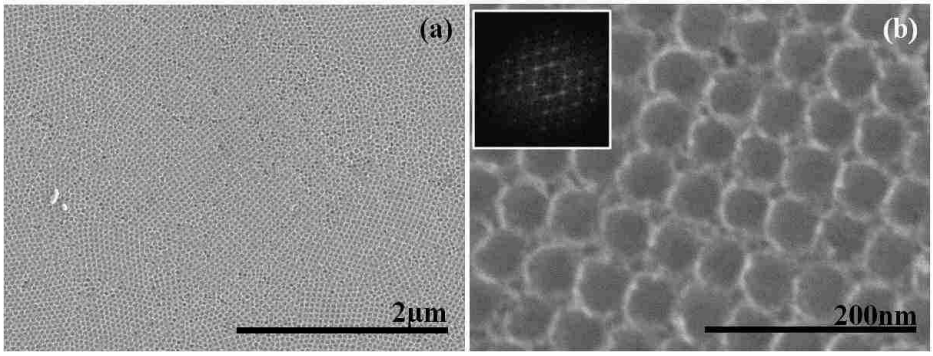

Figure 5.7: SEM images of inverse carbon films with ordered binary mesoporous structure.

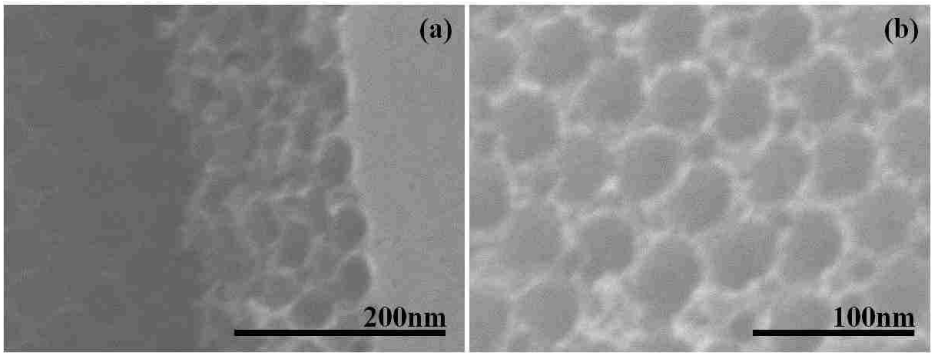

Figure 5.8: SEM images of cross-sectional view of binary carbon mesoporous films. (a) General view to confirm both cross-section and topping layer; (b) High magnification to confirm ordering structure.

5.4 Conclusions

3D-ordered binary silica films have been realized for the first time by convective assembly of mixed binary silica nanoparticle solution with primary particle sizes of 20 and 50 nm. This simple one-pot assembly method holds the potential for large-scale production of multi-modal silica films and could be applied to other similar colloidal crystal systems. The important role of ethanol within the binary suspension has been preliminary investigated, indicating that finite ethanol content may facilitate binary assembly, possibly by tuning capillary forces and/or particle flux, in order to achieve enlarged ordered binary colloidal crystals structure. 3D-interconnected bimodal mesoporous carbon films have been prepared by using the binary silica films as sacrificial hard templates. Such structures hold promise for applications in catalysis, molecular separations, and coupled reaction-separations technologies.

5.5 Reference

1. Vlasov, Y. A.; Bo, X. Z.; Sturm, J. C.; Norris, D. J. On-chip natural assembly of silicon photonic bandgap crystals. *Nature* **2001,** *414* (6861), 289-293.

2. Wang, J. J.; Li, Q.; Knoll, W.; Jonas, U. Preparation of multilayered trimodal colloid crystals and binary inverse opals. *Journal of the American Chemical Society* **2006,** *128* (49), 15606-15607.

3. Becker, C.; Linden, S.; von Freymann, G.; Wegener, M.; Tetreault, N.; Vekris, E.; Kitaev, V.; Ozin, G. A. Two-color pump-probe experiments on silicon inverse opals. *Applied Physics Letters* **2005,** *87* (9).

4. Parlett, C. M. A.; Wilson, K.; Lee, A. F. Hierarchical porous materials: catalytic applications. *Chemical Society Reviews* **2013,** *42* (9), 3876-3893.

5. Patoka, P.; Giersig, M. Self-assembly of latex particles for the creation of nanostructures with tunable plasmonic properties. *Journal of Materials Chemistry* **2011,** *21* (42), 16783-16796.

6. Zhou, Z. C.; Yan, Q. F.; Li, Q.; Zhao, X. S. Fabrication of binary colloidal crystals and non-close-packed structures by a sequential self-assembly method. *Langmuir* **2007,** *23* (3), 1473-1477.

7. Li, Y.; Cai, W.; Duan, G. Ordered micro/nanostructured arrays based on the monolayer colloidal crystals. *Chemistry of Materials* **2008,** *20* (3), 615-624.

8. Woodcock, L. V. Entropy difference between the face-centred cubic and hexagonal close-packed crystal structures. *Nature* **1997,** *385* (6612), 141-143.

9. Tan, B. J. Y.; Sow, C. H.; Lim, K. Y.; Cheong, F. C.; Chong, G. L.; Wee, A. T. S.; Ong, C. K. Fabrication of a two-dimensional periodic non-close-packed array of polystyrene particles. *Journal of Physical Chemistry B* **2004,** *108* (48), 18575-18579.

10. Jiang, P.; McFarland, M. J. Wafer-scale periodic nanohole arrays templated from two-dimensional nonclose-packed colloidal crystals. *Journal of the American Chemical Society* **2005,** *127* (11), 3710-3711.

11. Yan, X.; Yao, J. M.; Lu, G.; Li, X.; Zhang, J. H.; Han, K.; Yang, B. Fabrication of non-close-packed arrays of colloidal spheres by soft lithography. *Journal of the American Chemical Society* **2005,** *127* (21), 7688-7689.

12. Ren, Z. Y.; Li, X.; Zhang, J. H.; Li, W.; Zhang, X. M.; Yang, B. Tunable two-dimensional non-close-packed microwell arrays using colloidal crystals as templates. *Langmuir* **2007,** *23* (15), 8272-8276.

13. Singh, G.; Pillai, S.; Arpanaei, A.; Kingshott, P. Layer-by-Layer Growth of Multicomponent Colloidal Crystals Over Large Areas. *Advanced Functional Materials* **2011,** *21* (13), 2556-2563.

14. Sanders, J. V.; Murray, M. J. ORDERED ARRANGEMENTS OF SPHERES OF 2 DIFFERENT SIZES IN OPAL. *Nature* **1978,** *275* (5677), 201-203.

15. Dai, Z. F.; Li, Y.; Duan, G. T.; Jia, L. C.; Cai, W. P. Phase Diagram, Design of Monolayer Binary Colloidal Crystals, and Their Fabrication Based on Ethanol-Assisted Self-Assembly at the Air/Water Interface. *Acs Nano* **2012,** *6* (8), 6706-6716.

16. Eldridge, M. D.; Madden, P. A.; Frenkel, D. ENTROPY-DRIVEN FORMATION OF A SUPERLATTICE IN A HARD-SPHERE BINARY MIXTURE. *Nature* **1993,** *365* (6441), 35-37.

17. Velikov, K. P.; Christova, C. G.; Dullens, R. P. A.; van Blaaderen, A. Layer-by-layer growth of binary colloidal crystals. *Science* **2002,** *296* (5565), 106-109.

18. Meseguer, F. Colloidal crystals as photonic crystals. *Colloids and Surfaces a-Physicochemical and Engineering Aspects* **2005,** *270*, 1-7.

19. Jia, L. C.; Cai, W. P.; Wang, H. Q.; Sun, F. Q.; Li, Y. Hetero-apertured Micro/Nanostructured Ordered Porous Array: Layer-by-Layered Construction and Structure-Induced Sensing Parameter Controllability. *Acs Nano* **2009,** *3* (9), 2697-2705.

20. Leunissen, M. E.; Christova, C. G.; Hynninen, A. P.; Royall, C. P.; Campbell, A. I.; Imhof, A.; Dijkstra, M.; van Roij, R.; van Blaaderen, A. Ionic colloidal crystals of oppositely charged particles. *Nature* **2005,** *437* (7056), 235-240.

21. Bartlett, P.; Ottewill, R. H.; Pusey, P. N. SUPERLATTICE FORMATION IN BINARY-MIXTURES OF HARD-SPHERE COLLOIDS. *Physical Review Letters* **1992,** *68* (25), 3801-3804.

22. Yoshimura, S.; Hachisu, S. ORDER FORMATION IN BINARY-MIXTURES OF MONODISPERSE LATTICES .1. OBSERVATION OF ORDERED STRUCTURES. *Progress in Colloid and Polymer Science* **1983,** *68*, 59-70.

23. Tommaseo, G.; Petekidis, G.; Steffen, W.; Fytas, G.; Schofield, A. B.; Stefanou, N. Hypersonic acoustic excitations in binary colloidal crystals: Big versus small hard sphere control. *Journal of Chemical Physics* **2007,** *126* (1).

24. Kitaev, V.; Ozin, G. A. Self-assembled surface patterns of binary colloidal crystals. *Advanced Materials* **2003,** *15* (1), 75-+.

25. Kim, M. H.; Im, S. H.; Park, O. O. Fabrication and structural analysis of binary colloidal crystals with two-dimensional superlattices. *Advanced Materials* **2005,** *17* (20), 2501-+.

26. Zheng, Z. Y.; Gao, K. Y.; Luo, Y. H.; Li, D. M.; Meng, Q. B.; Wang, Y. R.; Zhangt, D. Z. Rapidly infrared-assisted cooperatively self-assembled highly ordered multiscale porous materials. *Journal of the American Chemical Society* **2008,** *130* (30), 9785-9789.

27. Kuroda, Y.; Sakamoto, Y.; Kuroda, K. Selective Cleavage of Periodic Mesoscale Structures: Two-Dimensional Replication of Binary Colloidal Crystals into Dimpled Gold Nanoplates. *Journal of the American Chemical Society* **2012,** *134* (20), 8684-8692.

28. Fan, W.; Snyder, M. A.; Kumar, S.; Lee, P. S.; Yoo, W. C.; McCormick, A. V.; Penn, R. L.; Stein, A.; Tsapatsis, M. Hierarchical nanofabrication of microporous crystals with ordered mesoporosity. *Nature Materials* **2008,** *7* (12), 984-991.

29. Snyder, M. A.; Lee, J. A.; Davis, T. M.; Scriven, L. E.; Tsapatsis, M. Silica nanoparticle crystals and ordered coatings using lys-sil and a novel coating device. *Langmuir* **2007,** *23* (20), 9924-9928.

30. Davis, T. M.; Snyder, M. A.; Krohn, J. E.; Tsapatsis, M. Nanoparticles in lysine-silica sols. *Chemistry of Materials* **2006,** *18* (25), 5814-5816.

31. Yokoi, T.; Sakamoto, Y.; Terasaki, O.; Kubota, Y.; Okubo, T.; Tatsumi, T. Periodic arrangement of silica nanospheres assisted by amino acids. *Journal of the American Chemical Society* **2006,** *128* (42), 13664-13665.

Chapter 6: Conclusions and Future Work

6.1 Summary

This dissertation has established strategies for hard-templating of hierarchically porous and structured carbon powders and tunable thin films by both multi-step hard-templating and a new 'one-pot' template-replica precursor co-assembly process. While the focus has been primarily on establishing new synthesis strategies and understanding mechanisms of diversified nanocasting processes, we have also demonstrated the impact of the advances in materials for applications spanning cost- and power-efficient electrodes for solar cells and supercapacitors.

Motivation for the porous carbon films discussed in Chapter 2 arose from established strategies for preparing 3DOm carbon powders through an incipient back-filling process. While novel film morphologies and properties were realized, Chapter 3 made a significant advance by establishing the process of and mechanistic insight into co-assembled nanoscasting of bi-continuous 3DOm (b3DOm) carbon films. The elucidated psedo phase behavior for realizing ordered mesoporous structures via this co-assembly approach was extended in Chapter 4 to 'one-pot' co-assembled powders of the same bi-continuous morphology with concomitantly enhanced textural and microstructural properties. As such, in the course of this dissertation we developed novel strategies that came full circle in ultimately improving nanocasting approaches in both thin films and powders, with Chapter 5 even highlighting advances extending to the enhancement of structural diversity of the colloidal crystal thin film templates themselves through multi-modal convective assembly. We believe that this platform for realizing three-dimensionally ordered mesoporous (3DOm) and bi-continuous 3DOm (b3DOm) materials is versatile and should have implications on applications spanning from separation membrane, photonics, chemical sensors to catalyst supports.

One perceived benefit of the templating paradigm established here is the potential it offers to expand well beyond the pure carbon materials described in this thesis to include a more diverse materials palette—both in terms of tuning the function of 3DOm or b3DOm carbon powders or thin films as well as establishing compositional diversity of the replica material. We conclude this thesis with two vignettes illustrating this potential through preliminary proof-of-concept data. In the first example, we describe a process by which a pre-formed silica colloidal crystal powder template can be employed to realize carbon-stabilized transmission metal nanocarbide powders that hold exciting potential, for example, in highly active and selective catalysis (e.g., hydrodeoxygenation) of biomass derivatives. In a second example, we extend the concept of 'one-pot' template-replica precursor co-assembly for realizing 3DOm metal oxide (ZrO_2) films.

6.2 Stabilization of high-surface area metal carbides toward active catalysts

6.2.1 Introduction

Catalytic processes contribute to over 90% of chemical manufacturing and more than 20% of all industrial products, and are vital for producing high volume bulk chemicals and fuels, specialty chemicals, and pharmaceuticals.[1] The use of heterogeneous catalysts is highly desirable due to their compliance with the principles of green chemistry; offering low energy routes to products, eliminating the requirement for auxiliary species, and facilitating catalyst recovery to minimize waste generation during product isolation. Metal, metal oxides and metal sulfides are among the most popular heterogeneous catalysts.[2] However, in the search for new processes and the improvement of existing processes, the application of alternative materials as catalysts is always of interest. In industrial catalytic processes there is a growing interest in substituting rare and expensive noble metal catalysts by cheap and abundant transition metal carbide materials.

For carbides, catalytic attention has predominantly centered upon binary and ternary molybdenum or tungsten based systems.[3] For example, tungsten carbide (WC) has garnered a lot of attention for its catalytic similarities to the platinum group metals[4] in several thermo- and

electro-catalytic reactions, such as biomass conversion[5, 6], hydrogen evolution and oxygen reduction[7], and alcohol electro-oxidation[8]. Molybdenum carbide (Mo_xC) also shows excellent catalytic activity and selectivity in hydrogen-involved reactions, which are traditionally catalyzed by noble metals[9]. The reactivity of such transition metal carbides is attributed to the intercalation of carbon to the tungsten and molybdenum lattices, lengthening the distances between metal atoms and giving rise to a "platinum-like" d-band electronic density states[10, 11]. More importantly, based upon their high thermal and electrochemical stability and resistance against common catalyst poisons such as carbon monoxide and sulfur, molybdenum and tungsten carbides have been identified as suitable candidates to replace costly platinum group metal-based catalysts in emerging renewable energy technologies, such as fuel cells and electrolyzers[12, 13].

Whereas there are already many methods to synthesize such molybdenum and tungsten carbide nanoparticles, none of the current methods can simultaneously prevent sintering of the metal oxide nanoparticles while also mitigating surface impurity deposition. For example, although increasing the surface area of such carbide catalyst is the most popular route toward optimization of the catalytic activity[2], by simply applying conventional carburization methods, such porous transition metal carbides with high specific surface areas are very difficult to obtain. The standard metallurgy approaches involve reaction of the metals with carbon at temperature above 1200°C to overcome the thermodynamic and kinetic barriers for carbon incorporation into the metal lattice, which induces uncontrollable particle sintering and inevitably yields bulk carbides with low surface area and catalytic activity[14]. Exploration of the true promising transition metal carbides requires the development of appropriate synthesis techniques leading to carbides with nanoscale particle size, high surface area and large pore volumes[15].

Recently, techniques, such as temperature programmed reduction carburization (TPRC) and carbothermal reduction, have been adopted to allow reduction of precursor materials at lower temperatures under a flow of hydrocarbon gases that serve as a source of carbon[16, 17, 18]. Although such low temperature preparation methods deliver relative high surface area and catalytically

active materials, the resulting carbides do not feature ordered and uniform pores that might optimize mass transport[19, 20]. For example, to be used as liquid phase catalysts, the use of mesoporous structure is advanced to minimize diffusion limitation commonly observed for microporous materials[1]. And significant enhancements in accessibility can be achieved via the use of 3D interconnected mesopore architectures over 2D ones, by establishing highly active site dispersion[21] and enhancing reagent diffusion during catalytic reactions[22] when bulky substrates are employed.

Up to now, techniques for organizing transition metal carbides on the mesoscale with high porosity are scarce. For example, ordered mesoporous metal carbides are prepared by adopting block copolymers as template, following the similar route as the soft-templating technique to prepare OMCs[23, 24, 25]. However, specific template macromolecules are unavailable in the market and require complex steps for synthesis[14]; furthermore, the use of expensive template molecules also plays a role as carbon source, leading to a relative high cost for the final carbide materials.

There have been reports to use microsize polymer colloidal particles as templates to prepare 3D ordered inverse opal tungsten carbides of feature pore size of over 200 nm, showing promising applications in photonic crystals[26, 27]. Here, to obtain 3D ordered mesoporous carbides, we employ a hard-templating strategy employing silica colloidal crystal powders akin to materials described in Chapter 2. Hydrothermal reaction is used to prepare molybdenum nanocarbides supported on carbonaceous materials, adopting monososize Lys-sil particles as templates, followed by the temperature programmed reduction carburization (TPRC) to convert the carbon-supported Mo materials into supported molybdenum nanocarbides. Such hydrothermal reaction for the production of various carbonaceous materials usually applies at mild temperatures and in pure water inside closed vessels and under autogenous pressure[28]. To further lower the material cost, renewal biomass-derived materials (specifically glucose) is used as a carbon source.

6.2.2 Materials and Methods

6.2.2.1 Materials

Ammonium molybdate (AHM, ammonium heptamolybdate, $(NH_4)_6Mo_7O_{24}\cdot 4H_2O$, 99.99%) and D-glucose ($C_6H_{12}O_6$, 99%) were purchased from Sigma-Aldrich. Potassium hydroxide (KOH, 99%) is from BDH.

6.2.2.2 Experiments

As introduced in Chapter 2, monosized 50 nm silica nanoparticles were prepared by hydrothermal reaction of tetraethyl orthosilicate (TEOS) with existence of lysine in water. Silica powders were obtained by simply drying dialyzed suspensions at 70°C in the oven. Various molybdate/glucose solutions with controlled Mo:C molar ratios were prepared. For example, a sample with Mo:C=1:15, 3.9292g of ammonium molybdate (AHM) was added to an aqueous glucose solution, composed of 10g glucose and 20g water. A sample bearing a ratio of Mo:C=1:30 was prepared similarly with addition instead of 1.9646g of AHM.

Typically 5g of dry 50nm dialyzed silica nanoparticle powders was used as a sacrificial template. This template was placed in a glass vial to which 5.09g/4.79g molybdate/glucose solutions, Mo:C=1:15 and 1:30, respectively, were added and allowed to soak for ca. 30 min . Hydrothermal reaction of the samples in the glass vial was carried out in a stainless steel autoclave at 200°C for 2hrs. After cooling to room temperature, resulting dark brown powders were dried at 70°C for over 24hr, and then carbonized at 900°C under ultra-high-purity nitrogen for 3hrs with a ramp of 5°C/min. The final 3D ordered mesoporous Mo/C composite materials were obtained by etching the silica template with 30% wt. KOH solution at room temperature for 3 days. Following the etching process, washing and centrifugation with DI-water and ethanol was used to remove the etching products and excess KOH.

Temperature programmed reduction carburization (TPRC) was carried out by Weiqing Zheng from the Catalysis Center for Energy Innovation (CCEI) at the University of Delaware. The

templated hydrothermal Molybdenum carbonaceous/silica particle composite materials were first thermally treated at 150℃ for 3 hours with ramp of 5℃ per minute under He/Ar flow of 200mL/min. Further carburization treatment steps were conducted under flow of a mixture of 400mL/min of CH_4 and 160mL/min of H_2, with heating from 150°C to 350°C with ramp of 1°C/min, 350°C to 450°C with ramp of 0.2°C/min, 450°C to 500°C with ramp of 1°C/min, 500°C to 675°C with ramp of 0.2°C/min, and a final dwell time of at 675°C for 4 hours.

6.2.2.3 Characterization

SEM and TEM characterization was carried out using a Hitachi 4300 SE/N and JEOL JEM-2000FX, with working voltages at 5kV and 200kV respectively. High-resolution TEM (HRTEM) was carried out with a JEOL ARM 200 at working voltage of 200kV. XRD patterns were taken on a diffractometer using Cu Kα radiation (λ=1.54056Å). Nitrogen adsorption and desorption isotherms were measured at 77K with a Micromeritics 2020 system. Brunauer–Emmett–Teller (BET) surface area was calculated within the relative pressure range between 0.05 and 0.3.

6.2.3 Preliminary Results and Discussion

It has been previously demonstrated that under the above mentioned hydrothermal conditions at 200°C, the hexose sugars, no matter what their complexity, degrade into (hydroxymethyl)furfural, which finally condenses to a carbon-like material having morphological similarities and the similar chemical and structural compositions[28]. The hydrothermal reaction takes place in three important steps: (1) dehydration of the carbohydrate to (hydroxymethyl)furfural, (2) polymerization towards polyfurans, and (3) carbonization via further intermolecular dehydration, which leads to carbons containing an sp^2 hybridized backbone (also responsible for the brown/black color)[28].

It is found that the presence of metal ions, such as Mo, can effectively accelerate the hydrothermal carbonization of biomass, shortening the reaction time to hours. However, such

Mo/C composite materials collected directly after hydrothermal carbonization are relatively dense materials with limited microporosity, and, therefore, low surface area. The dispersion instead of the Mo moieties over a high-surface area, but easily accessible material is desired for catalytic applications, and thus realization of an Mo/3DOm carbon morphology would be beneficial.

As shown in the preliminary SEM and TEM images, Figure 6.1 and 6.2, the 3D ordered mesoporous hydrothermal Molybdenum carbonaceous materials were successfully produced in the presence of 3D nanosized silica colloidal crystal templates. Based upon the 50nm silica nanoparticle template, Figure 6.1(a), the hydrothermal reaction of Mo with glucose under high temperature and pressure does not destroy the template's ordered structure, Figure 6.1(b). Similarly, after temperature programmed reduction carburization (TPRC) at 675°C for 4 hours under various gases, the templated structure (Figure 6.1(c)) remains and the Mo-carbon is chemically reduced to Mo_xC. Following the hard-templating route, 3DOm-supported Mo_xC (Figure 6.1(d)) is obtained after etching of the silica template.

The SEM image under high magnification of final porous Mo_xC clearly shows the final ordered mesoporosity by hard-templating method. When comparing with the glucose-based 50nm 3DOm carbon structure in Chapter 3 and 4, the 3DOm material based upon Mo-glucose source shows walls composed of small nanoparticles, highlighted with black arrows in TEM in Figure 6.1(d). The difference from the previous 3DOm C based upon glucose is probably due to the formation of MoC/C nanoparticles[14].

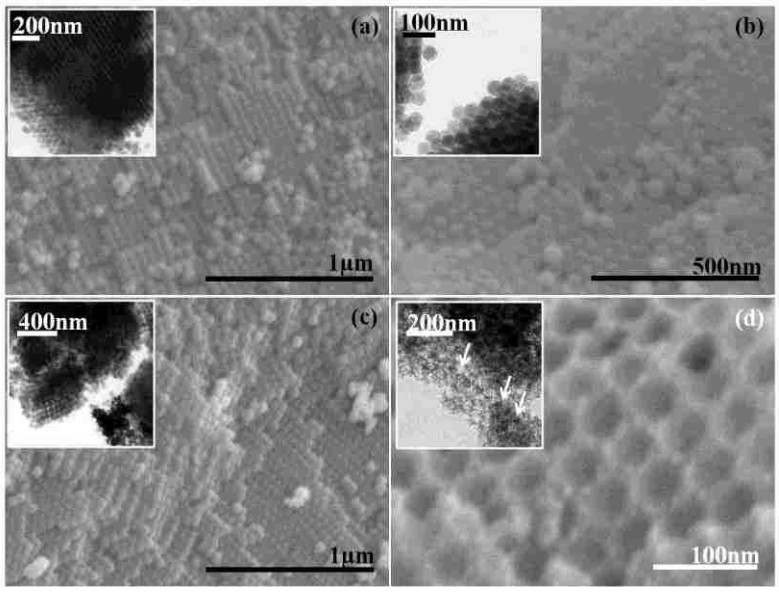

Figure 6.1: Representative SEM and inset TEM images of samples at each step throughout the whole templating route. (a) 50nm silica powder; (b) Mo-Carbon/50nm silica composite powder after hydrothermal reaction at 200°C in autoclave; (c) Mo-Carbide/50nm silica composite powder after temperature programmed reduction carburization (TPRC) at UDel and (d) Porous Mo carbide material after KOH etching off the silica template structure.

One of the most important benefits of using templating technique to prepare catalysts is to obtain high surface area and controlled porosity to optimize mass transport of reactant molecules. With the 3D mesoporosity confirmed and shown in both TEM and SEM images in Figure 6.1 (d) respectively, nitrogen physisorption measurements of porous and untemplated Mo carbonaceous materials exhibited a type I isotherm with a type H4 hysteresis (Figure 6.2(a)). The specific BET surface areas of 156m^2/g and 140m^2/g were measured for the samples with Mo:C molar ratio of 1:15 and 1:30, respectively. For the untemplated Mo carbonaceous sample, this value drops to 25m^2/g.

Furthermore, high-resolution transmission electron microscopy (HRTEM) showed that such mesoporous MoC/C were composed of MoC nanocrystallites of about 5–10 nm in size (Figure 6.3 (a) and (b)), signicantly differing from the morphology of larger and more irregular bulk commercial Mo2C particles.[29] And X-ray diffraction (XRD) cofirmed the characteristic peaks of MoC (Figure 6.3 (c)).

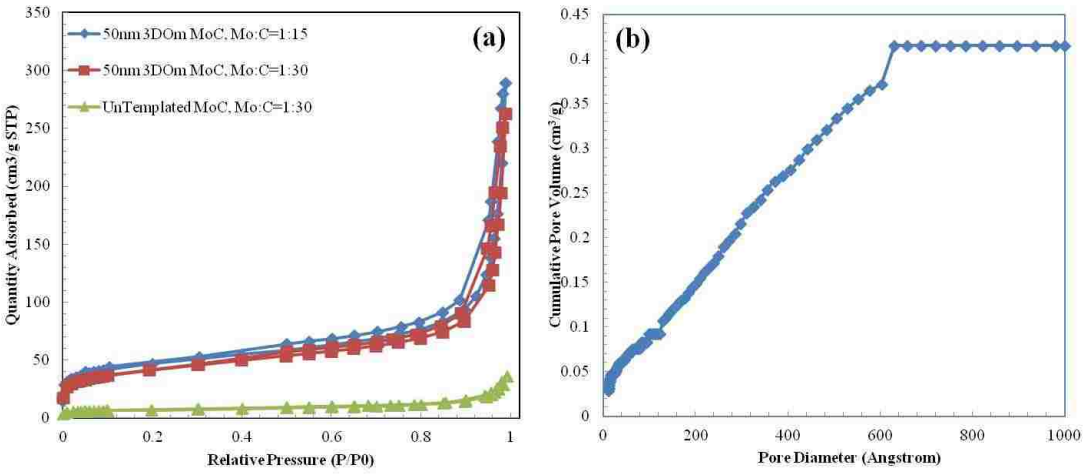

Figure 6.2: (a) Nitrogen adsorption of corresponding 50nm 3DOm and untemplated Mo/C materials; (b) Cumulative pore volume of Mo/C material, with Mo:C molar ratio of 1:15, as obtained from non local density functional theory (NLDFT, slit pore kernel), and the total pore volume was 0.437cm^3/g. The micropore volume was 0.147cm^3/g from this figure.

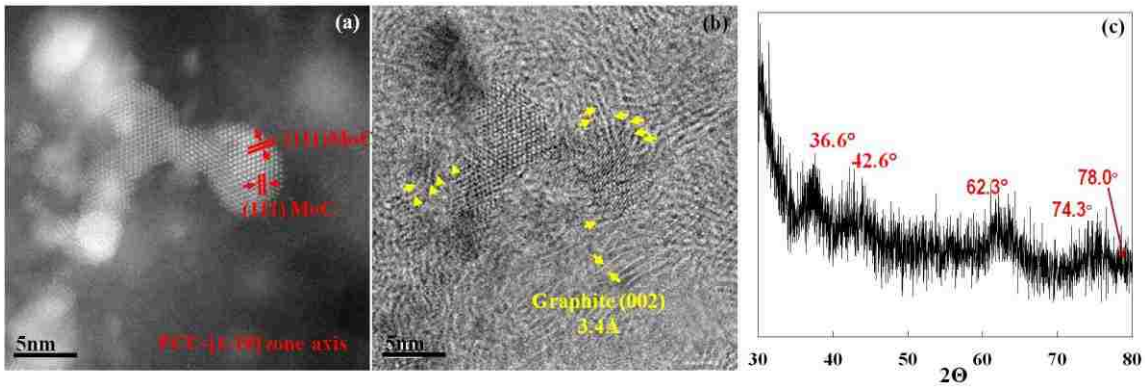

Figure 6.3: High-resolution TEM images: (a) dark-field and (b) bright field. (a) indexed (111) lattice of MoC, (b) (002) plane of stacking graphene layers around MoC nanoparticles. X-ray diffraction spectrum of corresponding mesoporous MoC.

6.2.4 Preliminary conclusions and future work

3DOm carbon-supported Mo_xC materials have been realized by hydrothermal carbonization and TPRC of aqueous glucose solutions of Mo precursors in the presence of 50 nm silica colloidal crystal templates. This low-temperature, facile method holds the potential for mesoporous transition metal carbide materials with controlled pore structure and attractive

surface area. Complementary high-resolution electron microscopy, and X-ray diffraction has revealed good dispersion of MoC nanocarbides within a 3DOm carbon framework. The MoC-supported nanocarbides hold exciting promise as stable catalysts.

6.3 Diversifying the materials palette: Co-assembly-based hard-templating of ZrO_2 films

6.3.1 Introduction

As mentioned in Section 6.2.1, highly ordered mesoporous inorganic oxides, with extremely high surface areas, finely tuned pore sizes and tunable compositions, attract great interest for applications in heterogeneous catalysis. Among those materials, zirconia is increasingly being recognized as useful catalytic material or as a catalyst support itself, owing to its intrinsic activity and hydrothermal stability[30]. Zirconia has both acidic and basic properties, and is stable under reducing conditions and generally more chemically inert than other supports such as alumina and silica. For example, nickel oxide interacts strongly with alumina and silica to form $NiAl_2O_4$ and Ni_2SiO_4, but no equivalent compound was found on zirconia[31, 32]. Unlike titania, zirconia does not photochemically degrade functionalizing agents attached to its surface[33].

A catalyst or related support should possess a large and accessible surface area, but conventional "high surface area" zirconia has a specific surface area of only 30~50m^2/g, which is low compared to other oxide supports such as alumina and silica with surface areas over 200m^2/g[30]. For example, when hydrous zirconia is used as catalyst for Meerwein-Ponndorf-Verley (MPV) reduction of aldehydes and ketones, maximum activity is obtained when the material had been calcined at 300°C, but at higher calcinations temperatures, the activity decreases due to reduced surface area[34].

The traditional route for synthesizing such mesoporous zirconia materials often utilizes self-assembled structures, such as surfactant micelles and amphiphilic block copolymer assemblies as structure directing agents (SDAs)[35]. One of the first to report the synthesis of such "templated" porous zirconia were Knowles and Hundson in 1996[36]. They postulated a scalffolding mechanism

with zirconia, where only a few detergent molecules formed a loose scaffold that kept the pores from collapse. But unlike the well-ordered hard-template materials we have employed in this thesis, the molecular scaffold is disordered, and its decomposition upon heating to e.g., 700°C-800°C, temperatures suitable for tuning crystallinity, pore collapse is observed giving rise to dense zirconia in the tetragonal form. Ordered mesoporous zirconia films have also been prepared by using another supramolecular-assisted evaporation induced self-assembly (EISA) method[33]. The first reports described the use of Pluronic F127 and Brij-58 as templates for the preparation of zirconia film from $ZrCl_4$[37, 38]. It showed that a two-step procedure was needed in order to obtain homogeneous, optical quality films: the source solution was first cast in a disordered state, and a highly ordered mesopore structure was obtained only after exposing the freshly deposited film to water vapors. This treatment adds an additional processing step that leads to potential challenges with reproducibility in film structure. Similarly to OMCs realized by soft-templating methods, calcination for surfactant removal results in the mesoporosity collapse.[38]

There have already been some reports about the successful preparation of crystalline zirconia catalysts[39] and tungsten photonic crystals[26] with large, periodically ordered, inter-connected macropores. In these reports, monosized polymer latex (i.e. PMMA) spheres were adopted as templates with feature sizes from ca. 300nm to 500nm. In order to further improve surface area and lower characteristic pore size for further application as catalysts, for example, for biomass conversion, we set out to decrease such ordered porosity to the mesoscale. To our best knowledge, there has limited reports about the repeatable preparation of 3DOm zirconia films/powders, owing in part to the rapid hydrolysis and condensation of common precursors, forming nm size particles in solution that preclude infiltration into the pore space of templates employed for mesopore replication. To overcome this obstacle, here we show proof-of-concept data for extension of the 'one-pot' precursor-template co-assembly technique described in Chapter 4 for synthesis of 3DOm zirconia films.

6.3.2 Materials and Methods

6.3.2.1 Materials

Two commonly used zirconia sources, i.e. Zirconium (IV) oxynitrate hydrate ($ZrO(NO_3)_2 \bullet 6H_2O$, Sigma-Aldrich, 99%) and Zirconyl chloride octahydrate ($ZrOCl_2 \bullet 8H_2O$, Sigma-Aldrich, 98%) were adopted as ZrO_2 precursors. Nitric acid (BDH, 68~70%) and sulfuric acid (Sigma-Aldrich, 95~98%) were directly used without any pretreatment.

6.3.2.2 Experiments

Similar to Chapter 3, dialyzed 50nm silica nanoparticulate suspensions were adopted as coating suspension. An 1M aqueous solution of zirconyl chloride ($ZrOCl_2$) was prepared by dissolving 1.61g of $ZrOCl_2 \bullet 8H_2O$ in 5g deionized water. 6.2mL of the resulting solution was added to 10mL of dialyzed 50nm silica suspension (3.8% vol.) and vortex mixed for 30 seconds. A second zirconia precursor solution was prepared by mixing 1 mL of water, 0.068 mL of nitric acid (HNO_3, 70% wt.), and 0.58g of $ZrO(NO_3)_2 \bullet 6H_2O$ to obtain a 1.7 M zirconium oxynitrate solution. The final sulfate zirconium source solution was prepared by adding 0.181mL sulfuric acid (H_2SO_4, 98% wt.) drop-wise into 1mL 1.7M zirconium oxynitrate solution. The coating suspension was prepared by mixing 10mL of dialyzed 50nm silica suspension (3.8% vol.) with 4.26mL nitrate sulfate zirconium solution.

Convective deposition was used to co-assemble zirconia precursor and silica nanoparticle templates on silicon wafers pre-treated with piranha solution (70% vol. sulfuric acid and 30% vol. hydrogen peroxide). The resulting composite films were calcined according to the zirconia precursor, namely zirconyl chloride based films were calcined at 550°C for 3 hours with a heating ramp of 5°C/min. Zirconium nitrate based films were heated to 325°C for 3 hours and then to 550°C for another 3 hours with ramp of 2°C/min. After cooling of the films to room temperature, potassium hydroxide solution (KOH, 30% wt.) was dropped onto the film to cover the surface, and allowed to stand for 2 hours to remove etch the silica template. Water and

ethanol were used to rinse the etched films, with characterization of the resulting film morphology carried out by SEM and TEM.

6.3.3 Preliminary Results and Discussion

When using the water-soluble inorganic zirconium salts as precursor, 3DOm ZrO_2 films were obtained via the precursor-template co-assembly approach described in Chapter 3. The morphology of calcined films were characterized by SEM, as shown in Figure 6.4.

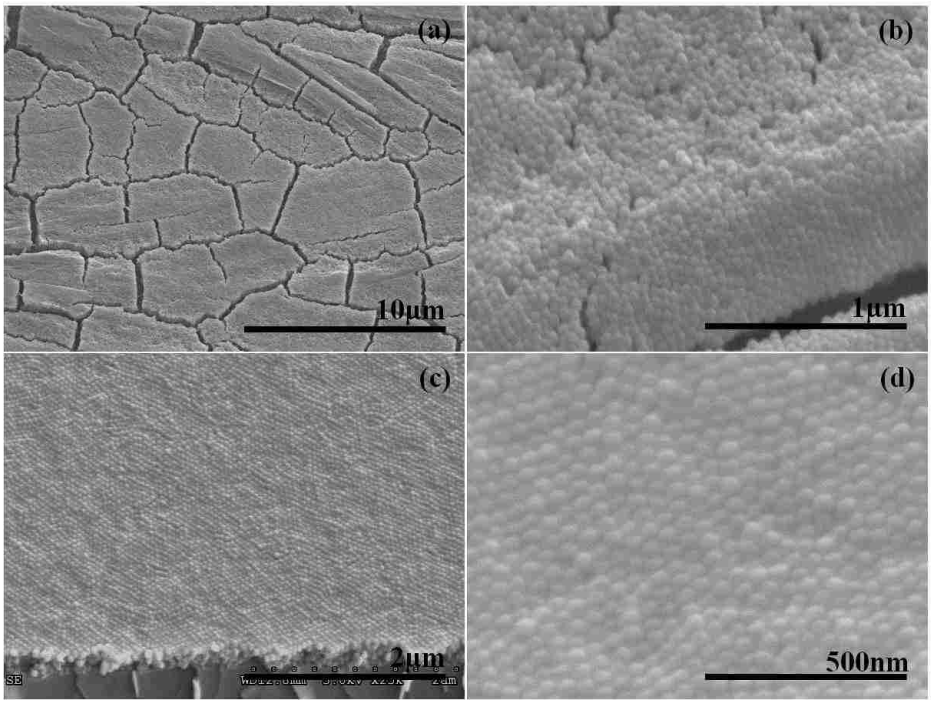

Figure 6.4: Unetched zirconia-silica composite films based upon 1M zirconium chloride octahydrate, (a) dense cracks under low magnification and (b) morphology under high magnification; Unetched sulfate zirconia-silica composite films based upon zirconium (IV) oxynitrate hydrate, (c) defect-free structure observed under low magnification and (d) ordered packing but un-smooth topping surface at high magnification.

When adopting zirconium chloride as the precursor without any additional acidification to slow hydrolysis and condensation, aggregation of silica particles and zirconium source molecules formed microsize particles, leading to discontinuous films and semi-ordered packing of silica

particles, shown Figure 6.4(a) and (b). Alternatively, formation of a clear homogeneous solution by use of sulfuric acid, known to be structural stabilizer for zirconia, [30] and zirconyl nitrate was prepared according to Ref. [39]. As shown in Figure 6.4(c) and (d), the resulting co-assembled film displays a continuous film structure with an improved ordering of the nanopartic template. Figure 6.5 illustrates a hypothesis for the co-deposition of sulfated zirconium nitrate precursor with silica nanoparticles, wherein the colloidal crystal film maintains the hexagonal close-packing of monosized silica building units with the intermediate zirconium source occupying the interstitial void spaces. Thermal treatment leads to solidification and crystallization of the zirconia precursor, forming inverse zirconia opal films when the template is finally removed by etching. The combined effects of capillary forces and liquid flux from the suspension to the drying crystal film drive template particles into an optimal packing.

However, it is not clear whether the zirconium source undergoes a similar adsorption behavior onto silica particles that was measured in Chapter 3 to occur in the case of glucose. Additionally, probably due to slow gelation of such zirconia precursors during the coating process, aggregated particles may form during the coating process and disrupt the long-range ordering of the template giving rise to the semi-smooth morphology of the silica-zirconia composite films shown in Figure 6.4(c) and (d).

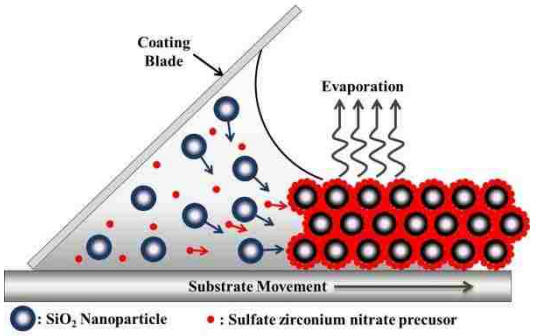

Figure 6.5: Supposed coating mechanism of co-assembly of silica nanoparticle and sulfate zirconium nitrate source molecules

After etching by KOH at room temperature to remove silica template particles, inverse opal materials were obtained, as shown in Figure 6.5. In the case of zirconyl chloride, the final zirconia film was discontinuous with semi-ordered mesoporosity as shown in Figure 6.5(a) and (b). In the case of sulfate zirconium nitrate, continuous zirconia films were successfully prepared with an improved long-range mesopore ordering achieved that is similar to that of the b3DOm carbon films discussed in Chapter 3.

Translation of the co-assembly strategy from thin-films to powders simple room solvent evaporation was not as successful as in the case of carbons (Chapter 4). Namely, no ordered mesoporoity was observed in the resulting powders, which may be due to exacerbated hydrolysis and condensation during the extended drying time that is not problematic under the shorter assembly and drying time scales for the co-assembled coatings.

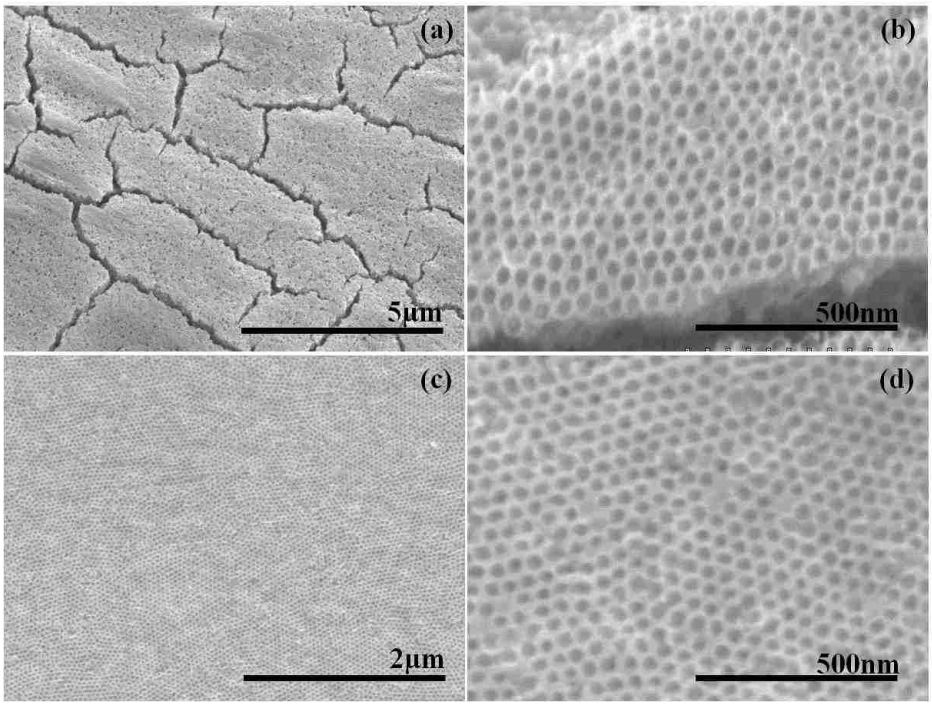

Figure 6.5: Final porous zirconia film structure. (a),(b) uncontinuous and semi-ordered mesopours ZrO_2 film using zirconyl chloride as source; (c) and (d) ordered 50nm ZrO_2 film using sulfate zirconium nitrate as source.

6.3.4 Preliminary Conclusions and Future Work

We have demonstrated proof-of-concept extension of the 'one-pot' co-assembly approach developed in Chapters 3 and 4 for carbon precursors to ordered mesoporous films of composed of zirconia. Two water-soluble zirconia sources were selected as candidate precursors, with successful realization of 3DOm ZrO_2 films. However, it remains challenging to prepare ordered mesoporous zirconia powders by this route. This underscores the important consideration that needs to be given to the stability of the replica precursor over the time scale associated with template-replica co-assembly, and the potential need to extend this time scale (e.g., by chemical stabilization) in order to realize a more diversified materials palette.

6.4 Reference

1. Parlett, C. M. A.; Wilson, K.; Lee, A. F. Hierarchical porous materials: catalytic applications. *Chemical Society Reviews* **2013,** *42* (9), 3876-3893.

2. Alexander, A. M.; Hargreaves, J. S. J. Alternative catalytic materials: carbides, nitrides, phosphides and amorphous boron alloys. *Chemical Society Reviews* **2010,** *39* (11), 4388-4401.

3. Stottlemyer, A. L.; Kelly, T. G.; Meng, Q. H.; Chen, J. G. G. Reactions of oxygen-containing molecules on transition metal carbides: Surface science insight into potential applications in catalysis and electrocatalysis. *Surface Science Reports* **2012,** *67* (9-10), 201-232.

4. Levy, R. B.; Boudart, M. PLATINUM-LIKE BEHAVIOR OF TUNGSTEN CARBIDE IN SURFACE CATALYSIS. *Science* **1973,** *181* (4099), 547-549.

5. Ji, N.; Zhang, T.; Zheng, M. Y.; Wang, A. Q.; Wang, H.; Wang, X. D.; Chen, J. G. G. Direct Catalytic Conversion of Cellulose into Ethylene Glycol Using Nickel-Promoted Tungsten Carbide Catalysts. *Angew. Chem.-Int. Edit.* **2008,** *47* (44), 8510-8513.

6. Gosselink, R. W.; Stellwagen, D. R.; Bitter, J. H. Tungsten-Based Catalysts for Selective Deoxygenation. *Angew. Chem.-Int. Edit.* **2013,** *52* (19), 5089-5092.

7. Esposito, D. V.; Hunt, S. T.; Stottlemyer, A. L.; Dobson, K. D.; McCandless, B. E.; Birkmire, R. W.; Chen, J. G. G. Low-Cost Hydrogen-Evolution Catalysts Based on Monolayer Platinum on Tungsten Monocarbide Substrates. *Angew. Chem.-Int. Edit.* **2010,** *49* (51), 9859-9862.

8. Yang, X. F.; Kimmel, Y. C.; Fu, J.; Koel, B. E.; Chen, J. G. G. Activation of Tungsten Carbide Catalysts by Use of an Oxygen Plasma Pretreatment. *Acs Catalysis* **2012,** *2* (5), 765-769.

9. Han, J. X.; Duan, J. Z.; Chen, P.; Lou, H.; Zheng, X. M. Molybdenum Carbide-Catalyzed Conversion of Renewable Oils into Diesel-like Hydrocarbons. *Advanced Synthesis & Catalysis* **2011,** *353* (14-15), 2577-2583.

10. Bennett, L. H.; Cuthill, J. R.; McAliste.Aj; Erickson, N. E.; Watson, R. E. ELECTRONIC-STRUCTURE AND CATALYTIC BEHAVIOR OF TUNGSTEN CARBIDE. *Science* **1974,** *184* (4136), 563-565.

11. Kitchin, J. R.; Norskov, J. K.; Barteau, M. A.; Chen, J. G. G. Trends in the chemical properties of early transition metal carbide surfaces: A density functional study. *Catalysis Today* **2005,** *105* (1), 66-73.

12. Wu, M. X.; Lin, X. A.; Hagfeldt, A.; Ma, T. L. Low-Cost Molybdenum Carbide and Tungsten Carbide Counter Electrodes for Dye-Sensitized Solar Cells. *Angew. Chem.-Int. Edit.* **2011,** *50* (15), 3520-3524.

13. Esposito, D. V.; Hunt, S. T.; Kimmel, Y. C.; Chen, J. G. G. A New Class of Electrocatalysts for Hydrogen Production from Water Electrolysis: Metal Monolayers Supported on Low-Cost Transition Metal Carbides. *Journal of the American Chemical Society* **2012,** *134* (6), 3025-3033.

14. Lunkenbein, T.; Rosenthal, D.; Otremba, T.; Girgsdies, F.; Li, Z. H.; Sai, H.; Bojer, C.; Auffermann, G.; Wiesner, U.; Breu, J. Access to Ordered Porous Molybdenum Oxycarbide/Carbon Nanocomposites. *Angew. Chem.-Int. Edit.* **2012,** *51* (51), 12892-12896.

15. Giordano, C.; Erpen, C.; Yao, W. T.; Antoniett, M. Synthesis of Mo and W Carbide and Nitride Nanoparticles via a Simple "Urea Glass" Route. *Nano Letters* **2008,** *8* (12), 4659-4663.

16. Volpe, L.; Boudart, M. COMPOUNDS OF MOLYBDENUM AND TUNGSTEN WITH HIGH SPECIFIC SURFACE-AREA .2. CARBIDES. *Journal of Solid State Chemistry* **1985,** *59* (3), 348-356.

17. Lee, J. S.; Oyama, S. T.; Boudart, M. MOLYBDENUM CARBIDE CATALYSTS .1. SYNTHESIS OF UNSUPPORTED POWDERS. *Journal of Catalysis* **1987,** *106* (1), 125-133.

18. Lee, J. S.; Volpe, L.; Ribeiro, F. H.; Boudart, M. MOLYBDENUM CARBIDE CATALYSTS .2. TOPOTACTIC SYNTHESIS OF UNSUPPORTED POWDERS. *Journal of Catalysis* **1988,** *112* (1), 44-53.

19. Schuth, F. Endo- and exotemplating to create high-surface-area inorganic materials. *Angew. Chem.-Int. Edit.* **2003,** *42* (31), 3604-3622.

20. Hartmann, M. Hierarchical zeolites: A proven strategy to combine shape selectivity with efficient mass transport. *Angew. Chem.-Int. Edit.* **2004,** *43* (44), 5880-5882.

21. Parlett, C. M. A.; Bruce, D. W.; Hondow, N. S.; Lee, A. F.; Wilson, K. Support-Enhanced Selective Aerobic Alcohol Oxidation over Pd/Mesoporous Silicas. *Acs Catalysis* **2011,** *1* (6), 636-640.

22. Pirez, C.; Caderon, J. M.; Dacquin, J. P.; Lee, A. F.; Wilson, K. Tunable KIT-6 Mesoporous Sulfonic Acid Catalysts for Fatty Acid Esterification. *Acs Catalysis* **2012,** *2* (8), 1607-1614.

23. Cui, X. Z.; Li, H.; Guo, L. M.; He, D. N.; Chen, H.; Shi, J. L. Synthesis of mesoporous tungsten carbide by an impregnation-compaction route, and its NH3 decomposition catalytic activity. *Dalton Transactions* **2008,** (45), 6435-6440.

24. Huang, C. H.; Gu, D.; Zhao, D. Y.; Doong, R. A. Direct Synthesis of Controllable Microstructures of Thermally Stable and Ordered Mesoporous Crystalline Titanium Oxides and Carbide/Carbon Composites. *Chemistry of Materials* **2010,** *22* (5), 1760-1767.

25. Liu, H. J.; Wang, J.; Wang, C. X.; Xia, Y. Y. Ordered Hierarchical Mesoporous/Microporous Carbon Derived from Mesoporous Titanium-Carbide/Carbon Composites and its Electrochemical Performance in Supercapacitor. *Advanced Energy Materials* **2011,** *1* (6), 1101-1108.

26. Denny, N. R.; Han, S. E.; Norris, D. J.; Stein, A. Effects of thermal processes on the structure of monolithic tungsten and tungsten alloy photonic crystals. *Chemistry of Materials* **2007,** *19* (18), 4563-4569.

27. Lytle, J. C.; Denny, N. R.; Turgeon, R. T.; Stein, A. Pseudomorphic transformation of inverse opal tungsten oxide to tungsten carbide. *Advanced Materials* **2007,** *19* (21), 3682-+.

28. Titirici, M. M.; Antonietti, M. Chemistry and materials options of sustainable carbon materials made by hydrothermal carbonization. *Chemical Society Reviews* **2010,** *39* (1), 103-116.

29. Liao, L.; Wang, S. N.; Xiao, J. J.; Bian, X. J.; Zhang, Y. H.; Scanlon, M. D.; Hu, X. L.; Tang, Y.; Liu, B. H.; Girault, H. H. A nanoporous molybdenum carbide nanowire as an electrocatalyst for hydrogen evolution reaction. *Energy Environ. Sci.* **2014,** *7* (1), 387-392.

30. Jaenicke, S.; Chuah, G. K.; Raju, V.; Nie, Y. T. Structural and Morphological Control in the Preparation of High Surface Area Zirconia. *Catalysis Surveys from Asia* **2008,** *12* (3), 153-169.

31. Gavalas, G. R.; Phichitkul, C.; Voecks, G. E. STRUCTURE AND ACTIVITY OF NIO ALPHA-AL2O3 AND NIO/ZRO2 CALCINED AT HIGH-TEMPERATURES .1. STRUCTURE. *Journal of Catalysis* **1984,** *88* (1), 54-64.

32. Smith, K. E.; Kershaw, R.; Dwight, K.; Wold, A. PREPARATION AND PROPERTIES OF CUBIC ZRO2 STABILIZED WITH NI(II). *Materials Research Bulletin* **1987,** *22* (8), 1125-1130.

33. Zelcer, A.; Soler-Illia, G. One-step preparation of UV transparent highly ordered mesoporous zirconia thin films. *Journal of Materials Chemistry C* **2013,** *1* (7), 1359-1367.

34. Shibagaki, M.; Takahashi, K.; Kuno, H.; Matsushita, H. THE CATALYTIC ACTIVITY OF HYDROUS ZIRCONIUM-OXIDE CALCINED AT SEVERAL TEMPERATURES. *Bulletin of the Chemical Society of Japan* **1990,** *63* (1), 258-259.

35. Fan, J.; Boettcher, S. W.; Tsung, C. K.; Shi, Q.; Schierhorn, M.; Stucky, G. D. Field-directed and confined molecular assembly of mesostructured materials: Basic principles and new opportunities. *Chemistry of Materials* **2008,** *20* (3), 909-921.

36. Hudson, M. J.; Knowles, J. A. Preparation and characterisation of mesoporous, high-surface-area zirconium(IV) oxide. *Journal of Materials Chemistry* **1996,** *6* (1), 89-95.

37. Crepaldi, E. L.; Soler-Illia, G.; Bouchara, A.; Grosso, D.; Durand, D.; Sanchez, C. Controlled formation of highly ordered cubic and hexagonal mesoporous nanocrystalline yttria-zirconia and ceria-zirconia thin films exhibiting high thermal stability. *Angew. Chem.-Int. Edit.* **2003,** *42* (3), 347-+.

38. Crepaldi, E. L.; Soler-Illia, G.; Grosso, D.; Sanchez, M. Nanocrystallised titania and zirconia mesoporous thin films exhibiting enhanced thermal stability. *New Journal of Chemistry* **2003,** *27* (1), 9-13.

39. Al-Daous, M. A.; Stein, A. Preparation and catalytic evaluation of macroporous crystalline sulfated zirconium dioxide templated with colloidal crystals. *Chemistry of Materials* **2003,** *15* (13), 2638-2645.

VITAE

Zheng Tian

EDUCATION and WORK EXPERIENCE

- Bemis Company, Inc., Neenah, Wisconsin — Jul. 2014-Present
  Research Scientist, Bemis Innovation Center
- Lehigh University, Bethlehem, Pennsylvania — Sep. 2008-Jun. 2014
  Ph.D., Dept. of Chemical Engineering — *Advisor: Prof. Mark A. Snyder*
  Thesis: *Template-mediated, hierarchical engineering of ordered mesoporous films and powders*
- Beijing Entry-Exit Inspection and Quarantine Bureau, P.R. China — Aug. 2006-Aug. 2008
  Senior Engineer, Safety Packing Division for Chemicals
- Tsinghua University, Beijing, P.R. China — Sep. 2004-Jun. 2006
  M.S., Dept. of Chemical Engineering — *Advisor: Prof. Chunrong Wan*
  Thesis: *Polyacrylonitrile (PAN) based gel polymer electrolyte for Lithium-ion battery*
- Tsinghua University, Beijing, P.R. China — Sep. 2000-Jun. 2004
  B.S., Polymer Materials and Engineering

PUBLICATIONS and REPORTS

1. **Z. Tian**, M. A. Snyder, "Hard templating of symmetric and asymmetric carbon thin films with three-dimensionally ordered mesoporosity," *Langmuir* dx.doi.org/10.1021/la501870h
2. **Z. Tian**, M. A. Snyder, "Nanocasting of bicontinuous three-dimensionally ordered mesoporous carbon films by template-replica co-assembly," *Langmuir* (submitted)
3. S.C. Kung, **Z. Tian**, M.A. Snyder, "Convective assembly of binary nanoparticle thin films," in preparation
4. **Z. Tian**, M. A. Snyder, "Tunable bicontinuous three-dimensionally ordered mesoporous carbon films by convective co-assembly," in preparation
5. S.C. Kung, **Z. Tian**, M. A. Snyder, "Three-dimensionally ordered binary colloidal crystal films," *EPI Graduate Progress Report (GRPR)* (2013). *(Cover article)*
6. **Z. Tian**, M. A. Snyder, "From nanoparticles to porous materials: Towards porous thin films for membrane applications," *EPI Graduate Research Progress Report (GRPR)* (2010). *(Cover article)*
7. W.H. Pu, X.M. He, L. Wang, **Z. Tian**, C.Y. Jiang, C.R. Wan, "Preparation of P(AN-MMA) gel electrolyte for Li-ion batteries," *Ionics* 14(2008) 27-31.
8. **Z. Tian**, W.H. Pu, X.M. He, C.R. Wan, C.Y. Jiang, "Preparation of a microporous polymer electrolyte based on poly(vinyl chloride)/poly(acrylonitrile-butyl acrylate) blend for Li-ion batteries," *Electrochimica Acta* 52(2007) 3199-3206.
9. W.H. Pu, X.M. He, L. Wang, **Z. Tian**, C.Y. Jiang, C.R. Wan, "Sulfur composite cathode materials: comparative characterization of polyacrylonitrile precursor," *Ionics* 13(2007) 273-276.
10. **Z. Tian**, X.M He, W.H. Pu, C.R. Wan, C.Y. Jiang, "Preparation of poly(acrylonitrile-butyl acrylate) gel electrolyte for lithium-ion batteries," *Electrochimica Acta* 52(2006) 688-693.
11. W.H. Pu, X.M He, L. Wang, **Z. Tian**, C.Y. Jiang, C.R. Wan, "Preparation of P(AN-MMA) microporous membrane for Li-ion batteries by phase inversion," *Journal of Membrane Science* 280(2006) 6-9.

SELECTED CONFERENCE PRESENTATIONS

1. Z. Tian, Q. Guo, S.C. Kung, W.C. Yoo, **M. A. Snyder**, "Hierarchically Engineered Nanoporous Materials by Assembly and Template Control," Gordon Research Conference on Nanoporous Materials & Their Applications, NH, Aug. 2013. *Oral Presentation*
2. **Z. Tian**, M. A. Snyder, "Assembly and Scaffolding Strategies for Realizing Ultra-thin Inorganic Films with Tunable Porosity," 2013 Catalysis Society of Metropolitan New York Annual Symposium, Princeton University, Princeton, Mar. 20, 2013. *Poster Presentation* ***(2nd Place Poster Award)***.
3. **Z. Tian**, M. A. Snyder, "Assembly and Scaffolding Strategies for Realizing Ultra-thin Inorganic Films with Tunable Porosity," 16th Northeast Corridor Zeolite Association Annual Meeting, University of Pennsylvania, Philadelphia, Dec. 14, 2012. *Poster Presentation* ***(Awarded oral presentation from poster competition)***
4. **Z. Tian**, M. A. Snyder, "Templated Engineering of Ultra-Thin Mesoporous and Hierarchically Porous Films," 2012 AIChE Annual Meeting, Pittsburgh, Oct. 29-Nov.2, 2012. *Oral Presentation*
5. **Z. Tian,** M. A. Snyder, "Hierarchical Engineering of Tunable Nanoparticulate and Templated Porous Films," 2011 Catalysis Society of Metropolitan New York Annual Symposium, Rutgers University, New Brunswick, Mar. 16, 2011. *Poster Presentation* ***(3rd Place Poster Award)***
6. **Z. Tian,** M. A. Snyder, Annual Review Meeting of Emulsion Polymers Institute (EPI), Lehigh University, Bethlehem, PA, 2009~2013. *Poster Presentation*

SKILLS and EXPERTISE

Synthesis and characterization of polymers, colloids, coating films, porous materials, Li-ion battery, capacitor and electrochemical behaviors

- Coating film formation: Convective deposition, Spin coating, Blade-coating, Phase-inversion
- Polymer chemistry/physics/processing: DSC, TGA, FT-IR, UV-Vis, HPLC
- Electronic microscopy characterization: SEM, TEM, EDS
- Colloidal particle surface/size, porous materials: DLS, zeta-Potential, N_2 Adsorption, XRD, Raman, XPS
- Electrochemical characterization: CV, EIS, Galvanostat Cycling

AWARDS

- Kenneth A. Earhart Research Award, EPI , Lehigh University, PA 2013
- 2nd Place Poster Award, Catalysis Society of Metropolitan New York, Princeton University, NJ 2013
- William C. Gottshall Graduate Fellowship, Lehigh University, PA 2013
- Poster Award and Invited Talk, Northeast Corridor Zeolite Association, University of Pennsylvania 2012
- 3rd Place Poster Award, Catalysis Society of Metropolitan New York, Rutgers University, NJ 2011

7. Chen, NCF Graduate Fellowship, Lehigh University, PA 2009, 2010

RESEARCH AFFILIATIONS

- American Institute of Chemical Engineers (AIChE)
- Emulsion Polymers Institute (EPI) at Lehigh University
- Center for Advanced Materials and Nanotechnology (CAMN) at Lehigh University